UNIVERSIDAD NACIONAL AUTÓNOMA DE MÉXICO
POSGRADO EN CIENCIAS DEL MAR Y LIMNOLOGÍA

ZONATION, STRUCTURE AND GEOLOGICAL DEVELOPMENT OF A FRINGING REEF AT MAHAHUAL

TESIS

QUE PARA OPTAR EL GRADO ACADÉMICO DE:
MAESTRO EN CIENCIAS
(GEOLOGÍA MARINA)

PRESENTA:
EDUARDO GABRIEL ISLAS DOMÍNGUEZ

TUTOR PRINCIPAL:
Dr. PAUL BLANCHON
INSTITUTO DE CIENCIAS DEL MAR Y LIMNOLOGÍA, UNAM
COMITÉ TUTOR:
Dr. LORENZO ÁLVAREZ FILIP
INSTITUTO DE CIENCIAS DEL MAR Y LIMNOLOGÍA, UNAM
Dr. ISMAEL MARIÑO TAPIA
ESCUELA NACIONAL DE ESTUDIOS SUPERIORES, UNIDAD MÉRIDA, UNAM
Dr. JOAQUÍN RODRIGO GARZA PÉREZ
UNIDAD MULTIDISCIPLINARIA DE DOCENCIA E INVESTIGACIÓN, SISAL, UNAM
Dr. MARCO ANTONIO PÉREZ FLORES
CENTRO DE INVESTIGACIÓN CIENTÍFICA Y DE EDUCACIÓN SUPERIOR DE ENSENADA (CICESE), BAJA CALIFORNIA

ASESORA EXTERNA:
Mtra. MARIANA PATRICIA GÓMEZ NICOLÁS
CENTRO DE INVESTIGACIÓN CIENTÍFICA Y DE EDUCACIÓN SUPERIOR DE ENSENADA (CICESE), BAJA CALIFORNIA

MÉXICO, CD. MX., ENERO, 2022

ZONATION, STRUCTURE AND GEOLOGICAL DEVELOPMENT OF A FRINGING REEF AT MAHAHUAL

TESIS

QUE PARA OBTENER EL GRADO ACADÉMICO DE:
MAESTRO EN CIENCIAS
(GEOLOGÍA MARINA)

PRESENTA:
EDUARDO GABRIEL ISLAS DOMINGUEZ

TUTOR PRINCIPAL:
Dr. PAUL BLANCHON
INSTITUTO DE CIENCIAS DEL MAR Y LIMNOLOGÍA, UNAM
COMITÉ TUTOR:
Dr. LORENZO ÁLVAREZ FILIP
INSTITUTO DE CIENCIAS DEL MAR Y LIMNOLOGÍA, UNAM
Dr. ISMAEL MARIÑO TAPIA
ESCUELA NACIONAL DE ESTUDIOS SUPERIORES, UNIDAD MÉRIDA, UNAM
Dr. JOAQUÍN RODRIGO GARZA PÉREZ
UNIDAD MULTIDISCIPLINARIA DE DOCENCIA E INVESTIGACIÓN, SISAL, UNAM
Dr. MARCO ANTONIO PÉREZ FLORES
CENTRO DE INVESTIGACIÓN CIENTÍFICA Y DE EDUCACIÓN SUPERIOR DE ENSENADA (CICESE), BAJA CALIFORNIA

ASESORA EXTERNA:
Mtra. MARIANA PATRICIA GÓMEZ NICOLÁS
CENTRO DE INVESTIGACIÓN CIENTÍFICA Y DE EDUCACIÓN SUPERIOR DE ENSENADA (CICESE), BAJA CALIFORNIA

MÉXICO, CD. MX., ENERO, 2022

Not a MM thesis…

ACKNOWLEDGEMENTS

To the Universidad Nacional Autonoma de México (UNAM), which thanks to its wide range of opportunities and infrastructure, I have been able to study what I like in amazings scenarios.

To the Posgrado en Ciencias del Mar y Limnología for their support during my master studies.

CONACYT for both, financial support of my postgraduate studies (scholarship 2020-000026-02NACF) and research project number A1-S-18879 , which financed the field trips to Mahahual.

To my supervisor, Paul Blanchon, for taught me the first steps to do science, for believe in me, supporting me and encourage me to move beyond, and last but not least, for his editing skills which considerable improved my english writing.

To the Tutoral Committee members for their reviews and commnets which helped to improve this project: Dr. Lorenzo Álvarez Filip, for shared with me the Mahahual ecological data recovered by his lab (BARCOLAB); Dr. Imael Mariño and Dr. Rodrigo Garza for their comments and suggestions; and Dr. Marco Pérez for his time, teaching and comments related to electrical methods, which significantly improved the geophysical parto for this project.

A particular gratitude to Mtra. Mariana Gómez Nicolas, who selfless continue teaching, helping and motivating me to learn more about geophysics, thanks for your time, and knowledge.

Dr. Paulo Salles, coordinator of the National Coastal Resilience Laboratory (LANRESC) and Dr. Christian Appendini, headо of the Laboratory of Engineering and Coastal Processes (LIPC) from SISAL Academic Unit from UNAM Engineering Institute, as well. For kindly provide the SuperSting. And to the SISAL technician, MI. Juan Alberto Gomez Liera, for its invaluable help and its disposition during the “geophysical field trip to Mahahual”.

TABLE OF CONTENTS

TABLE OF FIGURES VII

TABLES IX

ABSTRACT X

RESUMEN XI

INTRODUCTION 1

BACKGROUND 2

HYPOTHESIS 5

OBJECTIVES 5

STUDY AREA 6

METHODS 9

- Bathymetry and biogeomorphology 9
- Drill-Core Transects and Logging 10
- Electrical resistivity Imaging 11
  - Survey Protocol 16
  - Data Inversion 18

RESULTS 20

- Biogeomorphic zonation and bathymetry 20
- Internal Composition 24
- Paleoenvironmental interpretation 29
- Electrical Resistivity Profiles 32

DISCUSSION 34

- Further work 37

SUMMARY AND CONCLUSIONS 38

REFERENCES 40

ANNEX A 43

- 1. Reef Core Analysis Protocol 43
- 2. Scanned cores and composition logs 44
  - 2.1. M1a 44
  - 2.2. M1b 45
  - 2.3. M2 46
  - 2.4. M3a 47
  - 2.5. M3b 48
  - 2.6. M4 49

2.7. M5a 50
2.8. M5b 51
2.9. M6 52
2.10. M7a 53
2.11. M7b 54
2.12. M8a 55
2.13. M8b 56

ANNEX B 57

1. Initial Inversion Settings 57
1.1. Criteria for Data Removal 57
2. Forward Modelling Settings 58
3. Resistivity Inversion Settings 59
3.1. Stop criteria 59
3.2. Data weights 60
3.3. Horizontal/Vertical Roughness Ratio 61
4. .UWT files 62
5. Number of processed data, RMS and L2 values for each transect 63
6. Inverted resistivity profile in XYZ format 64

TABLE OF FIGURES

Fig. 1. Development stage model of Galeta Point fringing reef 2
Fig. 2. Hurricane-control model. 4
Fig. 3. Spatial distribution of hurricanes and tropical storms over the Caribbean region 5
Fig. 4. Mahahual fringing reef location 7
Fig. 5. Zonation and geomorphology schemes reported for Mahahual reef 9
Fig. 6. Mahahual reef zonation area 10
Fig. 7. Drill-Core transects 11
Fig. 8. Four electrode common configuration for electrical resistivity survey 12
Fig. 9. Types of electrode arrays 15
Fig. 10. Simplified representation of the inversion process 16
Fig. 11. Distortion of uniform field by ridges and valleys 16
Fig. 12. Electrical survey transects 17
Fig. 13. Idealised schematic representation of electrical resistivity survey 18
Fig. 14. Summary of the environmental data from Mahahual reef 21
Fig. 15. Hard coral assemblage obtained from ecological transects 22
Fig. 16. Biogeomorphic zonation of the fringing reef at Mahahual 23
Fig. 17. Core transect over the reef front 26
Fig. 18. Upper unit core logs showing primary and secondary framework, framework modification and sediment texture 27
Fig. 19. Lower unit core logs showing primary and secondary framework, framework modification and sediment texture 28
Fig. 20. Comparison between the benthic coral assemblages and facies assemblages in the internal framework 31
Fig. 21. Electrical Resistivity Profiles 33
Fig. 22. Mahahual fringing reef profile 34
Fig. A.1. Core description protocol used for reefal sedimentary units 43
Fig. A.2.1. Core M1a 44
Fig. A.2.2. Core M1b 45
Fig. A.2.3. Core M2 46
Fig. A.2.4. Core M3a 47
Fig. A.2.5. Core M3b 48
Fig. A.2.6. Core M4 49
Fig. A.2.7. Core M5a 50
Fig. A.2.8. Core M5b 51

Fig. A.2.9. Core M6 52
Fig. A.2.10. Core M7a 53
Fig. A.2.11. Core M7b 54
Fig. A.2.12. Core M8a 55
Fig. A.2.13. Core M8b 56
Fig. B.1. Initial Settings window. 57
Fig. B.2. Forward Modelling settings window. 58
Fig. B.3.1. Reciprocal error analysis 61
Fig. B.3.2. Resistivity Inversion settings window 61
Fig. B.4. T2 Electrical Resistivity Profile with water resistivity value set 63
Fig. B.6. ER mesh profiles. 65

TABLES

Table 1. Electrical resistivity survey settings used for each electrode array in the SuperSting for both transects 17

Table 2. Summary of the selected settings 18

Table 3. Unified colour scale 19

ABSTRACT

Models of Caribbean coral reef development have traditionally been based on vertical accretion models, where coralgal framework keeps pace with sea-level (SL) rise. In recent years, a new development model was added, in which external factors like hurricanes play a key role in accretion processes. Both models have been proven valid in specific areas where different environmental conditions prevail. In areas with a high frequency of hurricanes the reef structure is mainly composed of layers of *A. palmata* coral clasts that were destroyed and deposited by large hurricane waves. By contrast, in areas where hurricanes are absent or infrequent, reefs are composed of largely in-place coralgal framework. However these models fail to account for variations in exposure to oceanic conditions and the possibility that reefs can either be protected in areas of high hurricane incidence or exposed to destructive swell events in areas where hurricane incidence is low. In these cases, it may be that reef development is different from either end-member model. To test this hypothesis we investigate the geomorphology, internal structure and geological development of a sheltered fringing reef at Mahahual in the southeast Yucatan Peninsula. The geomorphological zonation shows a tripartite zonation typical of Caribbean reefs, but with an anomalously wide sub-horizontal intertidal reef flat behind the crest. The internal structure is reconstructed from 13 drilled cores, and consists of two facies units: a lower facies unit (from 6 to 13 m below SL) which developed under low-energy conditions, is composed of small/medium in-situ head-corals, dominated by *S. siderea* and *O. annularis*, with interstitial rubble; and a upper facies unit (from 2 to 6 m below SL) developed in higher energy conditions, composed of skeletal sand and coral gravel with lenses of *O. annularis* framework. Electric Resistivity Imaging shows the reef deposit is a seaward-thickening wedge being 2 ± 1 m thick below the back-reef flat, and increasing to 10 ± 2m below the middle reef front, with the underlying bedrock extending to 18 ± 2 m below this. These results show that reef development at Mahahual is notably different from other Caribbean reefs, and therefore supports the hypothesis that reefs protected from the direct impact of hurricanes have different geomorphology, different internal composition, and developed more extensive vertical sequences than reefs exposed to hurricanes.

RESUMEN

Los modelos de desarrollo de arrecifes de coral en el Caribe se han basado tradicionalmente en modelos de acreción vertical, donde el marco coralino se mantiene a la par del aumento del nivel del mar (NM). En los últimos años se sumó un nuevo modelo de desarrollo, en el que factores externos como los huracanes juegan un papel fundamental en los procesos de acreción. Ambos modelos han demostrado ser válidos en áreas específicas donde prevalecen diferentes condiciones ambientales. En áreas con una alta frecuencia de huracanes, la estructura del arrecife se compone principalmente de capas de clastos del coral A. palmata, que fueron destruidos y depositados por grandes olas de huracanes. Por el contrario, en áreas donde los huracanes están ausentes o son poco frecuentes, los arrecifes están compuestos en gran parte por una estructura coral-alga *in situ*. Sin embargo, estos modelos no tienen en cuenta las variaciones en la exposición a las condiciones oceánicas y la posibilidad de que los arrecifes puedan protegerse en áreas de alta incidencia de huracanes o exponerse a oleaje destructivo en áreas donde la incidencia de huracanes es baja. En estos casos, puede ser que el desarrollo del arrecife sea diferente al de ambos modelos. Para probar esta hipótesis, investigamos la geomorfología, la estructura interna y el desarrollo geológico de un arrecife de franja protegido en Mahahual, en el sureste de la Península de Yucatán. La zonación geomorfológica muestra una zonación tripartita típica de los arrecifes del Caribe, pero con una zona plana ancha intermareal subhorizontal anómala detrás de la cresta. La estructura interna se reconstruyó a partir de 13 núcleos perforados y consta de dos unidades de facies: una unidad de facies inferior (de 6 a 13 m por debajo del NM) que se desarrolló en condiciones de baja energía y está compuesta por corales pequeños/medianos tipo cabeza *in situ*, dominada por *S. siderea* y *O. annularis*, con escombros intersticiales; y una unidad de facies superior (de 2 a 6 m por debajo del NM) desarrollada en condiciones de mayor energía, compuesta de arena esquelética y grava de coral con lentes de marco de *O. annularis*. Las imágenes de resistividad eléctrica muestran que el depósito del arrecife es una cuña que se engrosa hacia el mar, con un espesor de 2 ± 1 m por debajo de la parte posterior plana del arrecife y aumentando a 10 ± 2 m por debajo de la mitad del arrecife frontal, con el lecho rocoso subyacente que se extiende hasta 18 ± 2 m por debajo de este. Estos resultados muestran que el desarrollo del arrecife en Mahahual es notablemente diferente al de otros arrecifes del Caribe y, por lo tanto, respalda la hipótesis de que los arrecifes protegidos del impacto directo de los huracanes tienen una geomorfología diferente, una composición interna diferente y desarrollaron secuencias verticales más extensas que los arrecifes expuestos a huracanes.

INTRODUCTION

Caribbean coral reefs are widely considered to accrete and develop due to the sequential growth of corals. This vertical accretion process is consistent with development models which designate coral framework as the dominant component of reef development (Darwin, 1842; Daly, 1915; Adey, 1978; Neumann & Macintyre, 1985, among others). Although there are significant differences between these models, vertical accretion is the main paradigm.

Studies of the morphology and development of Caribbean coral reefs however show significant differences to reefs in other oceans and imply that not all of them develop in this way (Blanchon et al., 2022). Recent studies, for example, have claimed that other external factors, such as hurricane incidence, is a principal control on their structural development, and a new model, the hurricane-control model, has been proposed (Blanchon et al., 2017). In this model the internal structure of reefs in areas with high hurricane incidence consists of coral gravel layers, rather than in-place corals, and develop as a result of a destruction-recovery cycle over thousands of years (Blanchon et al., 2017). This model has been proposed for reef development in the Northeast Yucatan and Grand Cayman where the incidence of hurricanes reaches a maximum (Blanchon et al. 1997; Blanchon and Perry 2004; Blanchon et al., 2017). By contrast, areas where hurricane frequency is minimal or absent, favour a non-destructive environment which allows corals to grow in-situ and develop into coral framework, as proposed by Macintyre & Glynn (1976) from a fringing reef in Panama, and other locations such as Curacao and Bonaire (Meyer et al., 2003).

Even though both models have a delimited region of validity according to the relative frequency of hurricane paths, it is clear that regions must exist where reefs can develop in areas protected from the impact of hurricane wave activity, such as in the lee of offshore banks or along the sheltered leeward coasts of islands. In such cases, the internal structure and geologic development of reefs should be controlled by non-hurricane related processes, and therefore show significant differences. To test this hypothesis, I investigate the geomorphology, internal composition and form of the underlying substrate of a fringing reef at Mahahual, in the southeast of the Yucatan Peninsula, which by its location at the shadow of Chinchorro Bank is protected from the direct impact of large hurricane waves. I then compare these results to those found in similar investigations on a nearby reef that is exposed to hurricane conditions (Blanchon et al., 2017, Islas-Domínguez, 2020).

BACKGROUND

Darwin (1842) formalised the first model of coral reef development, proposing that reefs were the result of vertical-accretion to keep them at sea level (SL) during the progressive subsidence of volcanic islands, and generating the classic trilogy of reef types: fringing reefs, barrier reefs and atolls. Darwin was followed by many other well-known scientists with the same basic vertical accretion idea, such as Daly (1915), who thought reefs accreted vertically from lowstand erosion terraces during postglacial SL rise. By the end of the fifties, the modern era of investigation of reefs in the western atlantic started, with Goreau (1959) claiming that *M. annularis* was the single most important coral framework in Jamaican reefs. At the beginnings of the sixties, the internal structure of reefs was beginning to be investigated and, using explosive methods, Shinn (1963) determined that the internal structure of spurs and grooves from Florida reefs was composed by in-growth position *A. palmata* colonies, with infillings of reef debris. This model was extended by Mesolella (1967) and Mesolella, et al. (1969) who described a coral framework in zones made up by *M. annularis, A. palmata* and *A.cervicornis* respectively, as the major builders of Pleistocene reefs tracts, from uplifted reefs in Barbados. These findings resemble and were related to the modern reef benthic cover zonation of the time, which led Mesoella to propose his coral zonation model as a climax development of West Indian reefs.

By the seventies, Scoffin (1972) and Scoffin & Garret (1974) studied the extensive fields of patch reefs in Bermuda out in the Atlantic, using blocks of reef rock. They described five processes in which the primary framework of the patch reefs, made up by *Diploria spp, M. cavernosa, P, astreoides* and *Siderastrea sp.*, were preserved into the subsurface. Shortly thereafter, Macintyre & Glynn (1976) undertook the first drilling studies of the internal structure of Caribbean modern reefs using closely spaced drill-cores, describing the fringing reef at Galeta Point, Panama, and discovering it had developed by vertical accretion of almost entirely *A, palmata* framework, beginning ~7ky before the present (BP), with at least 14 m thick of reef deposit (Fig. 1).

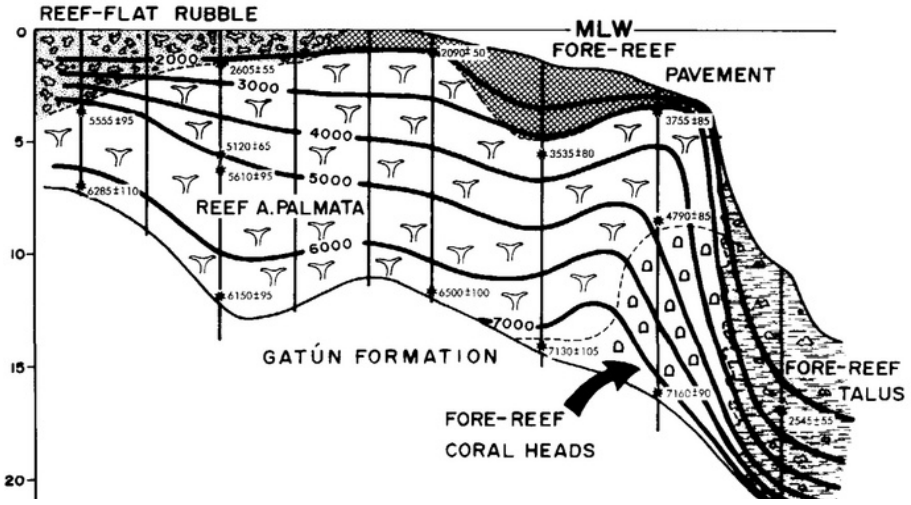

Fig.1. Development model of Galeta Point fringing reef. Made up almost entirely by *A. palmata* framework. Vertical depth in metres (modified from Macintyre & Glynn, 1976).

Macintyre et al. (1977) then described the internal structure of Alacran reef, from a single core in the southwest of the reef complex, and determined a thickness of at least 22.7 m, with *A. cervicornis* as the principal framework builder, along with a significant contribution of *M. annularis* (now reclassified as *Orbicella annualris*). Then based principally on multiple drill core studies in St. Croix island and other reef locations, Adey (1978) proposed a model for reef building in tropical shores, in which vertical accretion had a multidimensional response to antecedent topography, growth potential, wave energy, and local SL rise pattern. This was extended in the eighties by Neumann & Macintyre (1985), who proposed that vertical accretion was a response to the rate of SL rise by comparing the existence drill-core data from Atlantic holocene reefs, giving a rise/growth relationship of three types: *Keep-Up* reefs which accreted vertically at the same rate of SL rise, made up principally by an *A. palmata* sequence; *Catch-Up* reefs that caught up when the rate of SL rise slowed, made of head coral and/or *A cervicornis*; and Give-Up reefs which failed to maintain their position at SL.

By the nineties however the vertically-accretion paradigm started to be questioned when, Blanchon et al. (1997) used short cores (< 1.5 m) and excavations to determine the internal structure of the fringing reef complex around Grand Cayman, finding that the internal structure was made up of abraded coral rubble, dominated by *A, palamta* clasts, and not by coral framework. Instead they proposed that this coral rubble composition was produced from a cycle of coral destruction and deposition during hurricanes. The influence of hurricanes was subsequently supported by Macintyre et al. (2001), who determined the internal reef structure of the algal ridge on the seaward edge of the Holandés Cays, in Panama, was composed by extensively lithified *Agaricia/Millepora* rubble, formed by a series of storm deposits almost 3 Ky BP.

Soon after, Mayer et al. (2003) reported the impact of a rare hurricane on the reefs of Curacao and Bonaire, southern Caribbean, and compared surveys of the hurricane damage in the modern reefs with Pleistocene fossil coral reefs data from the island, which presented elevated proportions of in-place position corals in the record. They concluded that these results were consistent with the hypothesis that in regions experiencing very low frequency of hurricanes, like southern Caribbean, there is more probability of conserving corals in growth positions than in regions with higher hurricane frequency. Blanchon & Perry (2004) analysed the internal structure of Campeche Bank reefs in the Gulf of Mexico, by means of short drilled cores (< 2m), reporting that the internal structure was mainly composed of *A. palmata* gravels. They too concluded that hurricanes have a major influence on reef development, and that distinct depth-related facies are present which do not reflect the benthic coral zonation.

The impact of hurricanes on coral reef development was refined further by Blanchon et al. (2017) who proposed a development model based on a drill-core transect on a fringing reef at Punta Maroma, in the northeast Mexican Caribbean. These data showed that the internal reef structure was primarily composed of a 2 m-thick layer of *A.palmata* clasts that has retrograded over its backreef during the last 5.5 ka. To explain these findings, a hurricane-control model was

developed which proposed a cycle of reef destruction during hurricanes and recovery with the gradual rise in SL since the mid Holocene (Fig. 2).

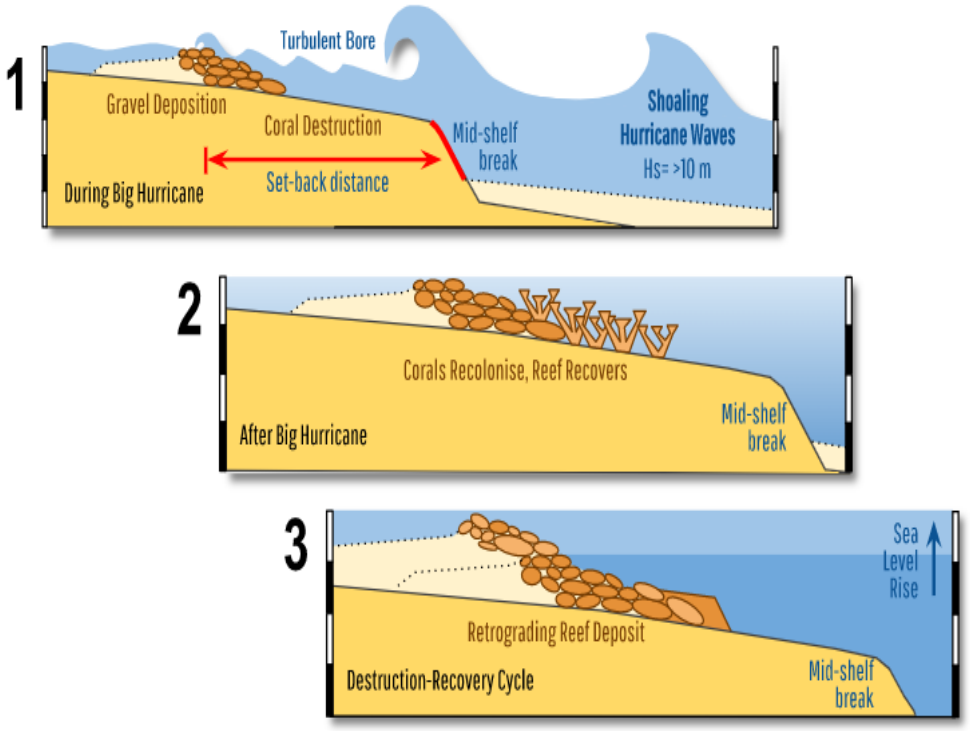

Fig. 2. Hurricane-control model. 1) Hurricane waves start to break from the mid-shelf slope break, destroying living coral colonies, transporting the clasts upslope and depositing them as a linear gravel ridge. 2) After the hurricane the linear gravel ridge is colonised by new corals as the reef recovers to its pre-storm state. 3) This destruction-recovery cycle, coupled with SL rise caused a retrogradation of the reef-crest position (crestline) during the last 5.5 ka (modified from Blanchon et al., 2017).

Although the literature on the development of Caribbean reefs is broader with more complexities than outlined above, it generally falls into these two main paradigms: 1) the original vertical accretion model, taking Macintyre & Glynn's (1976) Pamana results as the type example; and 2) the hurricane-control model, taking Blanchon et al. (2017) Punta Maroma results as the type example.

These two models highlight the fact that theories of coral-reef development have not adequately considered other controlling agents, such as the effects of hurricane effects. This was recognised by Lugo et al. (2000) who said that hurricanes play a role explaining the "complexity" of coral reefs inside the hurricane belt of the Caribbean (Fig. 3). This claim of "complexity" is related to the three-dimensional topographic complexity giving and thus the perception that vertical accretion is anything but simple. Nevertheless all previous models of Caribbean coral reef development have assumed that development is driven by simple yet different processes.

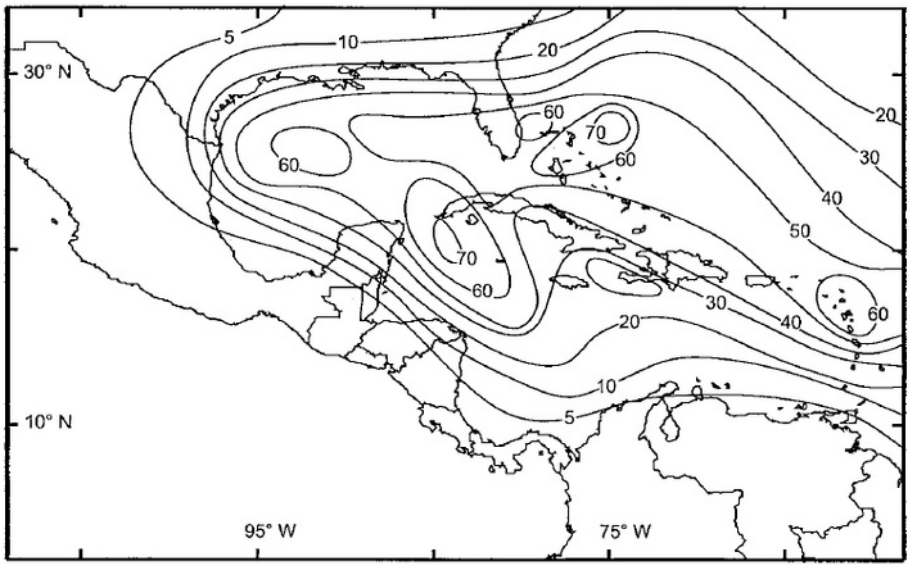

Fig. 3. Spatial distribution of hurricanes and tropical storms over the Caribbean region. Isopleths show lines of equal numbers of storms between 1871 and 1986 (taken from Lugo et al., 2000).

HYPOTHESIS

If hurricanes are a major control on the form, structure and development of Caribbean coral reefs, then a testable prediction of this hypothesis is that reefs which are protected from hurricane impact should be controlled by non-hurricane related processes, and therefore have a significantly different geomorphology, internal structure and geological development.

OBJECTIVES

General objective

Determine the geomorphology and internal structure of a fringing reef at Mahahual, which is protected from hurricanes, and identify the major processes involved in its Holocene development.

Specific objectives

1. Summarise the biogeomorphic zonation and available bathymetry.
2. Reconstruct the internal facies using drill-core transects.
3. Determine the depth and form of the underlying substrate.
4. Deduct the dominant processes responsible for reef development.

STUDY AREA

The reef at Mahahual is a detached coastal fringing reef that fronts a village of the same name (Blanchon et al., 2022), in the southeast Yucatan Peninsula, in the state of Quintana Roo, Mexico (Fig. 4A). It is in the shadow of Chinchorro Bank (Fig. 4B), and it is composed of three segments, which together extend parallel to the coast ~2.3 km (Fig. 4C).

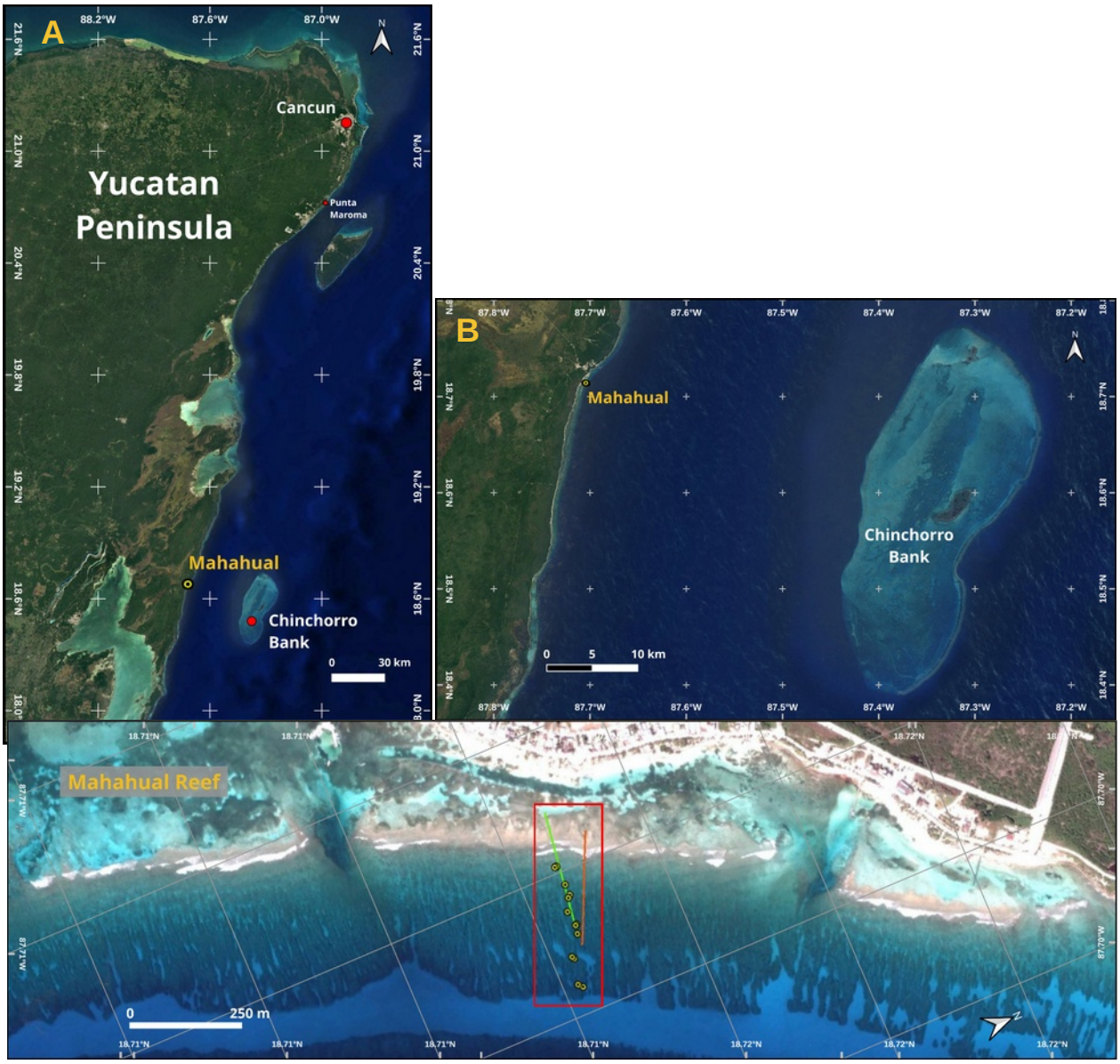

Fig. 4. Mahahual fringing reef location. A) Mahahual reef located along the southeast coast of the Yucatan Peninsula (18.715224,-87.705483°). B) Mahahual reef protected by Chinchorro Bank to the east. C) Mahahual fringing reef extension. Three parallel sections to the coast (extending from left to right ~700 m, ~1033 m and ~600 m respectively), With a total lineal reef length of ~ 2.3 km. The red polygon is the area where the field work was carried out (Images from Google Earth Pro).

To date, most research at Mahahual reef has focused on biology or ecology, but several studies have reported its general geomorphology and zonation. For example, Aguilar-Perera (1994) and Aguilar-Perera & Aguilar-Dávila (1996), classified Mahahual reef as a Barrier Reef, and divided it into north and south sections (Fig. 5a). The back-reef zones in both sections had a flat-type geomorphology without a significant slope and, in the north section a front-reef zone with low-relief coral patches (*Montastrea annularis, Porites astreoides, Porites porites and Agaricia sp.*), interspersed with gorgonians and intervening sandy areas, (between 6 to 20 m depth). In the south section, the front reef had a set of high-relief grooves with a gentle slope (between 15 to 25 m depth). Arias-Gonzáles et al. (1998) described Mahahual as a well-developed and complex Fringing Reef (FR), with the northern reef crest joined with the coast and a reef terrace width up to 30 m. They suggested it was related to the decreasing shelf width and complexity of reef development to the south, and used a general zonation typical of southern reef types with 6 zones: 1) lagoon, 2) back reef, 3) reef crest (distinguishing it from the back reef by denser coral abundance and increase in heterogeneity and diversity), 4) reef front, 5) reef slope and 6) drop-off (Fig. 5b).

Jordán-Dahlgren and Rodríguez-Martínez (2003) referred to Mexican Caribbean reefs as "extended" FRs, because it does not fit into classical Barrier Reef defined by James and Ginsburg (1979 p. 139), and is not strictly a FR which grows directly from shore. They arbitrarily divided the Mexican Caribbean margin into three sectors: northern, central and southern (Fig. 5c). They also claimed that the reef development in the southern sector is better due to a narrower shelf, typically showing a greater bottom relief in the reef front. They only report three reef zones for this sector: 1) lagoon; 2) reef crest, usually dominated by *A.palmata* with subordinate *Millepora complanata*; and 3) fore reef, dominated by S&G morphology, divided into two subzones: shallow zone (1-12 m), with spurs 3 to 7 m high and irregular grooves 3 to 6 m wide; and deeper zone (15-40 m), with long, thin spurs 5 to 12 m high and grooves 1 to 6 m wide. Ruiz-Zárate et al. (2003) by contrast, divided the fore reef into three zones according to depth: an inner fore reef (6 to up to 25 m), an outer fore reef (~15 to up to 40 m), and deep fore reef (~35 to ~50 m) terminating in a shelf-edge reef at the shelf break. They noted that Mexican Caribbean reef systems are moulded by the high frequency of tropical storms and hurricanes, but that Mahahual FR is protected in the "shadow" of Chinchorro Bank.

Nuñez-Lara et al. (2005) also describe three major zones for the Mexican Caribbean FR system: reef lagoon (back reef), crest, and reef front (fore reef), but subdivided them into five subzones based on benthic habitats: lagoon, crest, front, slope, and terrace (Fig. 9d). They described the southern reefs as semi-continuous structures, with a typical SaG system and a substrate with a complex rugosity. By contrast, Acosta-Gonzáles, et al. (2013) placed Mahahual reef in the northern part of the Mesoamerican "Barrier Reef system", and reported a well-defined zonation, composed of five geomorphic units identical to that of Nuñez-Lara et al. (2005) but with the following depth constraints: lagoon (3m depth); crest (emergent); front (5m depth); slope (12m depth); and terrace (18m depth) (Fig. 5d). This same zonation scheme used at Mahahual is widely adopted by later studies, as well as the conception of a better southern reef

development based on larger SaG systems (Rodríguez-Zaragoza and Arias-González, 2015; Martıínez-Rendis et al., 2016; Argüelles-Jiménez et al., 2020, 2021).

Although previous work on the ecology and biology of the reef at Mahahual provides only a general description of the zonation and geomorphology, there has been no effort to provide an objective or systematic description, even though reef geomorphology and zonation is an important component of the results of those investigations. Indeed, many of those descriptions are subjective, and only reproduced from previous descriptions of Mexican Caribbean reef zones or habitats.

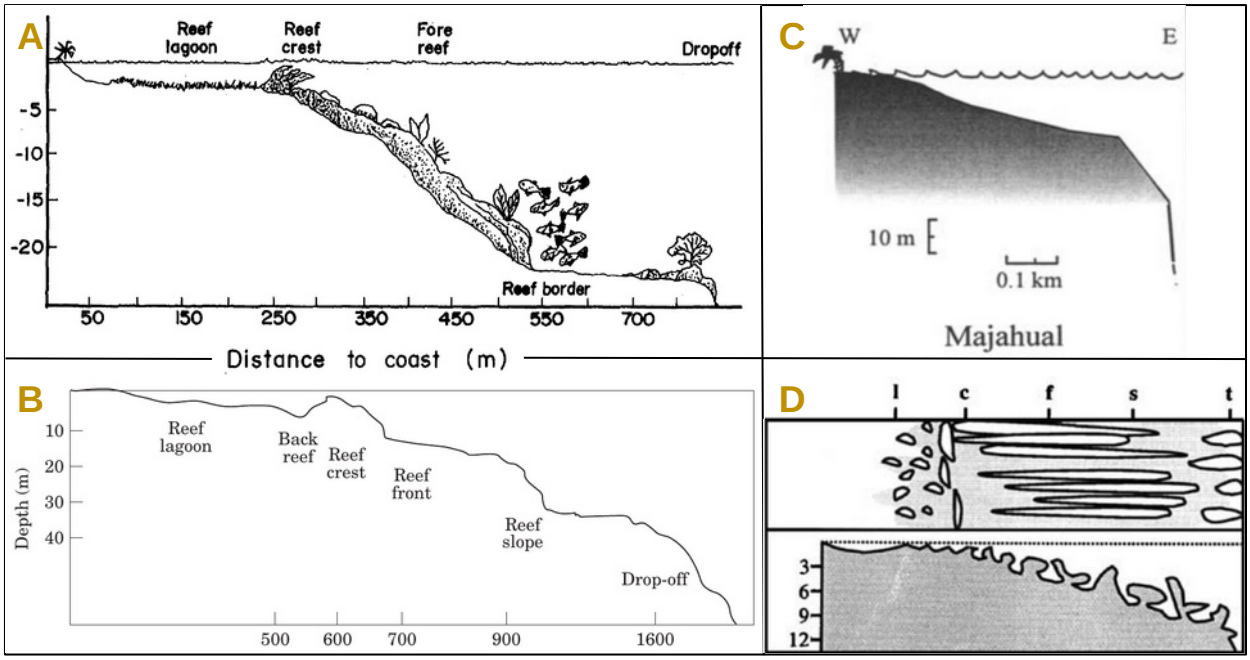

Fig. 5. Zonation and geomorphology schemes reported for Mahahual reef. A) Cross section of southern Mahahual reef (taken from Aguilar-Perera and Aguilar-Dávila, 1996). B) Cross section of a coral reef type at the southern coast of Quintana Roo, Mexico (taken from Arias-González et al., 1998). C) Profile of Mahahual reef approximately at mid reef section (modified from Jordán-Dahlgren and Rodríguez-Martínez, 2003). And D) Geomorphology at Mahahual reef, with typical habitats of FRs of the Mexican Caribbean: lagoon (l), crest (c), front (f), slope (s) and terrace (t). Depths in metres (modified from Nuñez-Lara et al., 2005).

METHODS

Bathymetry and biogeomorphology

To characterise Mahahual Reef zonation, we compile available ecologic, bathymetric and geomorphic data and combine these to produce an objective characterization of reef geomorphology. For ecological data we use Mahahual reef ecologic data transects collected between 2016 and 2019, provided by the Biodiversity and Reef Conservation (BARCO) Laboratory, from the National Autonomous University of Mexico (UNAM) and Mexican Caribbean benthic cover data from the National Commission for the Knowledge and Use of Biodiversity of Mexico (CONABIO) database (CONABIO, 2018a). The bathymetric data from Mexican Caribbean marine ecosystems was also obtained from the CONABIO database (CONABIO, 2018b). Finally, geomorphic data were derived from satellite images in Google Earth Pro and an aerial drone image provided by the Academic Meteorological and Oceanographic Monitoring Service from UNAM.

All the collected information was organised and handled using the Open Source Geographic Information System QGIS, version 3.22.4-Białowieża. The central section of Mahahual reef was the designated area where the zonation was determined, with a total area for about ~1 km^2 (FIg. 6). The available information was displayed into this area, with the bathymetric isobaths set at one metre intervals, in order to reconstruct a map of the biogeomorphic zonation of the reef and benthic zones of the shelf.

Fig. 6. Mahahual reef zonation area. The red polygon (~1 km^2) shows the designated area in which the summarised zonation map was created (image from Google Earth Pro).

Drill-Core Transects and Logging

To characterise the internal structure and composition of the reef, we obtained 13 rotary drill-cores using 1.20 m core barrel with a 10.16 cm (4") diameter carbide drill bit driven by a 3-speed hand-held hydraulic core drill (SPITZNAS®), powered by a P95 Hydraulic Power Unit (ICS®) from a small boat anchored right above the drill site, during 3 field trips between september 2021 and march 2022. The cores were taken from two parallel drill transects spaced 5 m apart over the reef front, perpendicular to the crest line (CL): Transect **A** with 8 drill sites and Transect **B** with 5 sites. Collecting cores from parallel transects replicates compositional data and therefore provides a test of lateral continuity and representativeness. All sites recorded by a hand-held GPS receptor device (Garmin® series GPSMAP® 78s). Cores were not taken over the crest and back reef due to the difficulty of drilling in unconsolidated sediments (Fig. 7).

In the laboratory, the drill-cores were cut lengthwise with a modified tile saw (RUBI DC-250), scanned at 1200 dpi. These cores were analysed and plotted on a composition log, to provide an accurate visual record of each core, using a sedimentological Reef Core Analysis Protocol (Blanchon et al. 2014). This analysis allowed us to differentiate between skeletal-framework units composed predominantly of mutually-supported in-situ corals, from detrital units composed predominantly of grain-supported clasts. The Protocol uses combinations of presence/absence indicators, in order to identify the differences (Blanchon et al., 2014; Annex A.1).

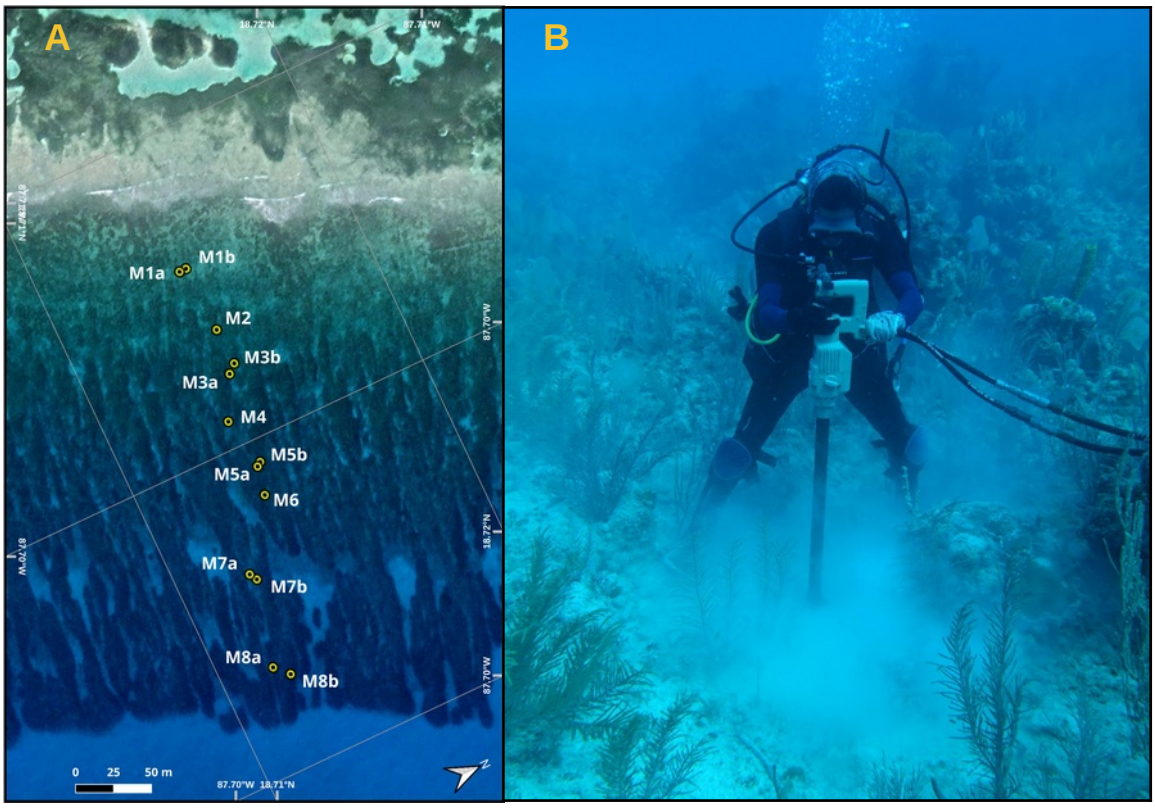

Fig. 7. Drill-Core transects. A) Location of the 13 drilled core points over the reef front in the middle of Mahahual reef structure, numbered from M1 to M8 as they separate from the crest line towards the ocean, and B) Drilling at Mahahual reef.

Electrical resistivity Imaging

Electrical resistivity (ER) is a geophysical method which uses electrical currents injected through an electrode on land or point sources on water. It uses zero frequency or direct currents. This geophysical method uses the physics of the electrical currents into complex geological media with different resistivities. In this research is used to estimate the subsurface variation in the bulk electrical resistivity. Both electrical resistivity (ρ) and its reciprocal electrical conductivity (σ), are related to rock type, grain size, porosity, pore-fluid conductivity, saturation and temperature. The technique has been used among others to obtain lithology images, location of clays, and groundwater fluid conductivity (Singha et al., 2022). Here the technique is referred to as electrical resistivity imaging (ERI) but is also known as electrical resistivity tomography (ERT).

Electric current is conducted through a geological media (rocks) in three ways: electrolytic, electronic (ohmic), and dielectric conduction. Electrolytic conduction occurs in aqueous solutions that contain free ions, electronic conduction is typical of metals, and dielectric conduction occurs in poor conductors (or insulators) which contain no free electrons (Reynolds, 1997; Lowrie, 2007). In most rocks, conduction results from pore fluids acting as electrolytes (electrolytic conduction), with mineral grains contributing little to the overall conductivity of the rock (except where they are good electrical conductors). Igneous rocks tend to have high resistivities, metamorphic rocks have intermediate but overlapping resistivities, and sedimentary rocks tend to be the most conductive (low resistivities), largely due to their high pore fluid content. Given variable grain composition and presence of facies in sedimentary rocks, resistivity accurately reflects the varying proportions of these constituents (Reynolds, 1997).

When current is injected into the subsurface between two electrodes or point sources, the receiving electrodes (or Potential electrodes) measure both a positive and negative charge (the Current electrodes), as well as the resultant electric potential (the voltage difference; Fig. 8).

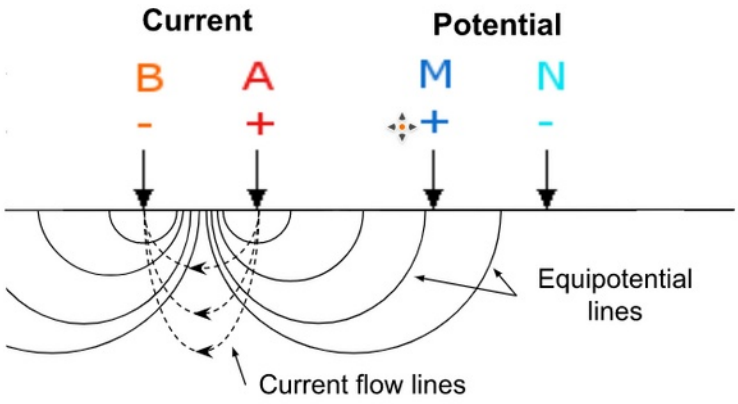

Fig. 8. Four electrode common configuration for electrical resistivity survey. B and A represent the current electrodes, used to drive current into the subsurface; while M and N the potential electrodes, measure the resulting voltage difference (modified from Gomez-Nicolas, 2014).

The fundamental physical law used in resistive surveys is Ohm's Law, which governs the flow of current in the ground. The equation for Ohm's Law in vector form for current flow in a continuous medium is given by (Loke, 2001):

$$J = \sigma E \tag{1.1}$$

where **J** is the current density vector and **E** is the electric field intensity vector. In practice, what is measured is the scalar electric potential and its relationship with the field intensity, which can be expressed as the gradient of a scalar potential (Telford et al., 1990; Loke, 2001):

$$E = -\nabla V \tag{1.2}$$

Combining equations (1.1) and (1.2), we get:

$$J = -\sigma \nabla V \tag{1.3}$$

If the current source is found in a point source over a heterogeneous half-space where conductivity varies in (x, z) and the scalar potential varies in (x, y, z; Dey & Morrison, 1979):

$$\nabla \sigma . \nabla V + \sigma \nabla^2 V = [-] \delta(x - x_s) \delta(y - y_s) \delta(z - z_s) \tag{1.4}$$

where δ is the Dirac delta function.

$$\nabla \sigma(x, z) . \nabla V(x, y, z) + \sigma(x, z) \nabla^2 V(x, y, z) = [-] \delta(x - x_s) \delta(y - y_s) \delta(z - z_s) \tag{1.5}$$

Equation (1.5) represents the basic equation that gives the electrical potential distribution in the ground due to a point-source current (Loke, 2001). Many methods have been used to solve this differential equation depending on the level of complexity, this is known as "forward" modelling. In the simplest case, a homogeneous and isotropic medium and a single point-source current on the ground surface, the potential is given by (Telford et al., 1990; Loke, 2001):

$$V = \frac{\rho I}{2\pi r} \tag{1.6}$$

where r is the distance of a point in the medium from the electrode. Given that in a field resistivity surveys use a typical arrangement with four electrodes (Fig. 4). It is not typical to measure two potentials, but the potential difference that is given by (Telford et al., 1990; Reynolds, 1997; Loke, 2001; Lowrie, 2007):

$$\Delta V = \frac{\rho I}{2\pi} \left[\left(\frac{1}{AM} - \frac{1}{BM} \right) - \left(\frac{1}{AN} - \frac{1}{BN} \right) \right] \tag{1.7}$$

Apparent resistivity: Apparent resistivity (ρa) is defined as the resistivity that the subsurface would have if it were not homogeneous. This can be calculated by rearranging the terms in equation (1.7), to obtain resistivity (Telford et al., 1990, Singha et al. 2022):

$$\rho_a = 2\pi K_g (\Delta V/I) \tag{1.8}$$

where K_g is a geometric factor that depends on the electrode configuration used in the survey. This is the parameter that converts a measured resistance (calculated from the voltage differences (ΔV), divided by the applied current (I) in the survey, (R = ΔV/I)), to apparent resistivity, assuming a homogeneous and isotropic half space (i.e., the same electrical conductivity in the earth to infinite distance below a surface boundary) without any electrical source, K_g for every quadrupole can be calculated for different surface arrays by means of equation:

$$K_g = \frac{2\pi}{\frac{1}{\overline{AM}} - \frac{1}{\overline{AN}} - \frac{1}{\overline{BM}} + \frac{1}{\overline{BN}}} \tag{1.9}$$

where $\overline{AM}$, $\overline{AN}$, $\overline{BM}$, y $\overline{BN}$ are the distances between electrodes A and M, A and N, B and M, and B and N, respectively (Fig. 4). In summary, the geometric factor accounts for the arrangement of electrodes and allows an apparent resistivity to be calculated (Singha et al. 2022).

Electrode arrays: Of the existing different types of arrays, three standard array types commonly used in field surveys are utilised: 1) dipole-dipole array, 2) Wenner array, and 3) Schlumberger array. All arrays deploy electrodes in a straight line called x-direction.

1) Dipole-dipole array (DD)

In this array, the potential electrodes are closely spaced to each other, but far from the current electrodes, which are also close to each other (Fig. 9a). It is mainly characterised for its sensitivity to lateral changes in electrical resistivity, implying its use to map structures with lateral heterogeneity (Telford et al., 1990; Loke, 2001; Singha et al. 2022).

2) Wenner array (W)

The electrodes in this array are evenly spaced from each other (Fig. 9b), and are characterised by being relatively sensitive to vertical contrasts in subsurface resistivity below the centre of the array. Therefore the Wenner array is a good option to resolve vertical heterogeneity (Telford et al., 1990; Loke, 2001; Singha et al. 2022).

3) Schlumberger Array (S)

Although Schlumberger has similarities with the Wenner array in the arrangement of the electrodes, the current electrodes are spaced much further apart than the potential electrodes

(Fig. 9c). This array is characterised by being moderately sensitive to both horizontal and vertical heterogeneity (Telford et al., 1990; Loke, 2001; Lowrie, 2007).

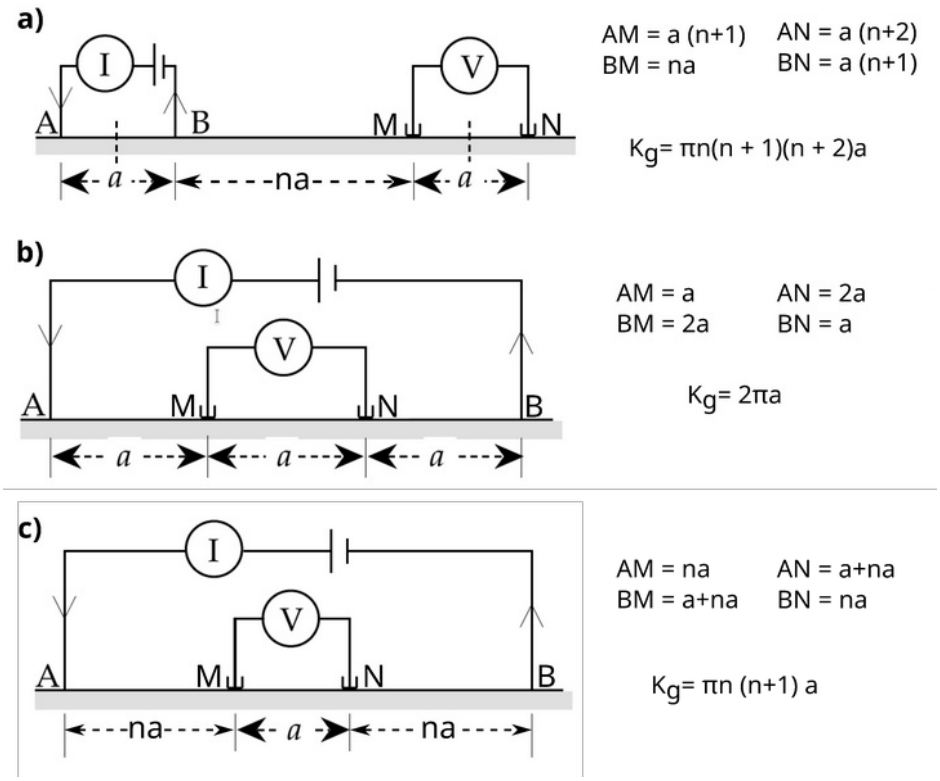

Fig. 9. Types of electrode arrays. a) dipole-dipole array, where a= dipole length and n= spacing factor; b) Wenner array, where a= spacing between electrodes; and C) Schlumberger array, where a= spacing between potential electrodes, the "n" factor is the ratio of the distance between the electrodes AM (or NB) to the spacing between the pair of potential electrodes MN. The values of the distances between electrodes AM, AN, BM and BN, are shown in front of each array, substituting them in equation (1.9), they give the corresponding K_g for each array (modified from Lowrie, 2007).

Data Inversion: The objective of inverting an electrical resistivity dataset is to recover a subsurface distribution of electrical resistivity (Fig. 10), that is, the measured data are inverted to obtain a spatially discretized distribution (i.e., gridded or meshed) of the electrical properties of the subsurface. The general procedure for inverse modelling consists of the following steps (Singha et al., 2022):

1) Starts with a distribution of electrical conductivity (usually a homogeneous starting model corresponding to the average apparent conductivity measured in the field);

2) A forward simulator is used which, for the given distribution of electrical conductivity, calculates predicted data using equation (1.7);

3) The misfit between the predicted and observed data is calculated, as well as a measure of the complexity of the electrical conductivity distribution; and

4) If the misfit between the data is less than our stopping criteria, the process stops and the current subsurface distribution of electrical conductivity is accepted as the final result.

Otherwise, the model is modified to improve the fit and returns to step 2. This way we can recover the resistivities underground in the x-direction and depth (z-direction) or two-dimensions (x, z).

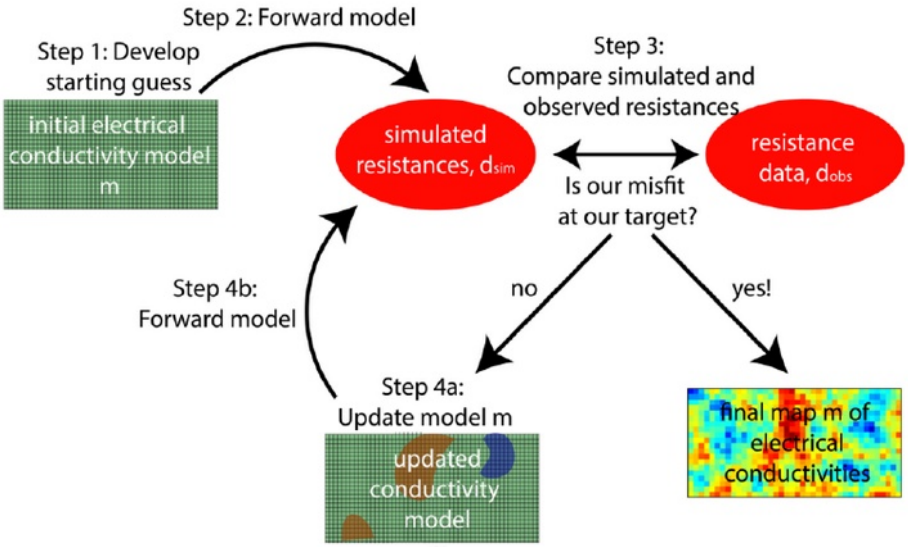

Fig. 10. Simplified representation of the inversion process (taken from Singha et al., 2022)

The ERI method has several limitations and local variations in the resistivity measurements, among which are: the need for direct contact of electrodes with the surface; significant effort and time in the field only for deployment of electrode array; slow data collection limits the number of different measurements in the field (Singha et al., 2022). In addition, terrains with complex surface relief can distort resistivity measurements: in valleys and depressions the current flow is concentrated or focused (large measured ΔV, in consequence a large ρa, equal to high resistivity), whereas beneath a ridge or hill flow is dispersed or diverged (lower measured ΔV, in consequence a lower ρa, equal to low resistivity). This current flow behaviour results in distorted equipotential surface, producing false anomalies and may distort or mask a real anomaly (Fig. 11). This terrain effect increases with surface relief, but is insignificant for slopes of less than 10°. To deal with those distortions, a finite-element numerical method has been used for solving equation (1.5) in two-dimensions (x, z), because it offers more flexibility for matching irregular boundaries (Holcombe and Jiracek, 1984; Telford et al., 1990).

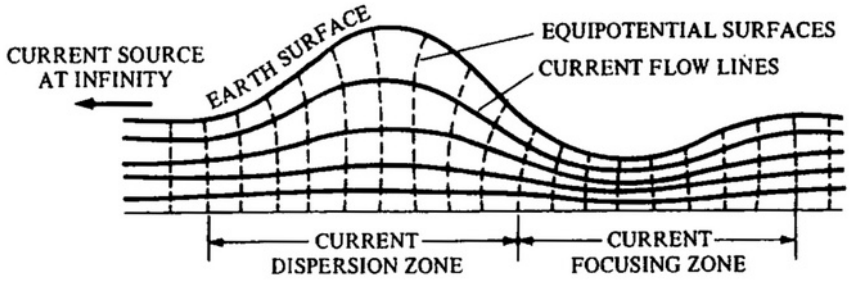

Fig. 11. Distortion of uniform field by ridges and valleys (taken form Telford et al., 1990)

Survey Protocol

To delineate the form and position of the bedrock beneath the reef structure, its resistance to the flow of an electric current (resistivity) was measured along 2 transects (T1 and T2) perpendicular to the CL, by laying a 56 passive-graphite electrode cable, with a factory spacing of 5 m between electrodes, giving a total length of 275 m, between August 9 and 11, 2022. The instrument used for the measurements was a SuperSting R8/IP® from Advance Geoscience, Inc. (AGI), UNAM property (Inventory No. 02469841), acquired by the National Coastal Resilience Laboratory (CONACYT project 271544) and currently located in the Laboratory of Engineering and Coastal Processes of the Engineering Institute of the same university. From now on, the instrument will be simply referred to as the SuperSting.

In both transects, the cable was laid over the seabed, as straight as possible, from the middle of the reef front at 8 m depth, to the back-reef flat, around 10 cm depth, where the boat was anchored with the remaining instruments for the survey. T1 was placed as close to the drill transect as possible, whereas T2 was collected across the reef-front to the north of the drill transect. In both transects, the cable was weighted with concrete-filled cylinders to ensure that electrodes or point sources were in contact with the seabed (Fig. 12 and 13).

In order to maximise data collection, the resistivity data was measured using three types of electrode arrays: DD and S in Transect 1 (**T1**) and DD, S and W in Transect 2 (**T2**), with the number of arrays used for each transect determined in the field according to the available time given the weather conditions on the day of the survey. Parameters selected in the SuperSting to carry out the surveys are shown in Table 1. Additionally, a bathymetric profile was obtained, by measuring the depth of each electrode site with a PLASTIMO Echotest II hand-held echo sounder.

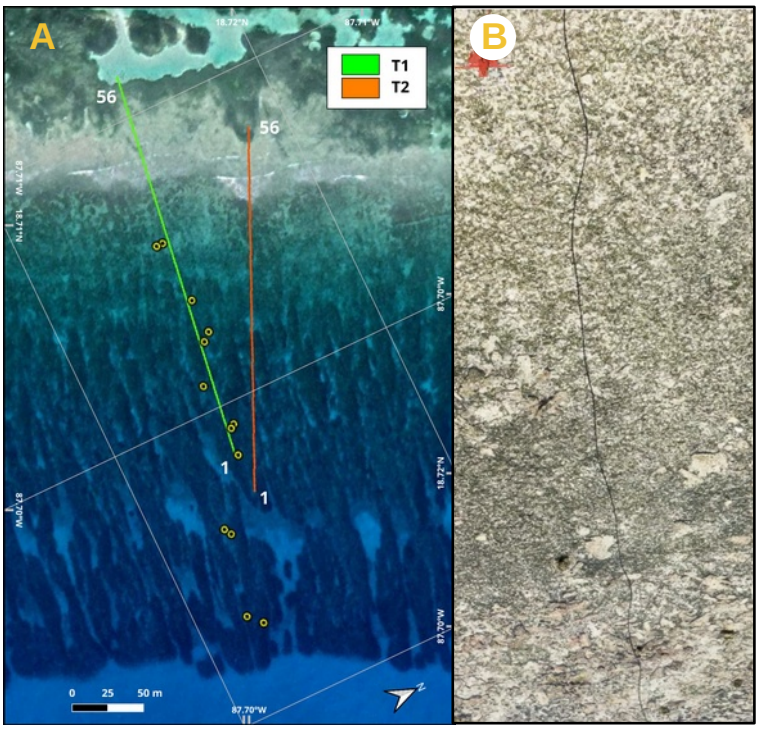

Fig. 12. Electrical survey transects. A) Location and track of the two electrical resistivity transects. Numbers represent the cable electrodes laid over the middle of the Reef Front, onto and over the CL and into the Back Reef. T1 was laid as close to the drilled-core transect as possible, but due to the roughness of the seabed it was not possible to lay them straight. Therefore, some suboptimal contacts between the electrodes and the sea bed could have been present. B) Aerial view of the cable laid over the Back Reef, same orientation as the map, highlighting the difficulty of laying the cable straight.

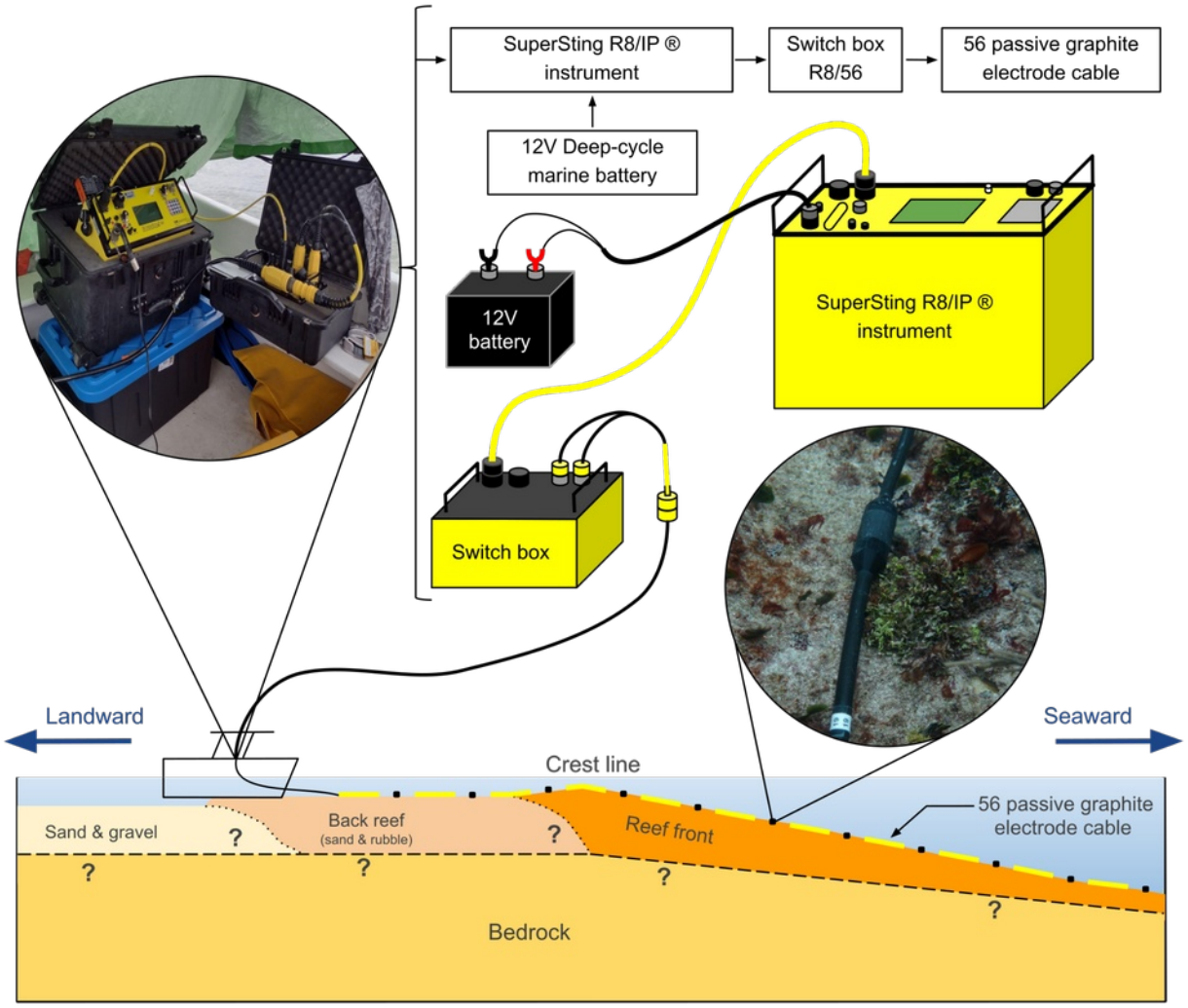

Fig. 13. Idealised schematic representation of electrical resistivity survey. Upper diagram shows the equipment assembly in a small boat: SuperSting powered by a 12V deep cycle marine battery, plugged-into a switch box and this in turn to the 56 passive graphite electrode cable. Lower panel illustrates the laying of the cable over the reef surface. The schematic is not to scale and does not show the actual internal structure (modified from Islas-Domínguez, 2020).

Table 1. Electrical resistivity survey settings used for each electrode array in the SuperSting for both transects. ES= electrode spacing.

Array	Number of electrodes	Max n	Max a	Max AB/MN	Expansion Factor	Include reverse array	ES (m)
DD	56	8	3	-	-	Yes	5
S	56	-	-	9	4	No	5
W	56	-	-	-	8	No	5

Data Inversion

Data inversion process was done using the proprietary software AGI EarthImager 2D Version: 2.4.4 with licence of the Ensenada Center for Scientific Research and Higher Education (CICESE). For this process, a merged file was obtained, with all the available data in each transect, thereby increasing the number of data for the inversion model. In turn, each merged file was trimmed to a depth of 18 m in order to highlight more detail of shallow features. The processing protocol for both transects, was conducted as follows:

1) The desired settings for the data inversion were selected (Table 2, Annex B.1). Within these, the Criteria for Data Removal filters the raw data. The Forward Modelling section solves equation (1.5) from a selected method. The Inversion Method section imposes additional constraints or regularizations to the result of the inverse modelling in order to single out one optimal solution. And the Stop Criteria section sets rules that stop the iterations (AGI EarthImager 2D, 2009).

2) The merged data file was loaded, followed by the bathymetry file (.uwt file, Annex B.4). The resistivity value for the water column was omitted because setting a unique value forces the model to produce inversion artefacts in order to fit the resistivity values to the water column values (Annex B.4). It is important to sign out that EarthImager inversion software knows that electrodes are underwater when we give it the bathymetry file.

Table 2. Summary of the selected settings. All the settings in the Criteria for Data Removal were set in a safe range within the recommended values, with exception of the Max. Reciprocal Error setting, which after a thorough analysis of the reciprocal raw data, it was concluded that setting this parameter in a small value turned out to be an unnecessary removal of data due to the nature of the data itself. (For a complete settings descriptions and justification of selection, see Annex B.1 to B.3)

Criteria for Data Removal	**Forward Modelling**
Min. Voltage= 0.02 mV	Finite element method
Min. abs(V/I)= 2x10-5 Ohm	**Inversion Method**
Max. Repeat Error: 3 %	Smooth Model Inversion
Min. App. Res.= 0.03 Ohm-m	**Stop Criteria**
Max App. Res= 10000 Ohm-m	Number of Iterations= 8
Max. Reciprocal Error= 10000%	Max RMS Error= 5%
Remove Neg Res= Yes	L2 Norm= Yes

From points 3 to 11, EarthImager software automatically performs the following steps:

3) With the measured raw data of current and voltage, together with the geometric factor, ρa is calculated (equation 1.8 but considering that electrodes are underwater).

4) A starting resistivity model is constructed based on the average distribution of ρ_a.

5) From the starting resistivity model, the forward modelling process is carried out, solving equation (1.5) by the finite element method. This is because the triangular mesh of finite element method is very flexible to deal with topographical variations like the ones from the .uwt file. The predicted ρ_a is obtained (Annex B.2).

6) The initial root mean squared (RMS) error is calculated, a measure of data misfit, whose main objective is to characterise the degree of misfit between the measured data in the field (ρ_a) and the initial calculated (predicted ρ_a) (see annex B.3.1).

7) The inversion problem is solved from the previous model (predicted ρ_a). Since the inversion problem solution is *not* unique, the software allows us to impose additional constraints/normalizations on the model, in order to single out one optimal solution. The Smooth Model Inversion (SMI) method was chosen, which is based on the assumption of Gaussian distribution of data errors. Its objective is to find the smoothest possible model, whose response fits the data to an a-priori Chi-squared statistic. The objective function of the SMI is given by (AGI EarthImager 2D, 2009):

$$\mathbf{S(m)} = (\mathbf{d}_{obs} - g(\mathbf{m}))^T \mathbf{W}_d (\mathbf{d}_{obs} - g(\mathbf{m})) + \alpha \cdot \mathbf{m}^T \mathbf{Rm}$$

where $\mathbf{d_{obs}}$ is the measured data, **g(m)** is the calculated data, $\mathbf{W_d}$ is a data weighting matrix**,** **α** is a Lagrange multiplier and a stabilising factor (determines the amount of roughness imposed on the model during the inversion), and **R** is a roughness operator.

8) The model is updated with the $\rho_{a\ i+1}$ obtained from the inversion process, where i is the corresponding iteration number.

9) Forward modelling runs again, based on the updated model (ρ_{ai}) to obtain a new predicted ρ_{ai+1}.

10) A new RMS error value is calculated between ρ_a and predicted $\rho_{a\ i+1}$.

11) The process continues (steps 3 to 10) until any of the inversion stop criteria is satisfied (Table 2).

12) Finally, a single colour scale was used to obtain an appropriate visual comparison between both models (Table 3).

Table 3. Unified colour scale.

#	Resistivity value (Ohm-m)	Colour
1	0.15 - 0.204	
2	0.204 - 0.240	
3	0.240 - 0.340	
4	0.340 - 0.420	
5	0420 - 0.609	
6	0.609 - 1.000	
7	1.000 - 1.440	
8	1.440 - 1.838	
9	1.838 - 2.346	
10	2.346 - 3.000	

RESULTS

Biogeomorphic zonation and bathymetry

The available public-domain data for Mahahual reef provides a general view of its surface geomorphology and benthic zonation (Fig. 14). Using retrospective satellite images from Google Earth, we delineate reef geomorphology by first identifying the Crestline (CL), where waves break, and then use this to identify two main zones: a landward back-reef (BR) unit, and seaward a reef-front (RF) unit. Combined, these units constitute the reef deposit (Fig. 16).

Landward of the CL, the BR unit is a ~60 m wide sub-horizontal intertidal flat bounded by an irregular slope break into the lagoon where water depths are ~2 m deep and exceed the normal intertidal range (~20 cm). The presence of this back-reef flat designates the reef as a 'detached Flat-type Coastal FR' (Blanchon et al., 2022). The flat can be subdivided into an upper BR zone which consists of a coarse-sediment substrate with cobble sized coral clasts (Macroalgae in Fig. 14C), and a lower zone with skeletal sand-and-gravel substrate colonised by seagrass (Sediments and Seagrass in Fig. 14C).

Seawards of the CL, the RF zone is subdivided based on the character of the benthic substrate into:

1) Upper RF zone, from ~0 to 3 m depth (breaker zone), is a ~90 m-wide zone characterised by coral stumps and rubble (drone image, Fig. 14A), and a benthic assemblage consisting of: algae mat and sediment (53.7%); macroalgae (23.5%); CcA (11.9%); hard corals (7.4%); others (1.6%); substrate (1.0%); invertebrates (0.6%); and hydrocorals (0.4%). In terms of hard corals this zone is principally composed of: *P. astreoides* (77.3%); *P. strigosa* (8.4%); and *A. palmata* (6.6%), which together account for >90% of the cover (Fig. 15A)

2) Middle RF zone, from ~3 to 8 m depth, is a ~140 m-wide zone characterised by spurs and grooves with a frequency of one spur every 14.6 m, and a benthic assemblage consisting of: algae mat and sediment (31.8%); macroalgae (26.1%); hard corals (14.5%); CcA (8.9%); others (6.4%); invertebrates (6.1%); octocorals and hydrocorals (3.5%); and substrate (2.7%); (Fig. 15B). In terms of hard corals this zone is mainly composed of: A. tenuifolia (20.2%); P. astreoides (19.1%); A. agaricites (18.7%); O. faveolata (14%); S. siderea (13.5%); and O. annularis (4.6%), which together account for >90% of the cover (Fig. 15B).

3) Lower RF zone, from 8 to 13 m depth, is a ~100 m-wide zone characterised by spurs and sand-filled grooves with a frequency of one spur every 21.8 m, and a benthic assemblage consisting of: algae mat and sediment (39.0%); macroalgae (27%); hard corals (14.0%); CcA (10.7%); invertebrates (5.9%); others (1.5%); octocorals (1.1%); and substrate (0.8%) (Fig. 15C). This zone is bounded on seaward by a slope-break (RF Break) at ~345 m, which levels into a sand terrace starting at 13 m below SL (Fig. 16). In terms of hard corals this zone is largely composed of: A. agaricites (22.3%); O. faveolata (17%); P. astreoides (15%); P. porites

(14.9%); O. annularis (12.9%); S. siderea (5.8%); and D. cylindrus (1.9%), which together account for 90 % of the cover.

The hard coral assemblage in the Upper RF zone has branching and mound/head corals, whereas the Mid and Lower RF zones have laminar and mound/head corals.

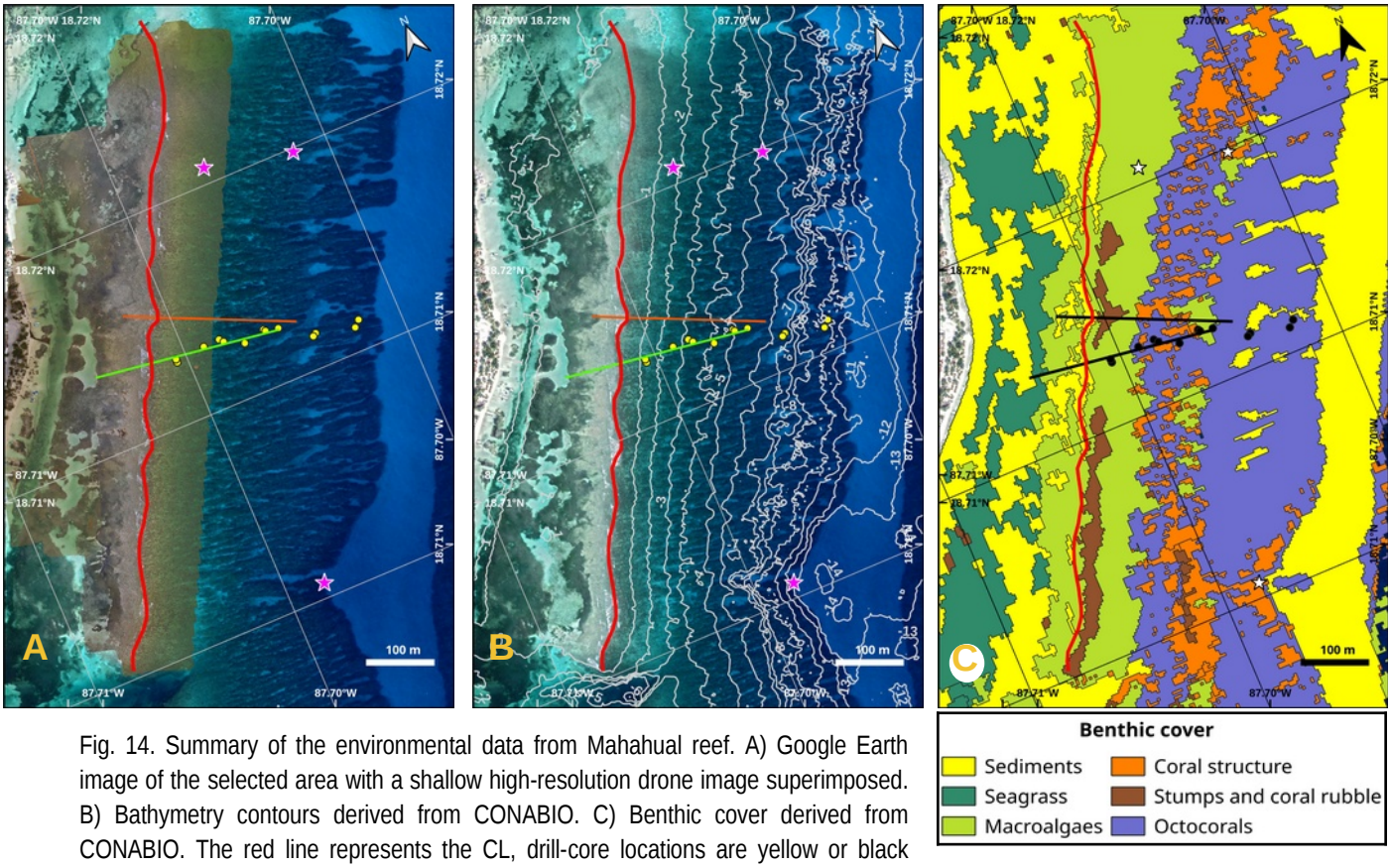

Fig. 14. Summary of the environmental data from Mahahual reef. A) Google Earth image of the selected area with a shallow high-resolution drone image superimposed. B) Bathymetry contours derived from CONABIO. C) Benthic cover derived from CONABIO. The red line represents the CL, drill-core locations are yellow or black points, ERI transects are green, orange and black lines, and ecological transects are purple or withe stars.

The CONABIO survey in the area shows that the benthic cover is composed of: macroalgae (40%); sediments (32 %); seagrass (13%); octocorals (11%); coral structure (2.5%) and stump and coral rubble (1.4%) (Fig. 14.C). Both the CONABIO and the transect coverage data are similar, showing a high proportion of macroalgae and sediment. Transect E1, was the most similar to the CONABIO benthic cover representation (macroalgae in that spot), due to its large cover of macroalgaes (23.5%). While transects at E3 and E4 did not coincide with the octocorals/coral structure benthic cover from CONABIO, and were instead both dominated by macroalgae 36% and 44%, respectively (Fig. 14C and 15B & C).

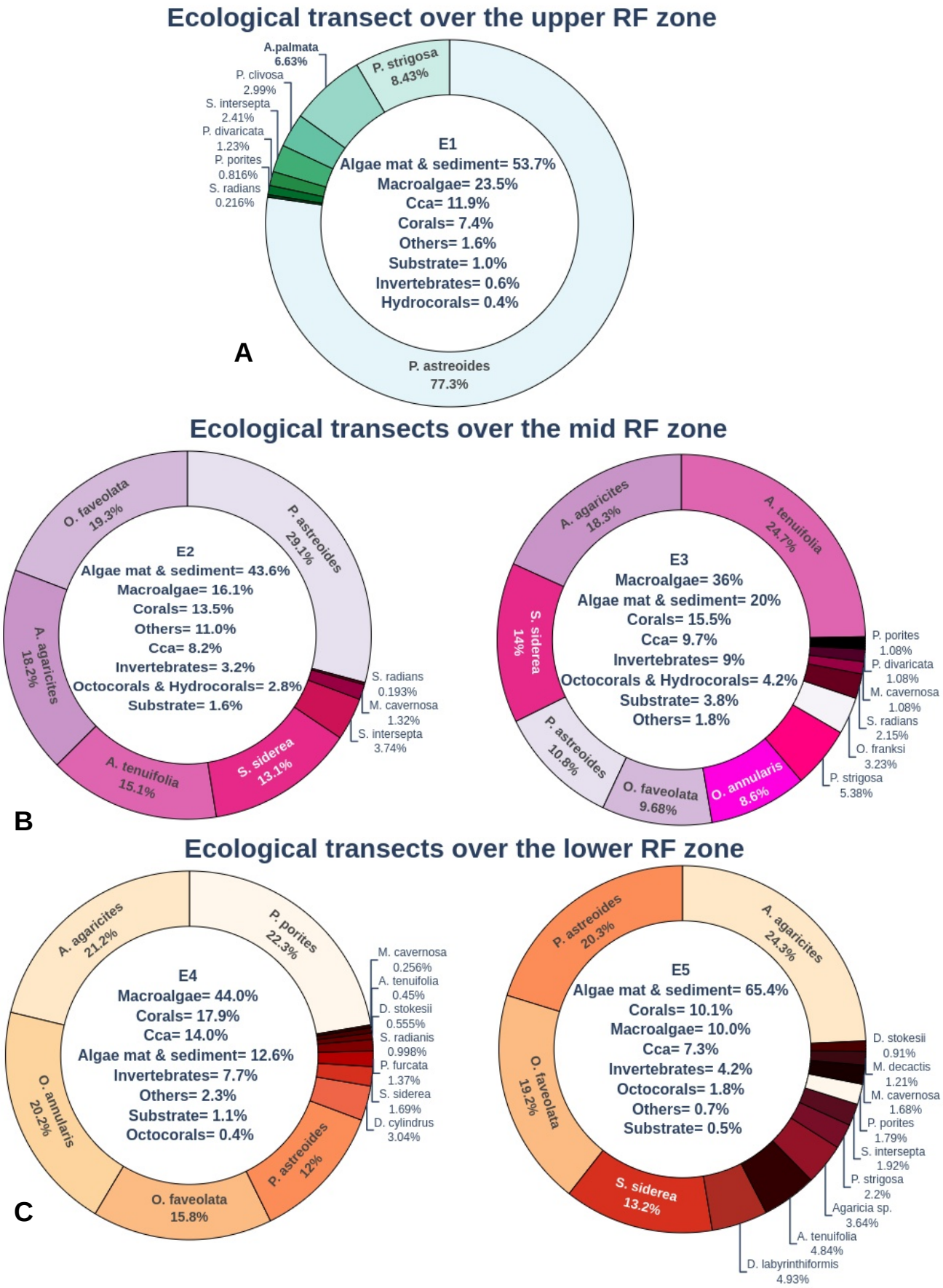

Fig. 15. Hard coral assemblage obtained from ecological transects. A) Coral assemblage in the upper RF zone, B) Coral assemblage in the mid RF zone, and C) Coral assemblage in the lower RF zone. Location of three transects (E1, E3 and E4) are shown as stars in Fig. 14 & 16, the other two are outside the selected area. E#= number of ecological transects.

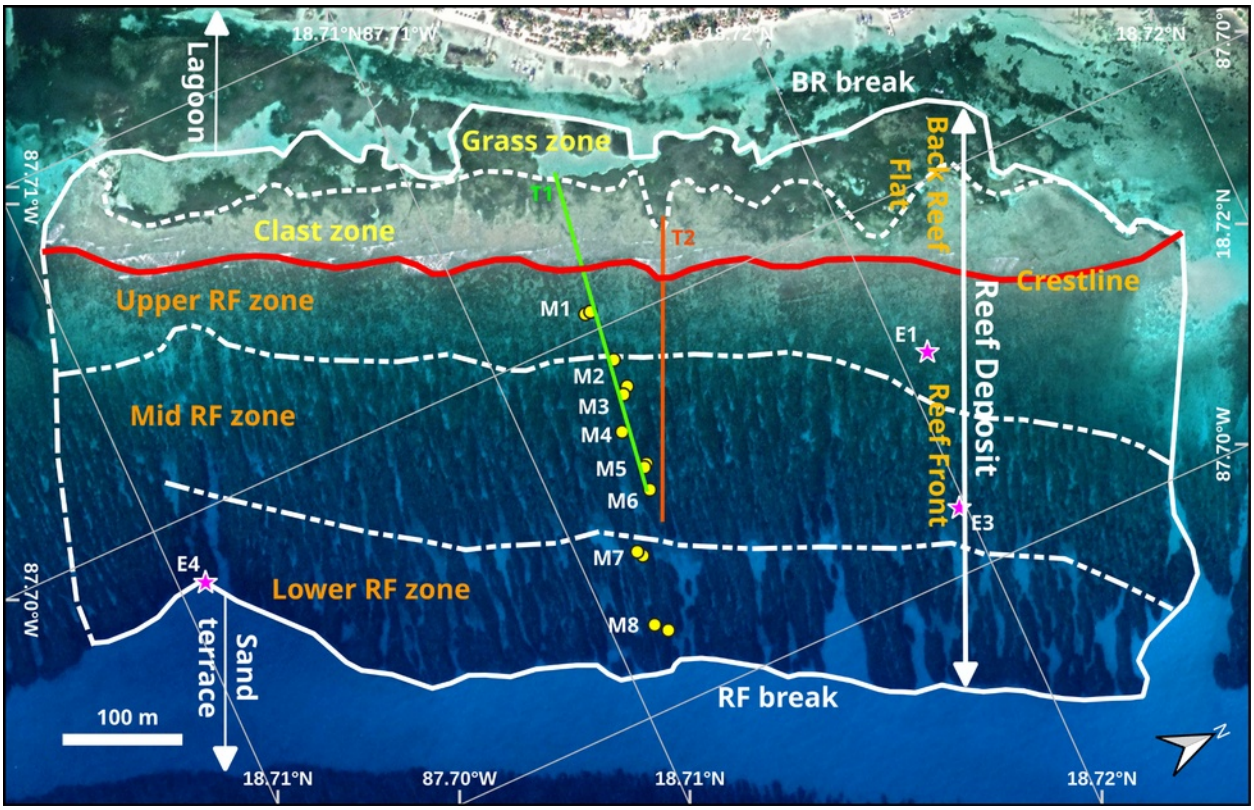

Fig. 16. Biogeomorphic zonation of the fringing reef at Mahahual. Reef geomorphology is divided into two zones by the CL (red line): 1) landward BR flat, around ~20 cm depth, with two subzones: clast zone (surf zone) and grass zone. And 2) seaward RF, with three subzones: Upper RF zone, between ~0 - 3 m depth (breaker zone); Mid RF zone, between ~3 - 8 m depth (spur and groove zone); and Lower RF zone, between ~8 to 13 m depth (spur and sand zone). The drilled-cores are represented as yellow dots, T1 and T2 represent the ERI transects, and the stars represent the ecological transects.

Internal Composition

The internal structure and composition of the reef is reconstructed from two transects totalling 13 drill cores recovered from the reef front between 2 to 11 m isobaths (Fig. 17). The cores are largely unconsolidated and composed of a combination of unaltered aragonitic coralagal skeletons and their sedimentary detritus. Based on these characteristics, and a lack of evidence of subaerial exposure (root casts, mineral phase inversion etc), they are assumed to represent the modern reef unit that has developed during the last few thousand years of the Holocene.

The cores were divided according to composition into two depth-related facies units: a lower unit with 7 cores, M5a to M8b, between 11 to 6 m below SL; and a upper unit with 6 cores, M1a to M4, from depths between 6 and 2 m below SL (Fig. 18 and 19). In both, the cores were obtained mainly from low points in the substrate, in order to obtain the maximum recovery. Unfortunately and despite the 2.2 m depth of maximum recovery in core M6, it was not possible to reach the underlying bedrock due to suboptimal down-hole conditions related to the increasing presence of unconsolidated sand that collapsed into the hole preventing drilling.

Lower facies: This unit has 7 cores, from M5a to M8b, and consists of a head-coral framestone with interstitial rubble. The framework is predominantly a growth sequence of small/medium *in-situ* colonies of head corals, less than 70 cm high, composed of *S. siderea* (21.6%)*, O .annularis* (11.99%)*, M, cavernosa* (10.4%)*, P. astreoides* (4.9%)*, P. strigosa* (4.7%) *and A. agaricites* (1.2%). This coral assemblage shows typical *in-situ* indicators, such as basal attachment surfaces, up-oriented coralites and consistency in orientation (Blanchon et al., 2014). Colonies show signs of a moderate bioerosion, mostly along the basal colonie margins, which overhang small cavities (M5a and 6). The bioerosion consists of a macro-borer assemblage of polychaetes, Trypanites isp., bivalves, Gastrochaenolites isp., and the sponge Entobia isp., all in ample quantities. Encrusting the bioeroded coral margins, are thin to medium (<1mm to <1cm thick) layers of crustose coralline algae (Cca), and above or within it, both low- and high-relief *Homotrema rubrum*, as well as vermetids gastropods and serpulid worm tubes.

The other component of this unit is interstitial unconsolidated or partially cemented skeletal gravel with a sand matrix between the colonies of the framework. Fragments include *O.annularis, A. cervicornis, P. strigosa, P.astreoides, M, cavernosa, S.siderea, and Agaricia sp.* These coral clasts show a large degree of bioerosion, reaching a heavy intensity, causing difficulty in fragment recognition. Many coral clasts are well cemented and form a rudstone texture, with the exception of M5b where loose coral gravel is found, also with the same suite of encrusters. (Fig. 19, Annex A.2.7 to 2.13).

This unit is formed by a sequential growth of small/medium *in-situ* head-corals, principally *S. siderea and O .annularis*, consistent with low energy conditions, which developed 2.2 m of framework accretion (M6). The rubble-filled gaps between the colonies are consistent with higher energy events which destroyed fragile colonies.

Upper facies: The upper unit with 6 cores, M1a to M4, consist mainly of coral rubble with patches of *O. annularis* framework. The coral rubble is present in almost all the cores in this unit, with exception of M1a, and it is composed of a gravel to boulder sized clasts with an unconsolidated sand-size matrix filling the interstices. In some cores the clasts are cemented but the degree of cementation is reduced with the depth (M3a). Identifiable clasts were, from major to minor proporcion: *P. strigosa, A. palmata, O. annularis, A. cervicornis, M. cavernosa, A. agaricites and P. astreoides*. Most clasts are highly bioeroded surfaces with the presence of the same macroborer assemblage, abundant Trypanites isp., Gastrochaenolites isp., and Entobia isp. In addition to the macroborers, encrusters include Cca layers, with a thickness between < 1 mm to less than 2 cm, both low and high relief *Homotrema rubrum*, vermetids, and serpulids.

As for *O.annularis* framework lenses were only found in half of the cores: M1a, M3b and M4, and it was clear that the coralites and therefore the coral framework was up-oriented (*in-situ*), also basal attachment surfaces were present and some colonies show lack evidence of fragmentation. Nevertheless, the lenses show a minimal bioerosional surfaces with a minor proportion of the macroborers Trypanites isp., Gastrochaenolites isp., and Entobia isp, a cryptic Cca with more than 3cm thick, grew at the base of M1a. Only in M3b a cavity was present, as well as exposed Cca, > 1mm and < 2 cm, with both low and high relief *Homotrema rubrum*, vermetids, and serpulids (Fig. 18, Annex A.2.1 to 2.6).

The interpretation of this unit is a sandy coral gravel patchily colonised by *O. annularis* framework, being the composition of the coral gravel section corresponds with the typical ranges of the living corals. The primary coral rubble in the cores M3a, M3b and M4, are mound/head corals: *P. strigosa* and *O.annularis* in a depth range of recovery between 4 and <6 m. In contrast, the predominant coral rubble in the remaining cores, M1b and M2, are branching corals: *A. palmata* and *A. cervicornis* in a depth range of recovery of 4m up, coinciding with the high energy surf zone of the reef. And according to the main framework builder of the reef described before, the only *in-situ* present colonies are *O.annularis*. Therefore, the unit is the result of coral destruction by wave energy due to the shallow depth zones where they are emplaced, forming a vast gravel layer of different coral species between the dispersed *O.annularis* colonies.

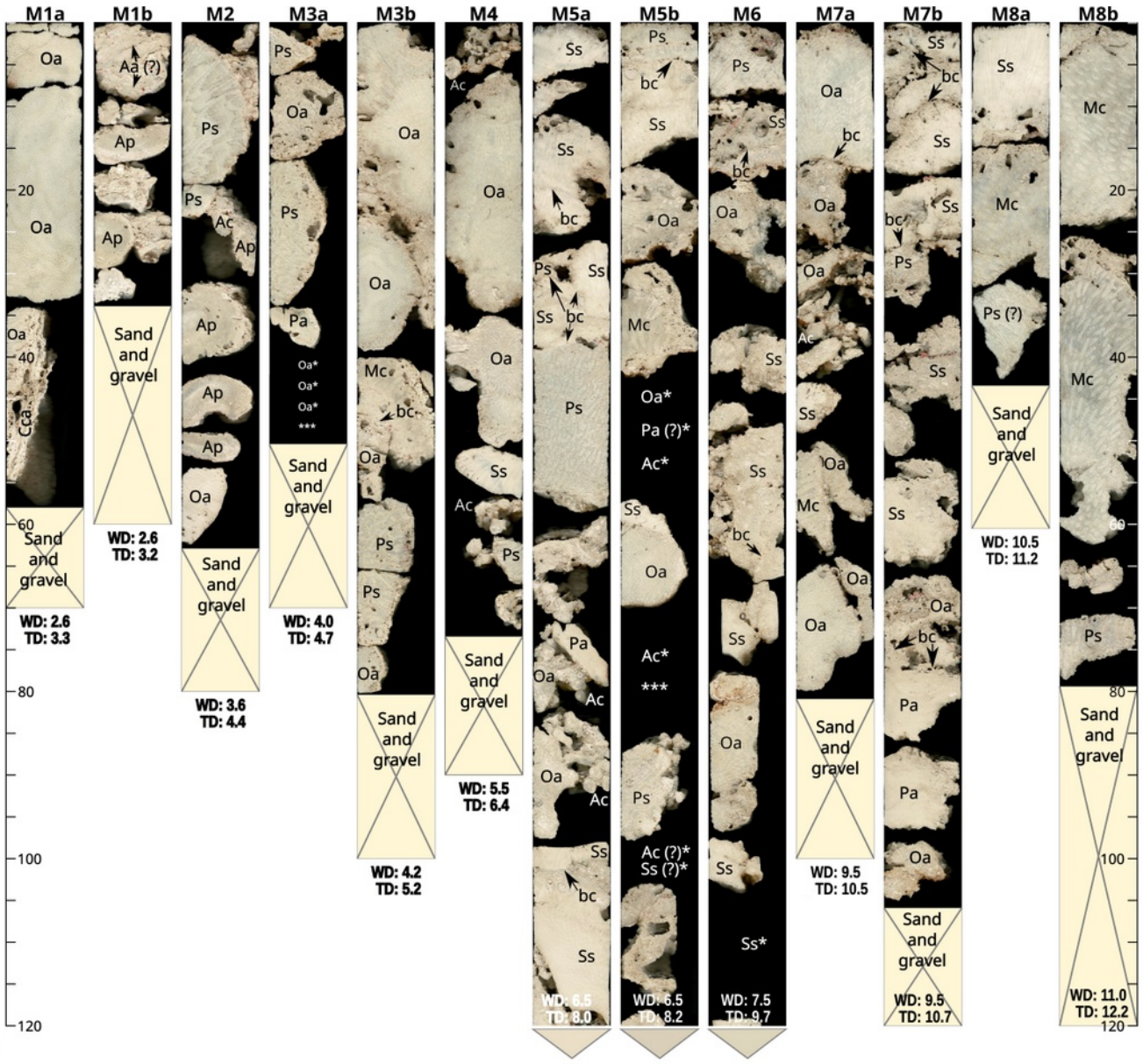

Fig. 17. Core transect over the reef front. Cores M1a to M4 represent the shallow unit, and recovered principally coral rubble with some *in-situ* colonies of *O. annularis* (Oa) in cores M1, M3b and M4, determined mainly by up-oriented corallites; the rubble contains coral fragments of *P. strigosa* (Ps), *A. palmata* (Ap), *O. annularis, A. cervicornis* (Ac), *M. cavernosa* (Mc), *A. agaricites (Aa) and P. astreoides* (Pa). Cores M5 to M8b represent the lower unit and recovered primarily sequences of small/medium *in-situ* colonies of head corals, up to 70 cm large in M8b, the principal frame builder corals were O *.annularis, S. siderea* (Ss), *M. cavernosa, P. astreoides, P. strigosa and A. agaricites*. These cores are characterised by the presence of basal contacts (bc, black arrows), indicating that the coral colonies grew rapidly one on top of each other. Between those colonies, the spaces were infilled by unconsolidated or partially cemented skeletal gravel with a sand matrix (fragments that were not scanned are represented in the core images by an asterisk). All the cores reached an unconsolidated section of sand and gravel, which collapsed into the hole, preventing further penetration. Only the upper 1.2 m of the cores is shown; scale in cm. Water depth at top of hole (WD) and total depth (TD) are shown for each hole at the bottom of each core image.

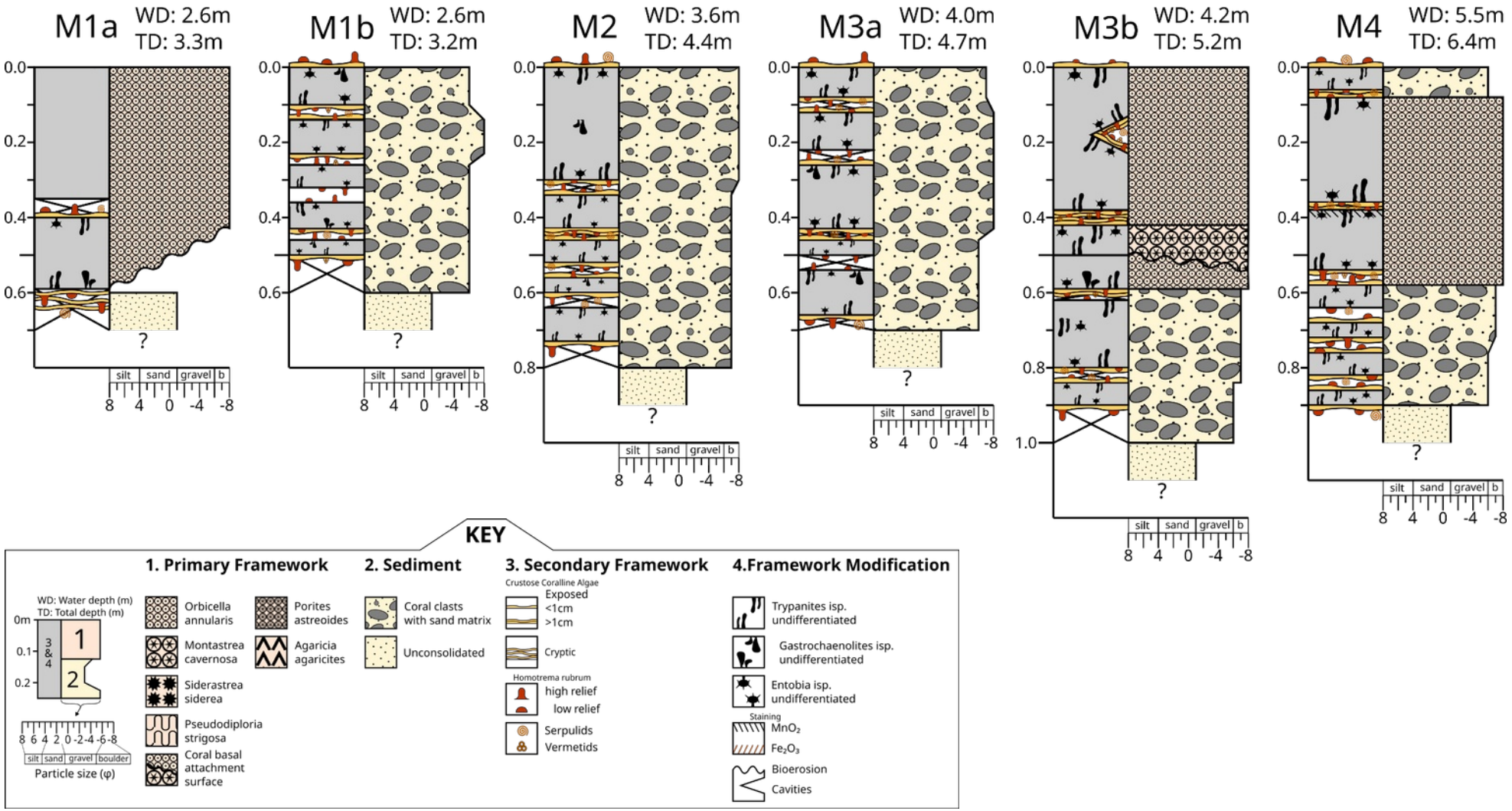

Fig. 18. Upper unit core logs showing primary and secondary framework, framework modification and sediment texture. Upper unit is a sandy coral rubble layer, with gravel to boulder sized clasts, colonised by patches of O. annularis *in- situ* framework. Particle size scale follows Blott and Pye (2012). Vertical scale is in metres below the water/substrate interface. Core name (M#), water depth at top of hole (WD) and total depth (TD) are shown for each hole above each core log.

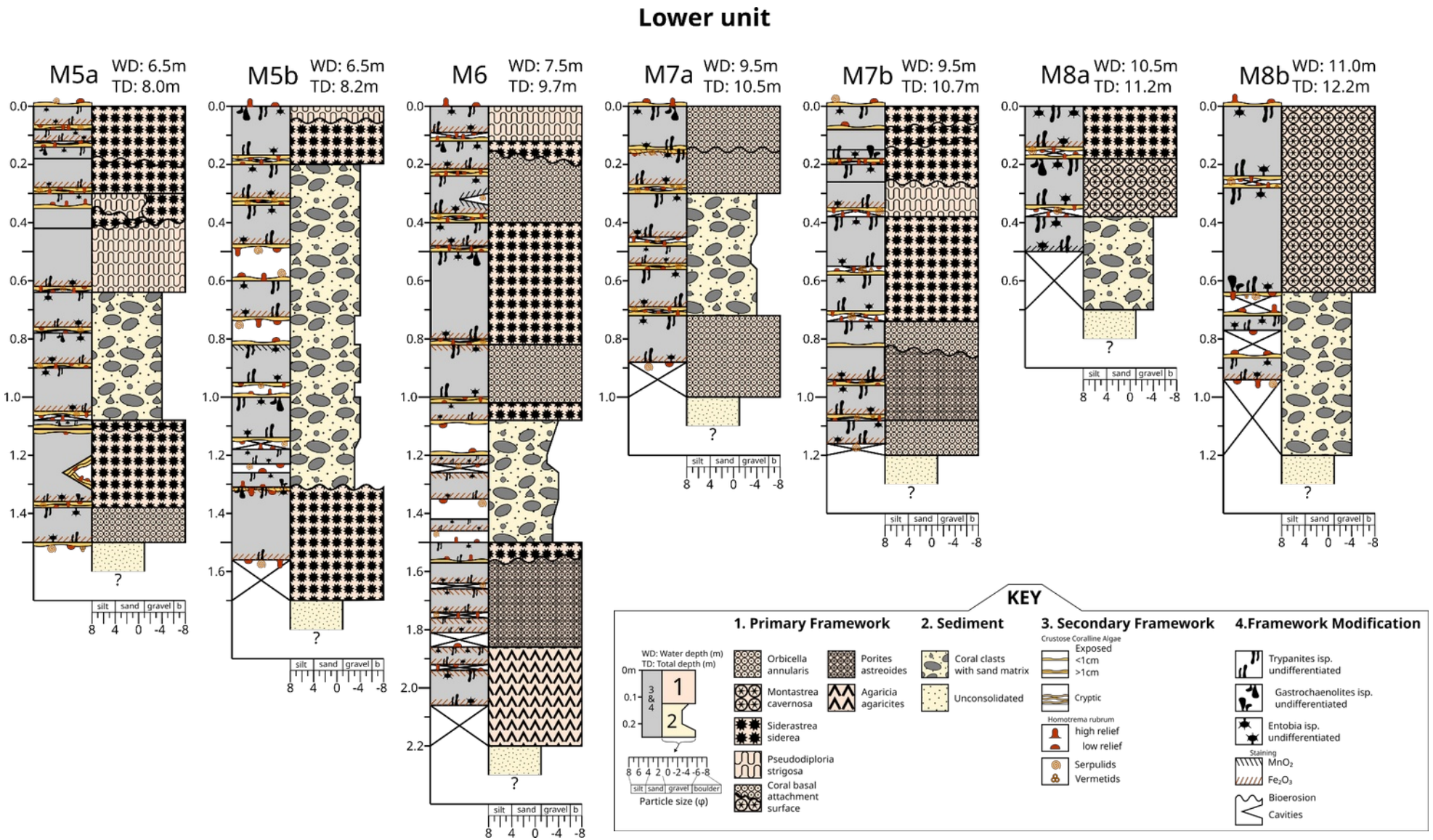

Fig. 19. Lower unit core logs showing primary and secondary framework, framework modification and sediment texture. Lower unit characterised by sequential growth sequence of small/medium in-situ head-corals, principally *O. annularis and S. siderea*, with unconsolidated or partially cemented skeletal gravel with a sand matrix filling the interstices between the framework colonies, mainly *O.annularis, A. cervicornis, P.strigosa, P.astreoides, M, cavernosa, S.siderea*. Particle size scale follows Blott and Pye (2012). Vertical scale is in metres below the water/substrate interface. Core name (M#), water depth at top of hole (WD) and total depth (TD) are shown for each hole above each core log.

Paleoenvironmental interpretation

The processes involved in the development of the two facies from the reef deposit, are interpreted as follow: The lower facies unit began in a low energy environment, favouring the conditions of semi-continuous growth of coral framework consisting of small/medium head-corals, principally *S. siderea* and O*. annularis*. The preservation of basal contacts between the colonies, implies new colonies started growth shortly after the demise of the previous corals and there was little time for colonisation by secondary encrusters, and only a limited bioerosion. Modification of the coral framework is represented by the presence of bioerosional surfaces in almost all the coral colonies, although the modification tends to be light to moderate, with only around 30% of the colonies being removed. In some cores (e.g., M5a), secondary framework such as CCA developed on the undersurface of primary framework, showing that some colonies remained exposed, giving borers and secondary framework sufficient time to develop. Finally, all interstitial cavity space was infilled by skeletal sand and gravel.

The development of the internal structure resembles that proposed by Scoffin (1972) and Scoffin & Garret (1974) for the patch reefs internal structure from Bermuda. Given that these lower facies developed in the reef front, the burial step in the development process is slightly different than in bermuda patch reefs. The sediment infill between colonies is largely unconsolidated but some cores showed partial cementation of skeletal sand and gravel, with some clasts up to ~20 cm in length (M5a and M7a). The composition of the gravel component is heterogeneous, from poorly sorted fragments of all primary framework to branch fragments of *A. cervicornis*, with most presenting moderate amounts of bioerosion and encrustation. This could indicate two scenarios: either the primary framework of branching corals collapsed in place due to structural weakening by bioeroders or high wave energy from occasional storms, removed the fragile branching corals and deposited their detritus in the interstices between head colonies. The poor sorting of coral rubble and its taxonomic heterogeneity, suggests that latter scenario is more likely, and that occasional storms removed fragile corals before they could dominate primary framework development. Lack of removal of this detritus from the reef front, likely caused frequent mortality in the remaining head coral community, thereby preventing the development of large colonies, and instead favouring a frequent turnover of smaller colonies

The upper facies represents a higher-energy facies characterised by the in-place collapse of mainly *A. palmata* and *A. cervicornis* branching colonies, and the deposition of fragments of *O, annularis, P.strigosa*, among others. After the collapse, the large fragments remained exposed to bioerosion and light encrustation and not buried by sediment. The large size of coral clasts contrasts with the lower facies, as do the more abundant head fragments, particularly in the deeper cores of this unit (M3a, M3b and M4). This accumulation of head-coral fragments and the in-place collapse of A. palmata produced a largely detrital unit, which was subsequently colonised by patches of head corals, particularly *O. annularis* in cores M1, M3b and M4. The preservation of these patchy colonies produced large shelter cavities where primary framework is thickly encrusted by secondary framework (such as in core M3b), implying prolonged environmental exposure. These cavities show that the borers probably were able to modify the primary framework to the point of separating the colony into small parts, as reported by Scoffin & Garret (1974). Other in-situ colonies in cores M3b and M4, however, show a similar process

to framework development in the deeper unit, with well-preserved basal contact between colonies, supporting the contention of rapid substrate colonisation over the detritus. Just as the deeper unit, framework development ends with partial marine cementation, with the degree of cementation decreasing as drill depth increases (as in core M3a for example).

A comparison of the coral assemblages between the upper and lower facies and the modern-day benthic assemblages are shown in Figure 20. This shows that in-situ corals in upper facies consist of only two head-coral species, *O. annularis* and *M cavernosa*, whereas the modern benthic assemblage is dominated by *P. astreoides*. This difference is difficult to explain because it is unknown how representative the benthic assemblage is of long-term conditions, especially given the decline in live coral cover over the last 50 years. The lower facies by contrast has a coral assemblage that compares well with the benthic assemblage having all 6 species present in the modern. The proportions do show differences but, in both benthic zones, the proportion of corals that also occur in the lower facies exceeds 50%.

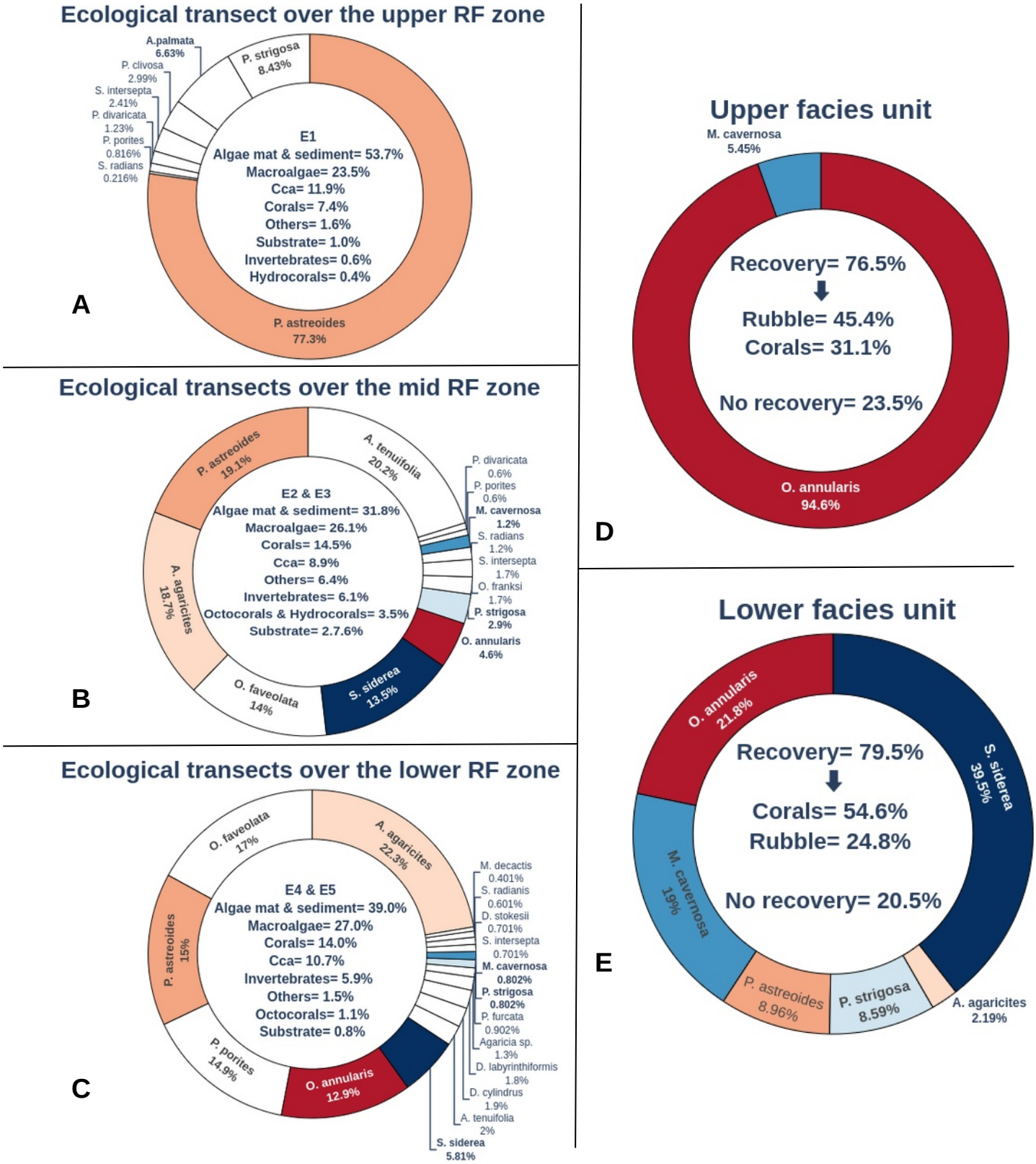

Fig. 20. Comparison between the benthic coral assemblages and facies assemblages in the internal framework. A, B and C show the coral assemblage in each RF zone, derived from ecological transects. D and E show the coral assemblage of the two facies units in the reef deposit. Donut chart colours only represent the hard coral proportions of the internal structure.

Electrical Resistivity Profiles

The form and position of the bedrock beneath the reef structure was delineated from 2 Electrical Resistivity profiles that were generated from each transect using sequential tests of all possible setting options allowed by the software, thereby generating a data inversion that best highlights resistivity variation with depth (Annex B.5 & B.6). The resistivity variation in these profiles allows us to differentiate three units: water column (W), reef deposit (R) and underlying bedrock (B).

Unit W: This uppermost unit, reflects the water column from 8 m below sea level (SL) in the middle of the reef-front where the electrode 1 was placed, to about 10 cm of water in the back-reef flat where electrode 56 was placed. In T1, the water resistivity values are low, ranging from 0.15 to 0.61 Ohm-m (blue to pale green colours in Fig. 15). In the central part, between 60 and 150 on the x axis, some areas show mid values with isolated points of ~1.9 Ohm-m. In T2 water resistivity values are lower than 0.7 Ohm-m (pale green colour in Fig. 15), and correspond to the resistivity characteristics typical of a conductive electrolyte solution with dissolved salts, such as sea water (Singha et al., 2022).

The above average values in T1 likely represent an resistivity artefact generated by an inappropriate electrode contact with the seabed and probably a subsequent movement of electrode cable over the seabed, reflecting the difficulties of working in energetic environments such as shallow reef fronts (Fig. 19). However these artefacts illustrate how singular values can force the software to adjust adjacent values and produce profile distortions. In this case, variation in water resistivity values would indicate a non-homogenous water column, forcing a modification of the resistivity model and producing erroneous profile interpretation (Annex B.4 and B.6). The lower boundary of unit W represents the water-substrate interface, over which the electrodes cable was laid, and corresponds to the bathymetric profile (Fig. 21).

Unit R: Represents the reef-deposit and exhibits mainly low to middle resistivity values that increase with depth to as much as 1 Ohm-m (blue and green colours in Fig. 21). The similarity of values to the water-column unit are the result of not constraining the water resistivity to a single value, as explained before. Core data show the reef deposit is largely unconsolidated and composed of both dense (high resistivity) coral heads and less dense (low resistivity) sand, gravel and open cavities with elevated porosity-permeability characteristics and water saturation. Therefore, the increase in resistivity values with depth (from 0.2 to 1 Ohm-m) likely represent a reduction in water saturation due to either deposit compaction and/or the filling of open cavities with sediment.

By assuming that the lower boundary between the reef deposit and the underlying substrate is marked by resistivity values exceeding 1 Ohm-m, we estimate that the thickness of the reef deposit increases in thickness from 2 ± 1 m in the back-reef flat (x axis = 275), to 10 ± 2m in the middle of the front reef (x axis =0). Both transects were laid close to the drill-core transect, allowing us to interpolate their locations and superimpose them on the resistivity profiles (Fig. 12 and 21).

Unit B: The underlying bedrock unit is distinguishable from the overlying reef deposit (unit R) based on the abrupt increase in resistivity values exceeding 1 Ohm-m (yellow to orange colours). This change is interpreted to represent a jump in substrate density which corresponds to a decrease in porosity-permeability characteristics typical of a fully consolidated bedrock. The position of the bedrock surface beneath the reef structure at T1 was estimated to be 17 ± 2 m below SL in the middle of the front reef (x axis =0), forming a gentle slope to 2 ± 1 m below SL in the back reef flat (x axis = 275) for T1 (Fig. 21A). Similarly at T2, the back-reef position is the same, sloping to 18 ± 2 m below SL in the middle of the front reef (x axis =0) (Fig. 21B).

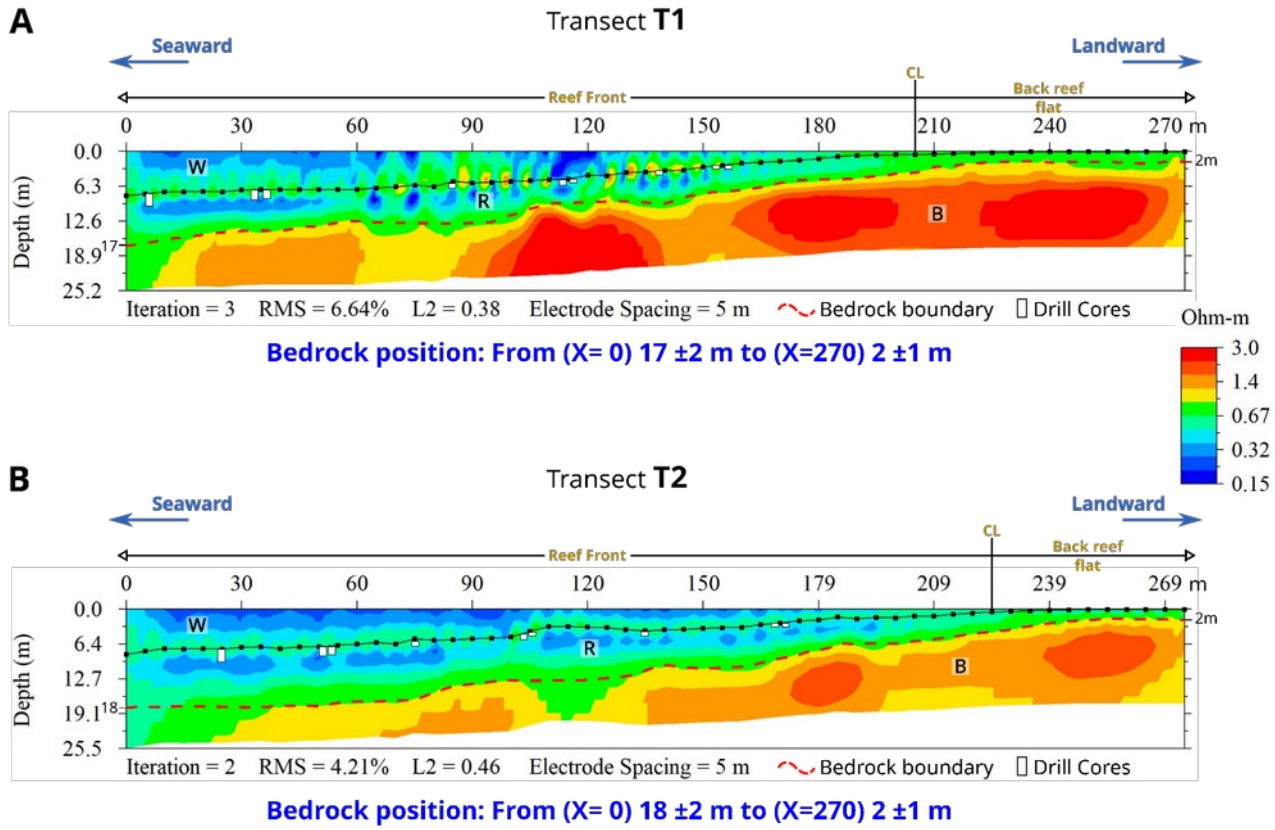

Fig. 21. Electrical Resistivity Profiles. A) Profile reconstruction for T1 . B) Profile reconstruction for T2. Both show in the upper x axis the cable length in m, from x=0 m (starting point) at the middle of the reef structure, to x=275m (end point) in the back reef flat. Over it, the reef zonation is displayed, as well as its orientation. The electrodes cable is displayed as a black line with 56 square dots, which represent the 56 passive electrodes cable; the drilled cores from the drill transect are projected onto the resistivity profiles as white rectangles. The dotted red line represents the boundary between the reef deposit and underlying bedrock.The z axis shows the depth in m, starting at 0 m at SL. CL= Crest line; B= unit B (bedrock, high resistivity unit ≥ 1 Ohm-m); R= unit R (reef deposit, 0.2 Ohm-m < mid/low resistivity unit ≤ 1 Ohm-m); and W= unit W (Water column, low resistivity unit < 0.7 Ohm-m.).

Resistivity variation between transects (most clear for bedrock): On account of the minimum differences in the position of the shown boundaries between the two transects and to the better performance in the field of T2, this one was taken as the representative depth for the full reef structure (Annex. B.5 and B.6).

DISCUSSION

Our data show that reef deposit at Mahahual consists of a seaward-thickening wedge of largely unconsolidated mix of coral framework (55%) and sedimentary detritus (45%), covering a gently sloping (5.9 %) bedrock terrace with low rugosity from 2 ± 1 m in the back-reef to a 18 ± 2 m in the lower RF. The reef deposit therefore has a minimum thickness of 2 (±1) m, and a maximum of 10 (±2) m. Drill cores only recovered the upper 2.2 m of this deposit but show two facies: an upper sediment unit (2-6 m below SL), of skeletal sand and gravel with lenses of *O. annularis* framework; and a lower framework unit (6-13 m below SL), of small/medium *in-situ* head-corals, dominated by *S. siderea* and *O. annularis* (Fig. 22).

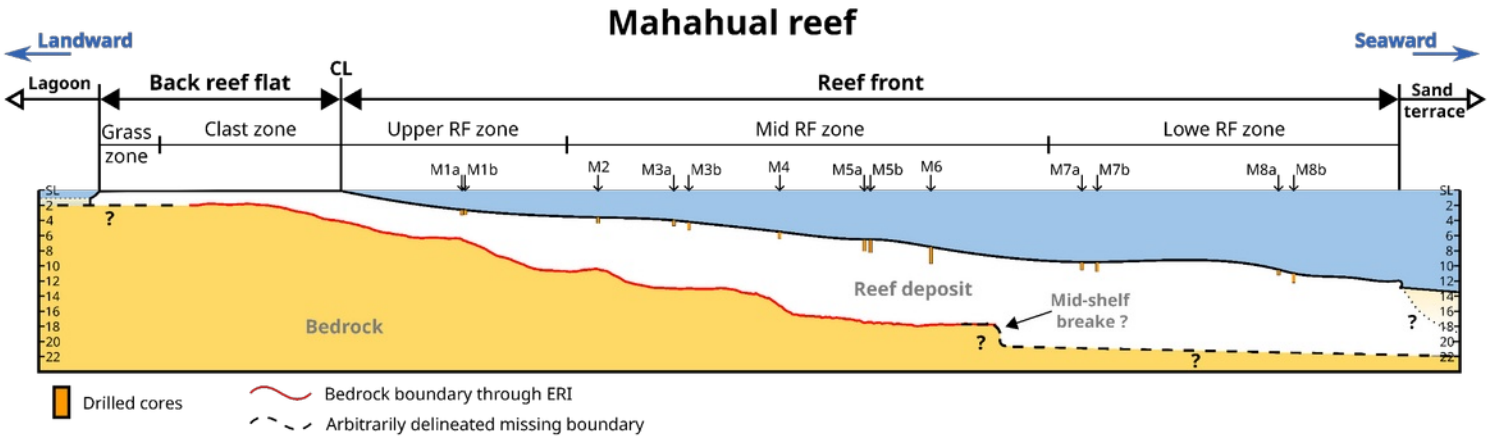

Fig. 22. Mahahual fringing reef profile. The fringing reef deposit is shown as a white polygon; within it, 13 orange rectangles represent the drilled-cores. Reliable bedrock form and position is marked with a continuous red line, where this boundary is unknown, dashed black line with question marks replaced it. The location of the Mid-shelf brake is also inferred, from the ERI and the resulting depth, which resemble its location from other reefs closed by. The geomorphic zonation is displayed above the profile, as well as its orientation. The form and depth of the sand units in the lagoon and sand terrace are unknown, and the boundaries with the reef deposit are arbitrarily represented with a dotted black line with question marks.

These two facies were likely the result of two main energy environments, a low energy environment, where the lower facies could develop its head-coral framework and occasionally high energy storms removed the more fragile branching colonies, and distributed this detritus over the reef front filling interstices and abrading live colonies. More of this detritus was transported upslope closer to the reef crest, completely smothering live coral cover. These processes produced the difference between framework facies, with the lower facies having less rubble and a high turn-over of head corals, and the upper facies having more rubble colonised by head corals (Fig. 20D & E). This pruning and redistribution of fragile corals by storms is supported to a certain extent by the modern benthic ecology of the reef-front zones. Although these ecological assemblages contain the majority of hard corals within the facies, many of their principal components are fragile branching corals such as *A. tenifolia, A. palmata* and *P. porites*, which are either absent or form only a minor proportion of the framework facies (Fig. 20A to C).

As such the effects of storms have generated a taphonomic bias in the framework facies which prevents a strictly comparative reconstruction of the paleoecology of the reef at Mahahual.

In terms of reef development, our data has significant uncertainty stemming from the absence of longer drill cores and an inability to fully sample the reef deposit and underlying substrate. The maximum drill depth of 2.2 m (Core M6) had a recovery of 80% but was unable to penetrate deeper due to the presence of sand at the base of the core. This was primarily a technical limitation due to the lack of a water pump in the drilling system. Nevertheless, we are confident that the facies data are representative given that parallel transects provide a test of lateral continuity.

Although the thickness of the reef deposit also remains to be confirmed by drilling data, we consider that the inversion model depth threshold value of 1 Ohm-m (Annex B.6), is accurate and therefore that the electric resistivity profiles represent a reliable interpretation of Mahahual reef structure. This is supported by values reported in other ERI studies. For example, Cardenas et al. (2010) ran a DD cable-tow survey of a 2 m deep “reef flat” around Santiago Island, Philippines, and reported a threshold resistivity value between 0.5 –1.0 Ohm-m to delimit the “reef flat” from seawater (0.1 to ~0.2 Ohm-m). Similarly, Befus et al. (2014) ran a DD cable-tow survey of the shallow Lagoon of Rarotonga, Cook Islands, reporting thresholds values for seawater from ≤ 0.1 to 0.5 Ohm-m, for “consolidated reef deposits” and porous volcanic rocks from 0.5 to 1.5 Ohm-m and for limestone and volcanics from 1.5 to ≥ 5 Ohm-m. Finally in a recent DD boat-tow survey of reefal deposits around Santiago Island, Philippines, Cantarero et al. (2019) identified three resistivity units: a unit with values greater than 3 Ohm-m, interpreted as a layer of sediments saturated with phreatic pore water; a unit varying from 1 to 3 Ohm-m, interpreted as being influenced by both phreatic and marine signatures; and a unit with values less than 1 Ohm-m, interpreted as sediments saturated with seawater or “saline” groundwater. The interpretations were made assuming that bulk resistivity is largely controlled by pore-fluid conductivity and that lithologic influences are minimal.

Even though these previous studies have shown that the influx of phreatic groundwater can increase resistivity and produce heterogeneous subsurface profiles, our ERI profiles do not show this effect. This is because the influx of groundwater occurs either at aquitards (such as the sediment-bedrock interface) or through bedrock fractures or other conduits (Kambesis & Coke IV, 2013). Either of these cases would generate high-resistivity zones that would exceed the typical carbonate sediment saturated with seawater values (Cardenas et al., 2010). Our data show a gradual increase of resistivity values with depth, which is interpreted as an increase in the degree of compaction or lithification in the reef structure (less porosity, therefore less saline porewater saturation) with depth, and with an abrupt transition into fully-consolidated carbonate bedrock where the resistivity values surpass the value of 1 Ohm-m.

The facies, thickness, and substrate depth we have documented from the Mahahual fringing reef show significant differences to other Caribbean fringing reefs, such as Punta Maroma fringing reef in the northeast Yucatan Peninsula. The main geomorphic difference is the wide

sub-horizontal intertidal flat landward of the CL, and the deeper, lower gradient RF zone at Mahahual, which contrasts with the steeper crest-type reef and shallower RF zone at Punta Maroma. The internal structure and development are also markedly different: at Mahahual internal structure is driven mainly by a low-energy environment which favours the growth of head-corals as primary coral framework and, due to the protection against the direct impact of hurricanes provided by Chinchorro Bank, only minor storm waves can reach the reef which results in the pruning of fragile corals and the generation of sedimentary detritus that infills the interstices between the coral framework. By contrast at Punta Maroma the internal structure is composed by a layer of *A. palmata* coral clasts that were destroyed and accumulated by large hurricane waves. The only occurrence of A. palmata at Mahahual occurs in the upper facies and in subordinate quantities, implying that it was not a major framework builder.

These significant differences allow some preliminary conclusions to be drawn regarding environmental controls on Caribbean reef development. Our findings from Mahahual suggest that reefs protected from the full force of hurricane waves have different geomorphologies, are composed of different facies, and have developed more extensive vertical sequences than reefs exposed to hurricanes. These differences seem to stem from the accumulation of coral detritus generated from both in-place collapse or destruction of fragile branching corals during storms. Their lack of removal, means that these deposits control both the character of facies development, and increase the rate of vertical accretion, producing reefs with a distinctive flat-type geomorphology. This conclusion has recently received support from a survey of geomorphic reef types across the Greater Caribbean, which has shown that reefs in hurricane impacted areas have a crest-type morphology, typical of that found at Punta Maroma, whereas those in hurricane-free areas have a flat-type morphology, typical of that documented here for Mahahual (Blanchon et al., 2022).

Further work

To support and confirm these findings however requires further investigation of both reef types, including:

1. Analysis of the morphology of the underlying substrate to address claims that reef geomorphology is influenced by the form of the underlying substrate. In the case of Mahahual, although we have shown that the reef is an independent structure, we do not know if the form of the underlying bedrock has influenced reef development and need to run additional ERI profiles parallel to the crestline.

2. Further drilling to reach and confirm the position of the bedrock beneath the reef structure, as well as characterise facies development through time. This will also help complete the resistivity model to estimate the accuracy of the inversion model.

3. Perform radiometric dating of the core samples to determine the chronological reef structure in order to determine its development through time.

4. High-resolution benthic images are also required to create a precise and accurate bathymetric map of the zone, in order to obtain an optimal characterization of the reef geomorphology.

5. Historical analysis of benthic cover is needed in order to further test the relation between the facies and benthic assemblages in the reef front.

6. Hindcast of oceanographic wave data to quantify the shelter provided by Chinchorro bank of the incoming wave energy and the energy shadow that it provides against hurricane impact.

SUMMARY AND CONCLUSIONS

1. The fringing reef at Mahahual has two main geomorphic zones either side of the crestline:

    a) a landward back-reef flat, characterised by a wide sub-horizontal intertidal flat, which can be subdivided into two subzones: a proximal clast subzone and a distal seagrass subzone.

    b) a seaward reef-front unit, which is subdivided into three subzones: an upper RF subzone, characterised by coral stumps and rubble; a middle RF subzone, characterised by spurs and grooves; and a lower RF subzone, characterised by spurs with intervening sand patches.

2. The shallow internal structure of Mahahual fringing reef (up to 2.2 m beneath its surface), is composed by two facies units:

    a) a lower framework facies unit (from 6 to 13 m below SL), made up by small/medium in-situ head-corals, dominated by *S. siderea* and *O. annulari*s, with interstitial rubble. This developed in a low-energy environment, where semi-continuous in-situ head-coral growth was occasionally interrupted by storms which destroyed fragile corals and redistributed their gravel detritus infilling interstices and low areas. The failure of these storms to completely remove this detritus, likely inhibited the development of large colonies and stemmed from the shelter provided by Chinchorro Bank.

    b) an upper sediment facies unit (from 2 to 6 m below SL), made up by skeletal sand and coral gravel with lenses of *O. annularis* framework. This developed in a higher energy zone, with storms triggering the collapse of fragile branching colonies (mainly *A. palmata* and *A. cervicornis)* and transport and deposition of dislodged head corals. This detrital layer was subsequently colonised by head coral lenses.

3. The electrical signature of subsurface profiles over the Mahahual reef, highlights three features:

    a) the reef deposit, with low to middle resistivity values that increase with depth, up to 1 Ohm-m, resulting from porosity reduction due to either compaction and/or the filling of internal cavities with sediment.

    b) the underlying bedrock, with high resistivity values, exceeding 1 Ohm-m, which represent a further abrupt decrease in porosity-permeability characteristics of a fully consolidated unit.

c) The boundary between the reef deposit and bedrock forms a gentle slope from to 2 ± 1 m below SL in the back reef flat, to 18 ± 2 m below SL in the middle of the reef front.

4. These subsurface data from the Mahahual fringing reef contrast with subsurface data from other Caribbean fringing reefs, and support the hypothesis that reefs protected from the full force of hurricane waves develop a distinct geomorphology, distinct facies, and more extensive vertical sequences than reefs exposed to hurricanes. Furthermore, the absence of frameworks dominated by *A. palmata*, at Mahahual questions its perceived ecological role as the main structural engineer of Caribbean reefs.

REFERENCES

Adey,W. H. (1978). Coral reef morphogenesis: a multidimensional model. Science 202, 831–837. doi:10.1126/science.202.4370.831

Advanced Geosciences, I. (2009). Instruction Manual for EarthImager 2D Version 2.4.0. Resistivity and IP Inversion Software.

Aguilar-Perera, A. (1994). Preliminary observations on the spawning aggregation of Nassau grouper, *Epinephelus striatus*, at Mahahual, Quintana Roo, Mexico. Proc. Gulf Carib. Fish. Inst. 43: 112-122.

Aguilar-Perera, A. and Aguilar-Dávila, W. (1996). A spawning aggregation of Nassau grouper *Epinephelus striatus* (Pisces: Serranidae) in the Mexican Caribbean. Environmental Biology of Fishes 45: 351-361.

Argüelles-Jiménez, J., Alva-Basurto, J.C., Pérez-España, H., Zetina-Rejón, M.J., Arias- González, J.E. (2020). The measurement of ecosystem development of Mexican Caribbean reefs through topological indices. Ecol. Indic. 110, 1-11. https://doi.org/10.1016/j.ecolind.2019.105866.

Argüelles-Jiménez, J., Rodríguez-Zaragoza, F.A., González-Gándara, C., Alva-Basurto, J.C., Arias-González, J.E., Hernández-Landa, R., Aguilar-Perera, A., Okolodkov, Y.B., Gutiérrez-Velázquez, A.L., Zetina-Rejón, M.J., Ulanowicz, R., Pérez-España, H. (2021). Functional developmental states of the Greater Caribbean coral reefs. Ecological Indicators 121, 1-11. https://doi.org/10.1016/j.ecolind.2020.107170

Arias-González, J.E. (1998). Trophic models of protected and unprotected coral reef ecosystems in the South of the Mexican Caribbean. Journal of Fish Biology 53(A), 236–255.

Befus, K. M., Cardenas, M. B., Tait, D.R., and Erler, D. V. (2014). Geoelectrical signals of geologic and hydrologic processes in a fringing reef lagoon setting. Journal of Hydrology, 517, 508-520. https://doi.org/10.1016/j.jhydrol.2014.05.070

Blanchon, P., and Perry, C. T. (2004). Taphonomic differentiation of Acropora palmata facies in cores from Campeche Bank Reefs, Gulf of Mexico. Sedimentology 51 (1}, 53–76. https://doi.org/10.1046/j.1365-3091.2003.00610.x

Blanchon, P., Granados-Corea, M., Abbey, E., Braga, J. C., Braithwaite, C., Kennedy, D.M., Spencer, T., Webster, J. M., and Woodroffe, C. D. (2014). Postglacial Fringing-Reef to Barrier-Reef conversion on Tahiti links Darwin's reef types. Sci Rep, 4 (4997), 1-9. https://doi.org/10.1038/srep04997

Blanchon, P., Jones, B., and Kalbfleisch, W. (1997). Anatomy of a fringing reef around Grand Cayman; storm rubble, not coral framework. Journal of Sedimentary Research. 67 (1), 1–16. https://doi.org/10.1306/D42684D7-2B26-11D7-8648000102C1865D

Blanchon, P., Medina-Valmaseda, A.E., Islas-Domínguez, E., Guerra-Castro, E., Blakeway, D., Garza-Pérez, J.R., Jordan-Garza, A.G., Mariño-Tapia, I., Zapata Ramírez, P.A. (2022). Linear breakwater reefs of the Greater Caribbean: Classification, Distribution & Morphology. PLoS One 17(11): e0270053. https://doi.org/10.1371/journal.pone.0270053

Blanchon, P., Richards, S., Bernal, J.P., Cerdeira-Estrada, S., Ibarra, M.S., Corona- Martínez, L. and Martell-Dubois, R. (2017). Retrograde Accretion of a Caribbean Fringing Reef Controlled by Hurricanes and Sea-level Rise. Front. Earth Sci. 5:78. https://doi.org/10.3389/feart.2017.00078

Blott, S.J. and Pye, K. (2012). Particle size scales and classification of sediment types based on particle size distributions: Review and recommended procedures. Sedimentology, 59 (7), 2071-2096. https://doi.org/10.1111/j.1365-3091.2012.01335.x

Cantarero, D. L. M., Blanco, A., Cardenas, M. B., Nadaoka, K., and Siringan, F. P. (2019). Offshore submarine groundwater discharge at a coral reef front controlled by faults. Geochemistry, Geophysics, Geosystems, 20 (7), 3170– 3185. https://doi.org/10.1029/2019GC008310

Cardenas, M. B., Zamora, P. B., Siringan, F. P., Lapus, M. R., Rodolfo, R. S., Jacinto, G. S., San Diego-McGlone, M. L., Villanoy, C. L., Cabrera, O., and Senal, M. I. (2010). Linking regional sources and pathways for submarine groundwater discharge at a reef by electrical resistivity tomography, ^{222}Rn, and salinity measurements. Geophysical Research Letters, 37(L16401), 1-6.

https://doi.org/10.1029/2010GL044066
CONABIO, (2018a). Cobertura Bentónica del Ecosistema Arrecifal Coralino del Caribe Mexicano: Cabo Catoche - Xcalak. 2018. Sistema Nacional de Información sobre Biodiversidad (SNIB). Portal de Geoinformación 2022. México. Available on: http://www.conabio.gob.mx/informacion/gis/
CONABIO, (2018b). Batimetría de los Ecosistema Marinos del Caribe Mexicano: Cabo Catoche - Xcalak. 2018. Sistema Nacional de Información sobre Biodiversidad (SNIB). Portal de Geoinformación 2022. Mexico. Available on: http://www.conabio.gob.mx/informacion/gis/
Daly, R. A. (1915). The glacial-control theory of coral reefs. Proc. Am. Acad. Arts Sci. 51, 157–251. doi:10.2307/20025572
Darwin, C. R. (1842). The Structure and Distribution of Coral Reefs. Being the First Part of the Geology of the Voyage of the Beagle, Under the Command of Capt. Fitzroy, RN, During the Years 1832 to 1836. (Smith Elder, London).
Dey, A. and Morrison, H. (1979). `Resistivity modelling for arbitrarily shaped two-dimensional structures', Geophysical Prospecting 27(1), 106-136. https://doi.org/10.1111/j.1365-2478.1979.tb00961.x
Gómez-Nicolás, M.P. (2014). Análisis de la conectividad entre cenotes a través de Tomografía de Resistividad Eléctrica y Teoría de Redes. Tesis de Maestría. Centro De Investigación y de Estudios Avanzados del Instituto Politécnico Nacional.
Goreau, T.F. (1959). The ecology of Jamaican coral reefs: I. Species composition and zonation. Ecology, 40(1), 67-90. https://doi.org/10.2307/1929924
Holcombe, H. T. and Jiracek, G. R. (1984). Three-dimensional terrain corrections in resistivity surveys. Geophysics, 49. 439-452. https://doi.org/10.1190/1.1441679
Islas-Domínguez, E.G. (2020). Espesor y Geometría de los sedimentos de la zona del arrecife posterior en el arrecife de franja de Punta Maroma. Tesis de Licenciatura. Facultad de Ingeniería. Universidad Nacional Autónoma de México. http://132.248.9.195/ptd2020/febrero/0800364/Index.html
Jordán-Dahlgren, E. and Rodriguez-Martinez, R.E. (2003). The Atlantic coral reefs of Mexico. In: Cortés, J. (Editor). Latin American Coral Reefs. Elsevier 131-158.
Kambesis, P. N., and Coke IV, J. G. (2013). Overview of the Controls on Eogenetic Cave and Karst Development in Quintana Roo, Mexico. Lace, M. J. and Mylroie, M.J. (eds.). Coastal Karst Landforms (pp. 347 - 373), Coastal Research Library 5, Springer Science+Business Media Dordrecht. DOI: 10.1007/978-94-007-5016-6 16
Loke, M.H. (2001). `Tutorial: 2-d and 3-d electrical imaging surveys', Copyright (1996-2012).
Lowrie, W. (1997). Fundamentals of Geophysics. (Second edition). UK. Cambridge University Press.
Lugo, A. E., Rogers, C. S., and Nixon, S. W. (2000). Hurricanes, coral reefs and rainforests: resistance, ruin and recovery in the Caribbean. Ambio: : A Journal of the Human Environment, 29 (2), 106–114. https://doi.org/10.1579/0044-7447-29.2.106
Macintyre, I.G. and Glynn, P.W. (1976). Evolution of a modern Caribbean fringing reef, Galeta Point, Panama. AAPG Bull., 60, 1054–1072.
Macintyre, I. G., Burke, R. B., and Stuckenrath, R. (1977). Thickest recorded Holocene reef section, Isla Pérez core hole, Alacran reef, Mexico. Geology, 5 (12), 749-754. doi:10.1130/0091-7613(1977)5<749:TRHRSI>2.0.CO;2
Macintyre, I.G., Glynn, P.W., and Steneck, R.S. (2001) . A classic Caribbean algal ridge, Holandes Cays, Panama: an algal coated storm deposit. Coral Reefs 20: 95-105. https://doi.org/10.1007/s003380000135
Martıínez-Rendis, A., Acosta-González, G., Hernández-Stefanoni, J.L., and Arias-González, J.E. (2016). Quantifying the reefscape transformation of a coastal Caribbean coral reef during a phase shift and the associated coastal landscape change. Marine Ecology, 37(3), 697–710.

https://doi.org/10.1111/maec.12334
Mesolella, K.J. (1967) Zonation of uplifted Pleistocene coral reefs on Barbados, West Indies. Science, 156 (3775), 638–640. DOI: 10.1126/science.156.3775.638
Mesolella, K.J., Matthews, R. K., Broecker, W.S. and Thurber, D.L. (1969). The Astronomical Theory of Climatic Change: Barbados Data. The Journal of Geology, 77(3), 250-274. http://www.jstor.org/stable/30063932
Meyer, D., Bries, J., Greenstein, B., and Debrot, A. (2003). Preservation of in situ reef framework in regions of low hurricane frequency: pleistocene of Curaçao and Bonaire, southern Caribbean. Lethaia 36, 273–285. https://doi.org/10.1080/00241160310004675
Neumann, A. C., and Macintyre, I. (1985). Reef response to sea level rise: keep–up, catch–up or give–up. Proceedings of the Fifth International Coral Reef Congress, Tahiti, Vol. 3, 105–110.
Núñez-Lara, E., Arias-González, J.E., Legendre, P. (2005). Spatial patterns of Yucatan reef fish communities: Testing, models using a multi-scale survey design. Journal of Experimental Marine Biology and Ecology, 324, 157–169. https://doi.org/10.1016/j.jembe.2005.04.011
Reynolds, J.M. (1997). An Introduction to Applied and Environmental Geophysics. England. John Wiley & Sons Ltd.
Rodríguez-Zaragoza, F.A. and Arias-González, J.E. (2015). Coral biodiversity and bio-construction in the northern sector of the mesoamerican reef system. Front. Mar. Sci. 2(13), 1-16. https://doi.org/10.3389/fmars.2015.00013
Ruíz-Zárate, M. A., Hernández-Landa, R., González-Salas, C., Núñez-Lara, E., and Arias-González, J. E. (2003). Condition of coral reef ecosystems in central-southern Quintana Roo (Part 1: stony corals and algae). In Lang, J. C. (ed.), Status of Coral Reefs in the western Atlantic: Results of Initial Surveys, Atlantic and Gulf Rapid Reef Assessment (AGRRA) Program. Atoll Research Bulletin 496,318–337. https://doi.org/10.5479/si.00775630.496-18.318
Scoffin, T. P. (1972). Fossilization of Bermuda patch reefs. Science, 178(4067), 1280-1282.
Scoffin, T. P., and Garrett, P. (1974). Processes in the formation and preservation of internal structure in Bermuda patch reefs. Proceedings of the Second International Coral Reef Symposium, Vol. 2: 429-448.
Singha, K., Johnson, T.C., Day-Lewis, F.D., and Slater, L. D. (2022). Electrical Imaging for Hydrogeology. The Groundwater Project, Guelph, Ontario, Canada.
Shinn, E. (1963). Spur and Groove formation on the Florida reef tract. Journal of Sedimentary Petrology, 33(2), 291-303. https://doi.org/10.1306/74D70E34-2B21-11D7-8648000102C1865D
Telford, W. M. y Sheriff, R. E. (1990). Applied geophysics, Vol. 1, Cambridge University press.

ANNEX A

1. Reef Core Analysis Protocol

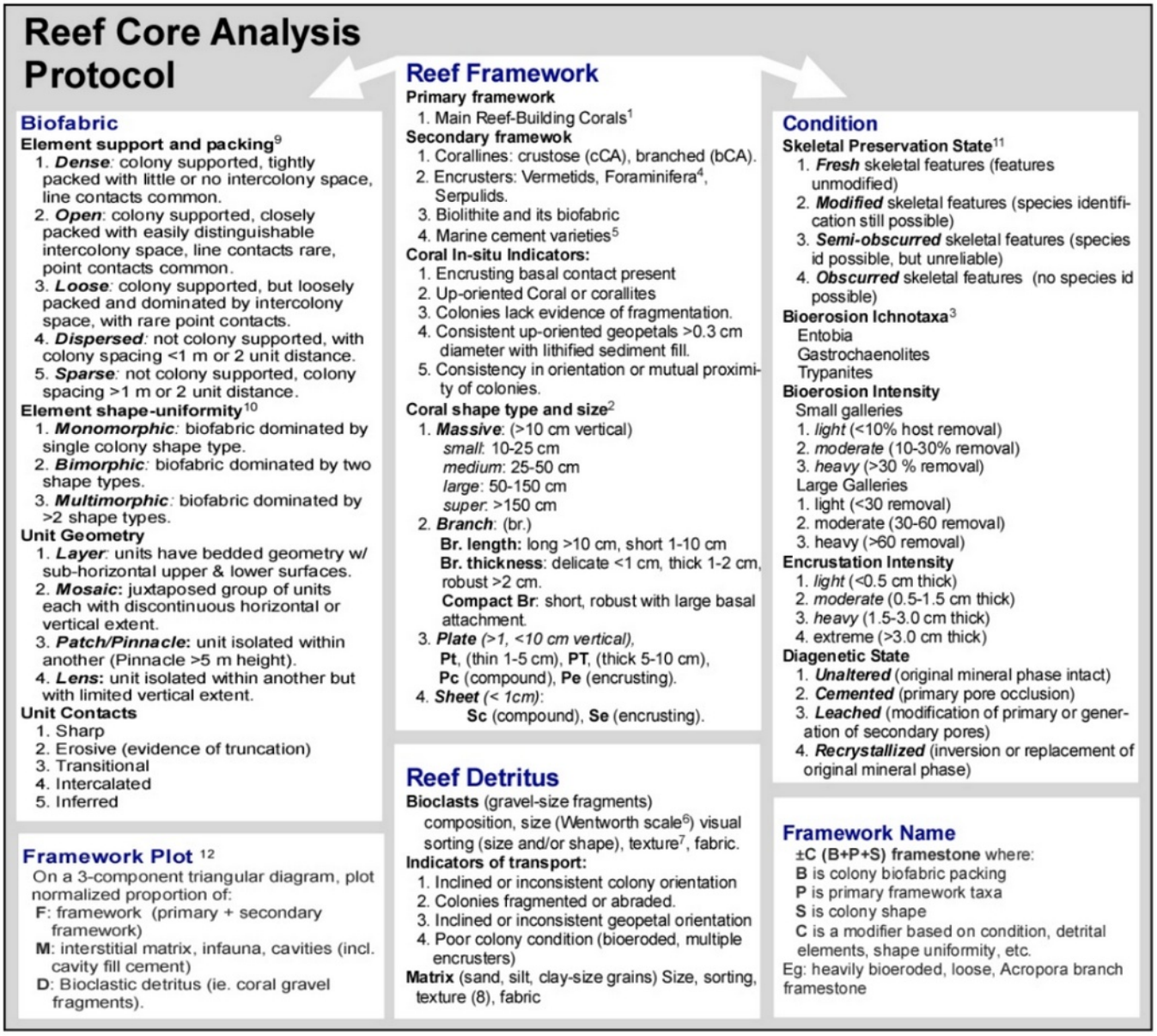

Fig. A.1. Core description protocol used for reefal sedimentary units (taken from Blanchon et al., 2014).

2. Scanned cores and composition logs

2.1. M1a

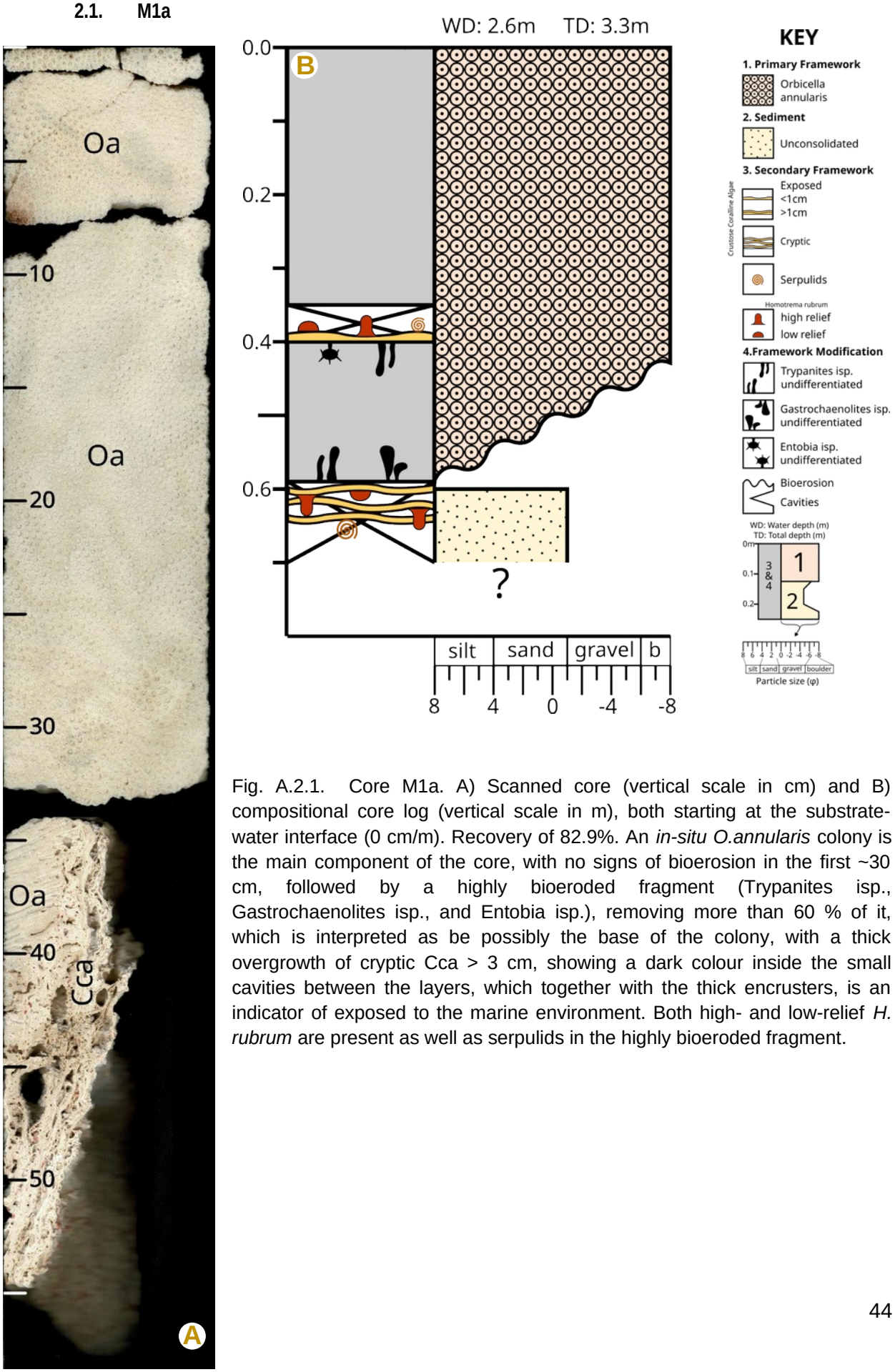

Fig. A.2.1. Core M1a. A) Scanned core (vertical scale in cm) and B) compositional core log (vertical scale in m), both starting at the substrate-water interface (0 cm/m). Recovery of 82.9%. An *in-situ O.annularis* colony is the main component of the core, with no signs of bioerosion in the first ~30 cm, followed by a highly bioeroded fragment (Trypanites isp., Gastrochaenolites isp., and Entobia isp.), removing more than 60 % of it, which is interpreted as be possibly the base of the colony, with a thick overgrowth of cryptic Cca > 3 cm, showing a dark colour inside the small cavities between the layers, which together with the thick encrusters, is an indicator of exposed to the marine environment. Both high- and low-relief *H. rubrum* are present as well as serpulids in the highly bioeroded fragment.

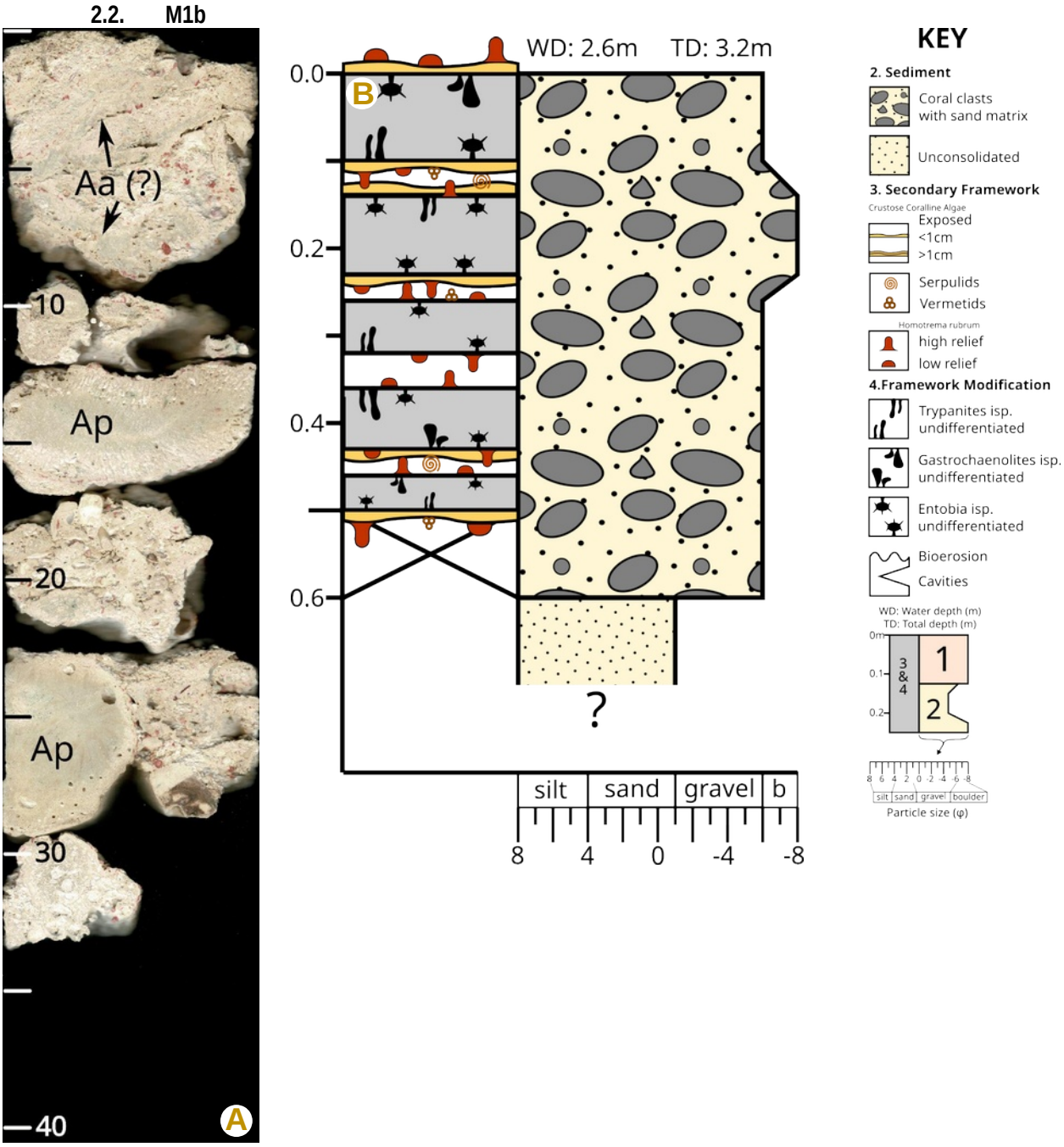

Fig. A.2.2. Core M1b. A) Scanned core (vertical scale in cm) and B) compositional core log (vertical scale in m), both starting at the substrate-water interface (0 cm/m) Recovery of 58.3 %. A moderate bioeroded coral rubble sequence is shown, with interstitial sand matrix, the smaller fragments are cemented. The identifiable larger clasts are mainly *A. palmata* clasts (Ap) and probably a fragment of *A. agaricites* at the top. The bioerosion consists of Trypanites isp., Gastrochaenolites isp., and Entobia isp. Encrustations of thin Cca (< 1cm) are present, as well as serpulids, vermetids and both high and low relief H. rubrum. This clastic assemblage is the reflection of a deposit in a high energy zone.

2.3. M2

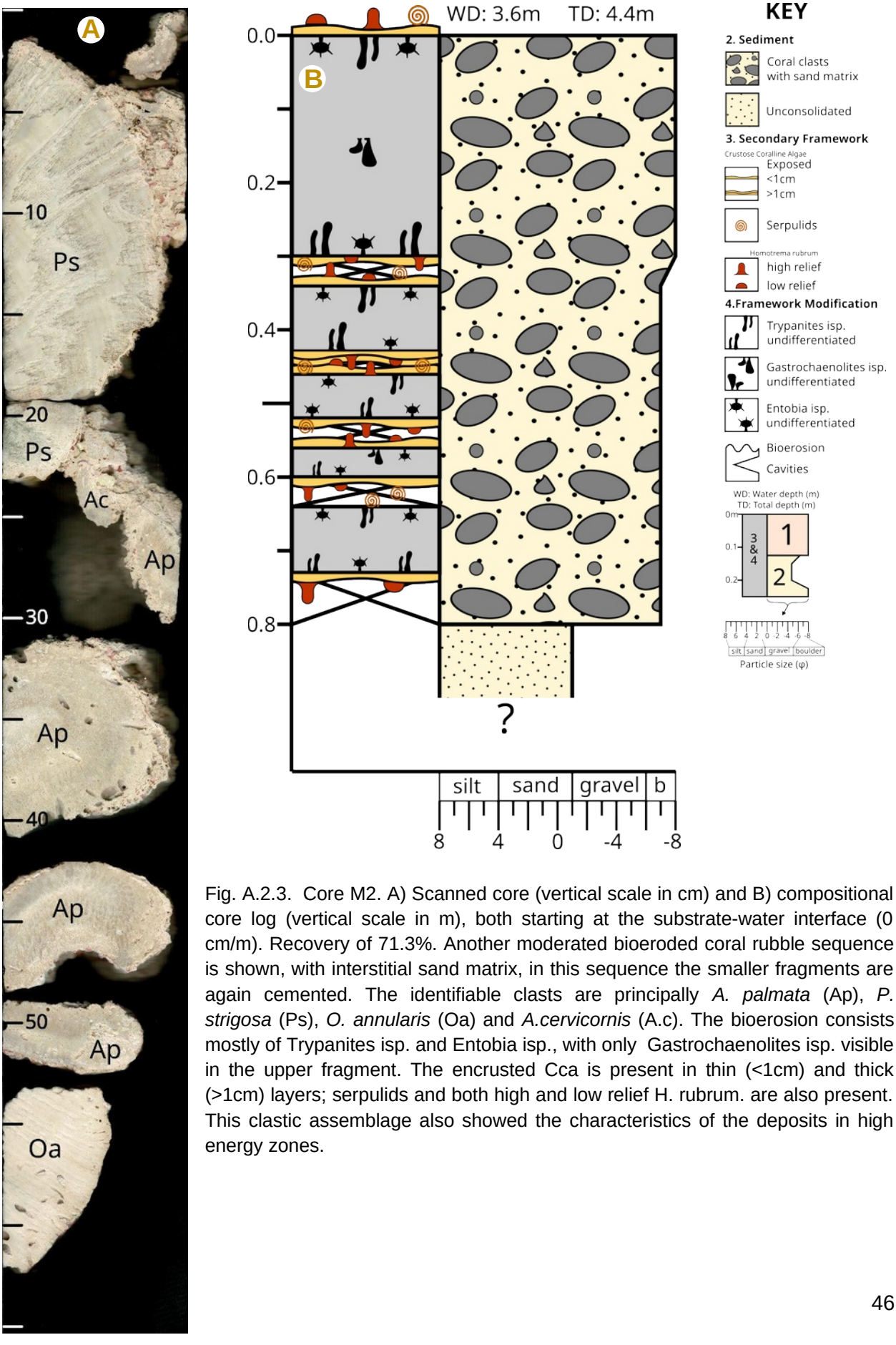

Fig. A.2.3. Core M2. A) Scanned core (vertical scale in cm) and B) compositional core log (vertical scale in m), both starting at the substrate-water interface (0 cm/m). Recovery of 71.3%. Another moderated bioeroded coral rubble sequence is shown, with interstitial sand matrix, in this sequence the smaller fragments are again cemented. The identifiable clasts are principally *A. palmata* (Ap), *P. strigosa* (Ps), *O. annularis* (Oa) and *A.cervicornis* (A.c). The bioerosion consists mostly of Trypanites isp. and Entobia isp., with only Gastrochaenolites isp. visible in the upper fragment. The encrusted Cca is present in thin (<1cm) and thick (>1cm) layers; serpulids and both high and low relief H. rubrum. are also present. This clastic assemblage also showed the characteristics of the deposits in high energy zones.

2.4. M3a

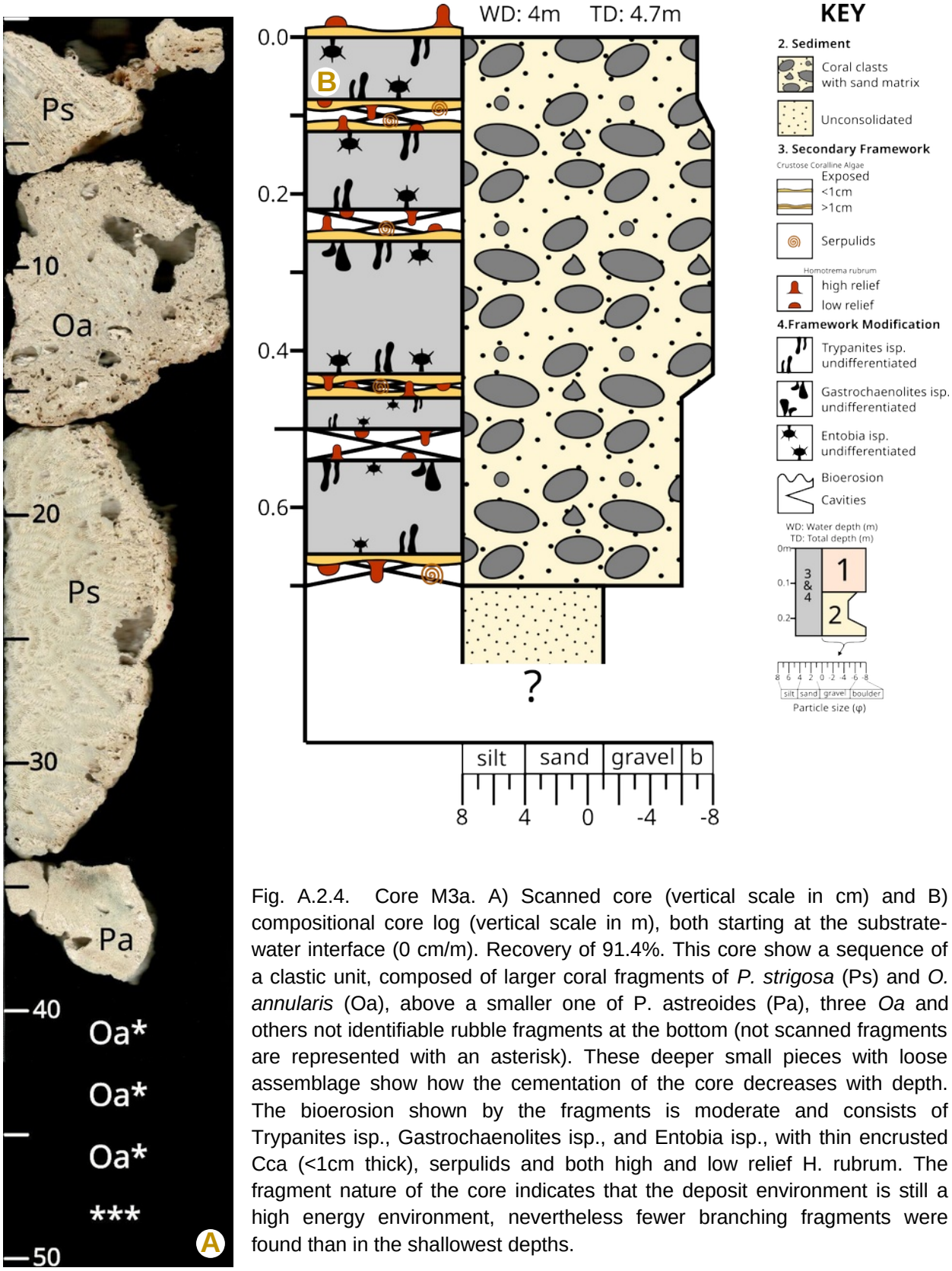

Fig. A.2.4. Core M3a. A) Scanned core (vertical scale in cm) and B) compositional core log (vertical scale in m), both starting at the substrate-water interface (0 cm/m). Recovery of 91.4%. This core show a sequence of a clastic unit, composed of larger coral fragments of *P. strigosa* (Ps) and *O. annularis* (Oa), above a smaller one of P. astreoides (Pa), three *Oa* and others not identifiable rubble fragments at the bottom (not scanned fragments are represented with an asterisk). These deeper small pieces with loose assemblage show how the cementation of the core decreases with depth. The bioerosion shown by the fragments is moderate and consists of Trypanites isp., Gastrochaenolites isp., and Entobia isp., with thin encrusted Cca (<1cm thick), serpulids and both high and low relief H. rubrum. The fragment nature of the core indicates that the deposit environment is still a high energy environment, nevertheless fewer branching fragments were found than in the shallowest depths.

2.5. M3b

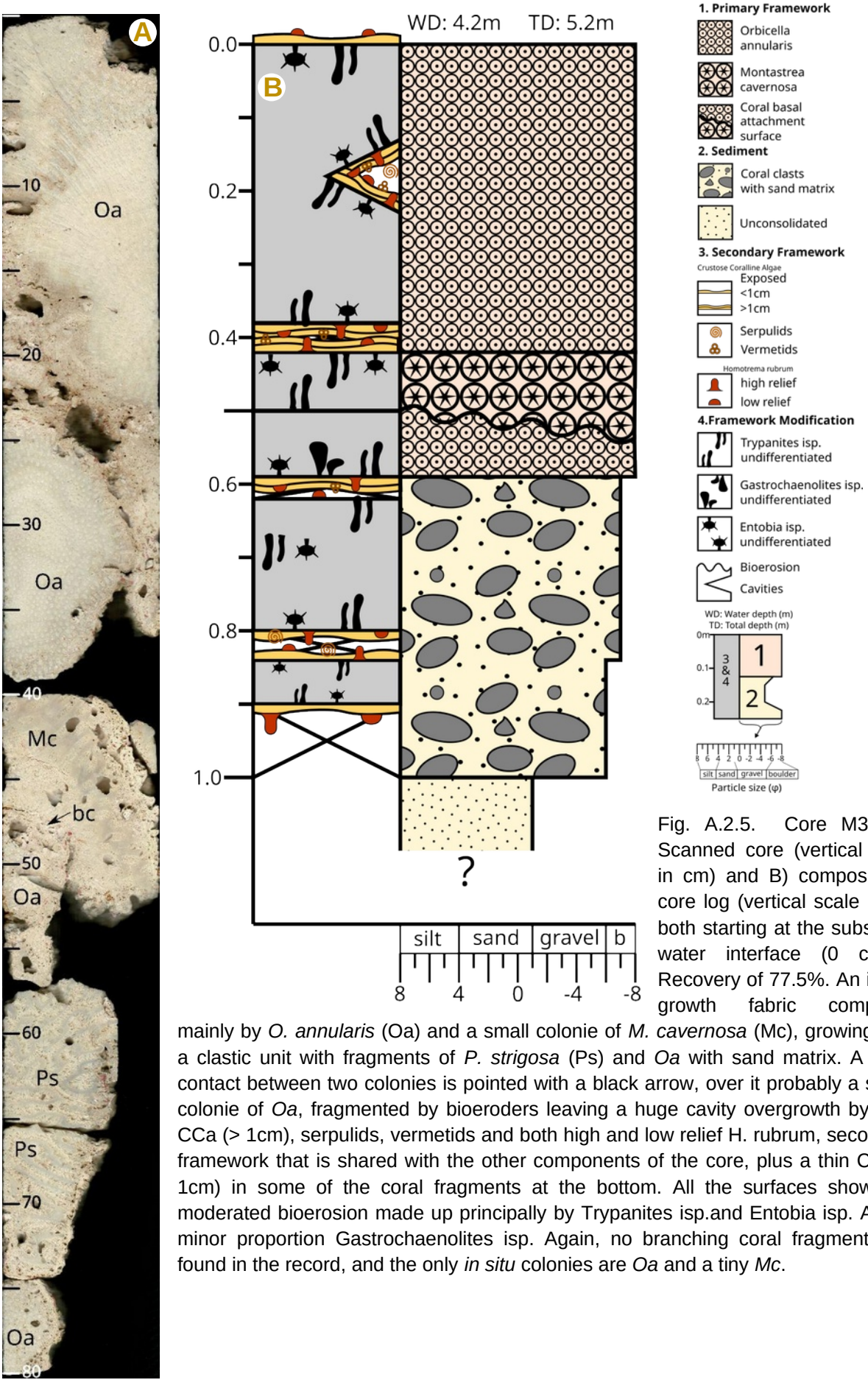

Fig. A.2.5. Core M3b. A) Scanned core (vertical scale in cm) and B) compositional core log (vertical scale in m), both starting at the substrate-water interface (0 cm/m). Recovery of 77.5%. An in situ growth fabric composed mainly by *O. annularis* (Oa) and a small colonie of *M. cavernosa* (Mc), growing over a clastic unit with fragments of *P. strigosa* (Ps) and *Oa* with sand matrix. A basal contact between two colonies is pointed with a black arrow, over it probably a single colonie of *Oa*, fragmented by bioeroders leaving a huge cavity overgrowth by thick CCa (> 1cm), serpulids, vermetids and both high and low relief H. rubrum, secondary framework that is shared with the other components of the core, plus a thin Cca (< 1cm) in some of the coral fragments at the bottom. All the surfaces showed a moderated bioerosion made up principally by Trypanites isp.and Entobia isp. And in minor proportion Gastrochaenolites isp. Again, no branching coral fragments are found in the record, and the only *in situ* colonies are *Oa* and a tiny *Mc*.

2.6. M4

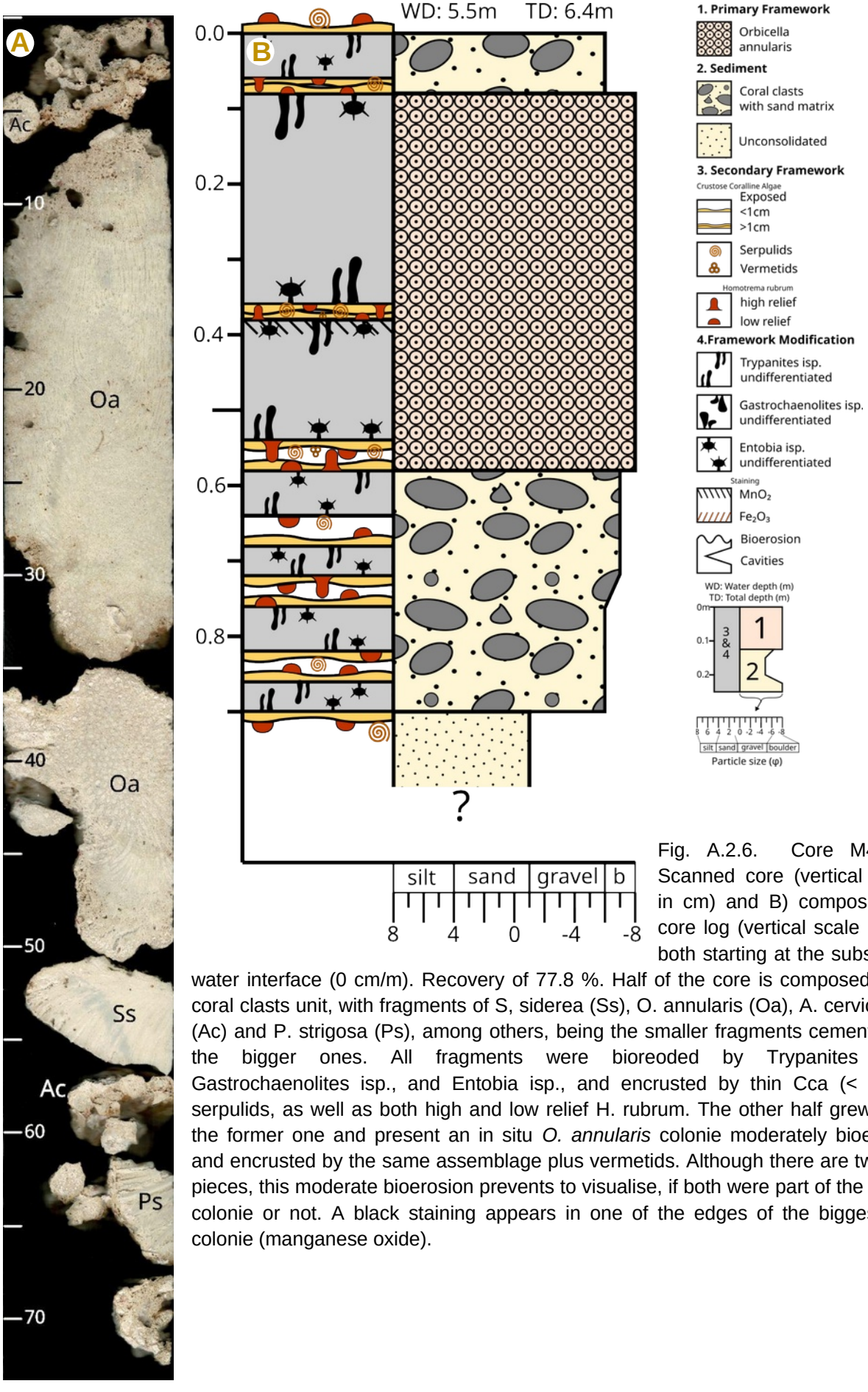

Fig. A.2.6. Core M4. A) Scanned core (vertical scale in cm) and B) compositional core log (vertical scale in m), both starting at the substrate-water interface (0 cm/m). Recovery of 77.8 %. Half of the core is composed by a coral clasts unit, with fragments of S, siderea (Ss), O. annularis (Oa), A. cervicornis (Ac) and P. strigosa (Ps), among others, being the smaller fragments cemented to the bigger ones. All fragments were bioreoded by Trypanites isp., Gastrochaenolites isp., and Entobia isp., and encrusted by thin Cca (< 1cm), serpulids, as well as both high and low relief H. rubrum. The other half grew over the former one and present an in situ *O. annularis* colonie moderately bioeroder and encrusted by the same assemblage plus vermetids. Although there are two Oa pieces, this moderate bioerosion prevents to visualise, if both were part of the same colonie or not. A black staining appears in one of the edges of the biggest Oa colonie (manganese oxide).

2.7. M5a

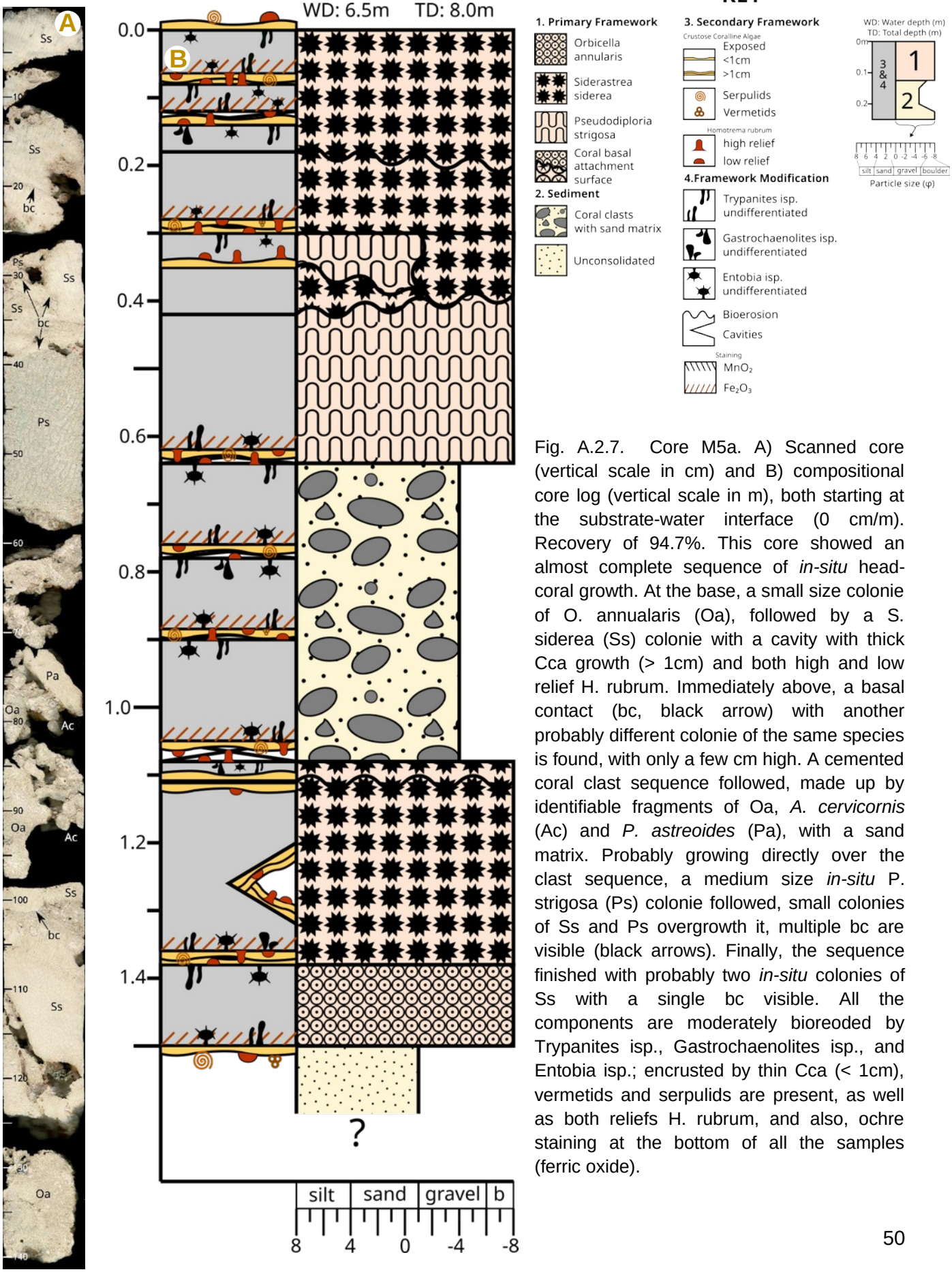

Fig. A.2.7. Core M5a. A) Scanned core (vertical scale in cm) and B) compositional core log (vertical scale in m), both starting at the substrate-water interface (0 cm/m). Recovery of 94.7%. This core showed an almost complete sequence of *in-situ* head-coral growth. At the base, a small size colonie of O. annualaris (Oa), followed by a S. siderea (Ss) colonie with a cavity with thick Cca growth (> 1cm) and both high and low relief H. rubrum. Immediately above, a basal contact (bc, black arrow) with another probably different colonie of the same species is found, with only a few cm high. A cemented coral clast sequence followed, made up by identifiable fragments of Oa, *A. cervicornis* (Ac) and *P. astreoides* (Pa), with a sand matrix. Probably growing directly over the clast sequence, a medium size *in-situ* P. strigosa (Ps) colonie followed, small colonies of Ss and Ps overgrowth it, multiple bc are visible (black arrows). Finally, the sequence finished with probably two *in-situ* colonies of Ss with a single bc visible. All the components are moderately bioreoded by Trypanites isp., Gastrochaenolites isp., and Entobia isp.; encrusted by thin Cca (< 1cm), vermetids and serpulids are present, as well as both reliefs H. rubrum, and also, ochre staining at the bottom of all the samples (ferric oxide).

2.8. M5b

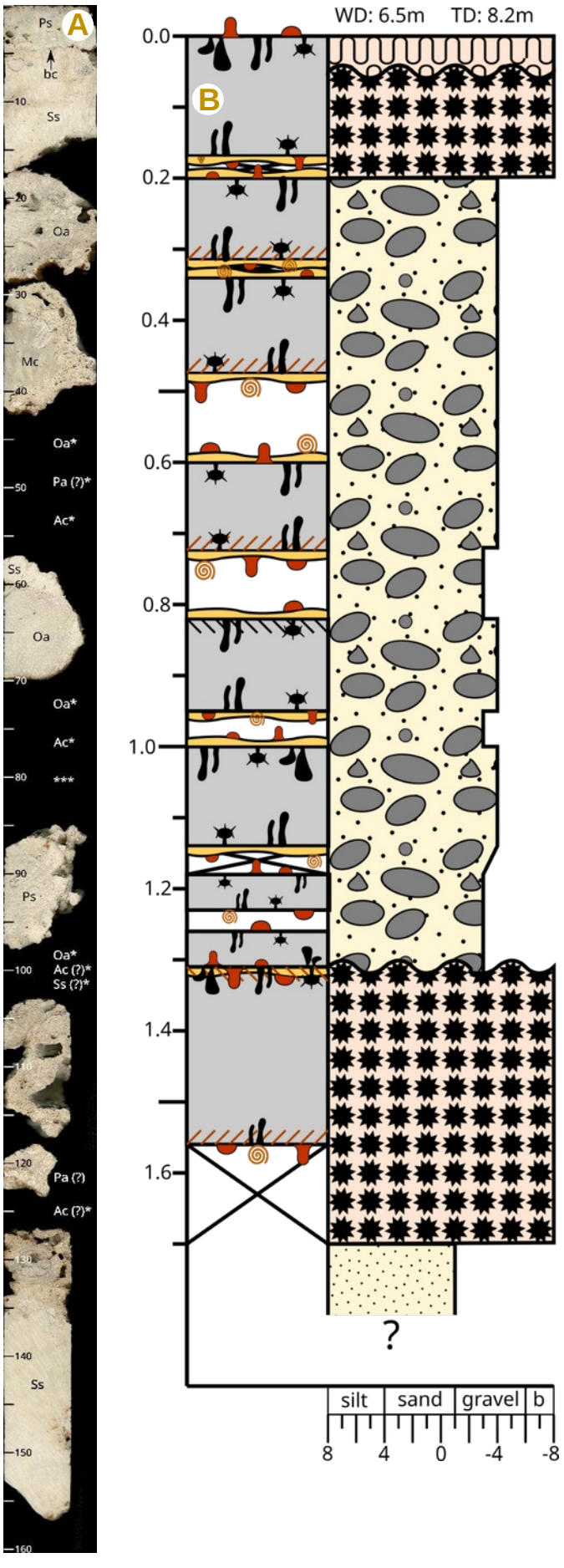

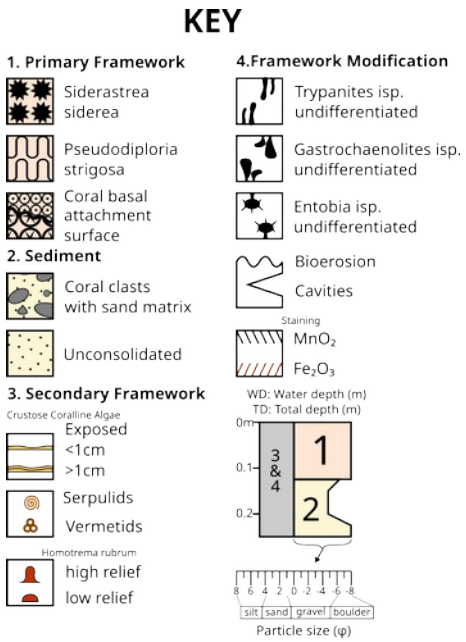

Fig. A.2.8. Core M5b. A) Scanned core (vertical scale in cm) and B) compositional core log (vertical scale in m), both starting at the substrate-water interface (0 cm/m). Recovery of 85.3%. An *in-situ* colonie of *S. siderea* (Ss) at the bottom with minimal bioerosion, with exception of its top where a heavy bioerosion is visible, capped by diverse calcareous fragments, a big oyster is identifiable. Followed by an unconsolidated clast sequence, mainly made up by fragments of O. annularis (Oa), *A. cervicornis* (Ac), *P. astreoides* (Pa) and Ss. Until this depth in the core (~1 m), the diamete0r was 7.62 cm, meanwhile the recovered core above was 10.16 in diameter, due to a change of bit to facilitate the recovery with depth. The thicker recovery continued with unconsolidated fragments until around 15 cm before the substrate/water interface, fragments of Oa, Ac, *M. cavernosa* (Mc), *P. strigosa* (Ps), were identifiable. An *in-situ* Ss colonie with a tiny Ps growth over it (basal contact, black arrow) topped the sequence. This basal contact seems to be the only one between two in situ colonies; there are other colonies overgrowing other colonies, but due to the corallites not in an up position, those were taken as fragments. The majority of the sequence presented a moderated bioerosion made by Trypanites isp., Gastrochaenolites isp., and Entobia isp. encrusted by thin Cca (< 1cm), vermetids, serpulids, as well as both reliefs of H. rubrum. Also, an ochre staining at the bottom of most samples (ferric oxide) and only one black staining at the top of an Oa fragment are present (manganese oxide).

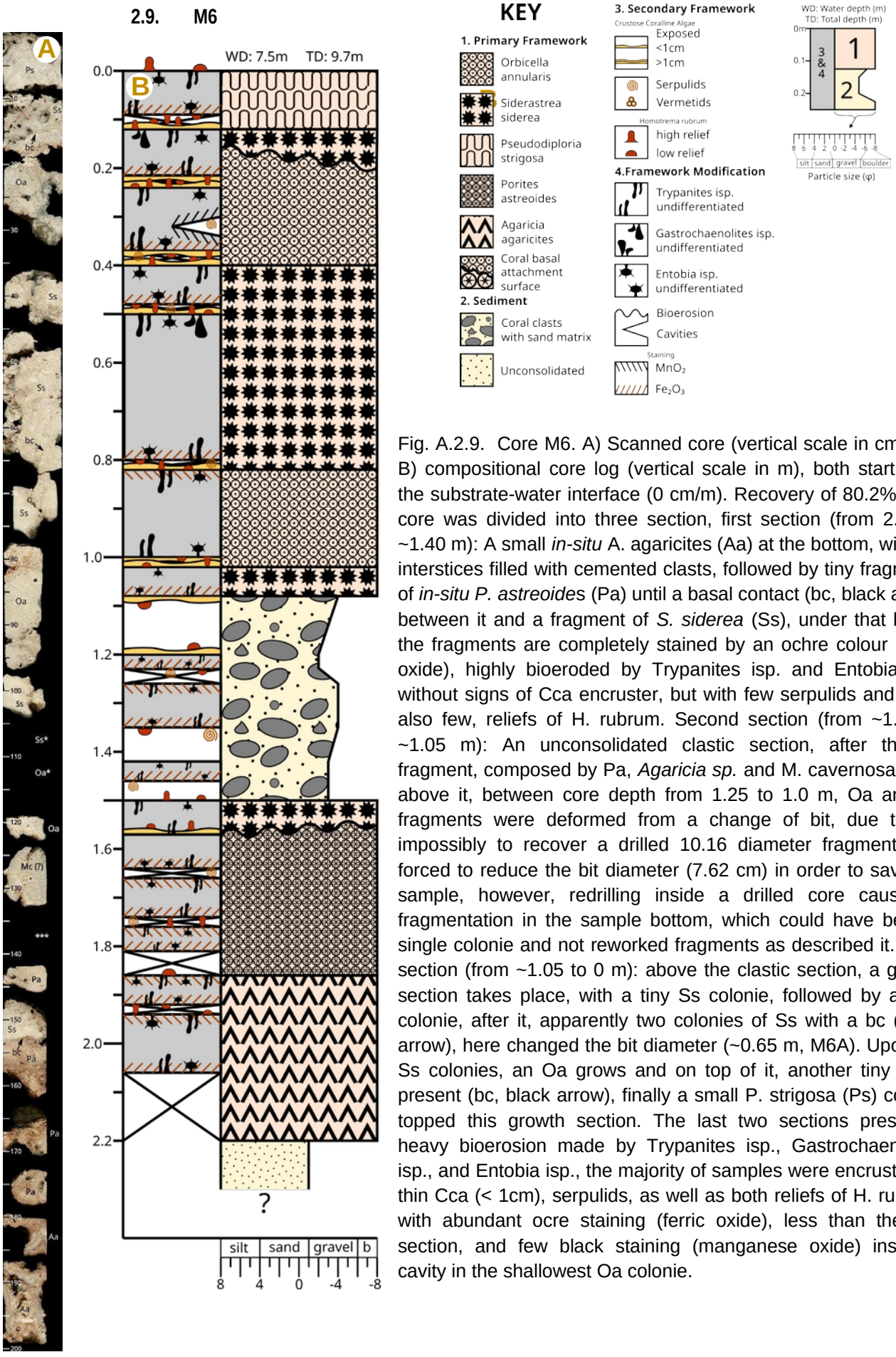

Fig. A.2.9. Core M6. A) Scanned core (vertical scale in cm) and B) compositional core log (vertical scale in m), both starting at the substrate-water interface (0 cm/m). Recovery of 80.2%. This core was divided into three section, first section (from 2.20 to ~1.40 m): A small *in-situ* A. agaricites (Aa) at the bottom, with the interstices filled with cemented clasts, followed by tiny fragments of *in-situ P. astreoide*s (Pa) until a basal contact (bc, black arrow) between it and a fragment of *S. siderea* (Ss), under that bc, all the fragments are completely stained by an ochre colour (ferric oxide), highly bioeroded by Trypanites isp. and Entobia isp., without signs of Cca encruster, but with few serpulids and both, also few, reliefs of H. rubrum. Second section (from ~1.40 to ~1.05 m): An unconsolidated clastic section, after the Ss fragment, composed by Pa, *Agaricia sp.* and M. cavernosa (Mc), above it, between core depth from 1.25 to 1.0 m, Oa and Ss fragments were deformed from a change of bit, due to the impossibly to recover a drilled 10.16 diameter fragment, that forced to reduce the bit diameter (7.62 cm) in order to save the sample, however, redrilling inside a drilled core caused a fragmentation in the sample bottom, which could have been a single colonie and not reworked fragments as described it. Third section (from ~1.05 to 0 m): above the clastic section, a growth section takes place, with a tiny Ss colonie, followed by an Oa colonie, after it, apparently two colonies of Ss with a bc (black arrow), here changed the bit diameter (~0.65 m, M6A). Upon the Ss colonies, an Oa grows and on top of it, another tiny Ss is present (bc, black arrow), finally a small P. strigosa (Ps) colonie topped this growth section. The last two sections presented heavy bioerosion made by Trypanites isp., Gastrochaenolites isp., and Entobia isp., the majority of samples were encrusted by thin Cca (< 1cm), serpulids, as well as both reliefs of H. rubrum, with abundant ocre staining (ferric oxide), less than the first section, and few black staining (manganese oxide) inside a cavity in the shallowest Oa colonie.

2.10. M7a

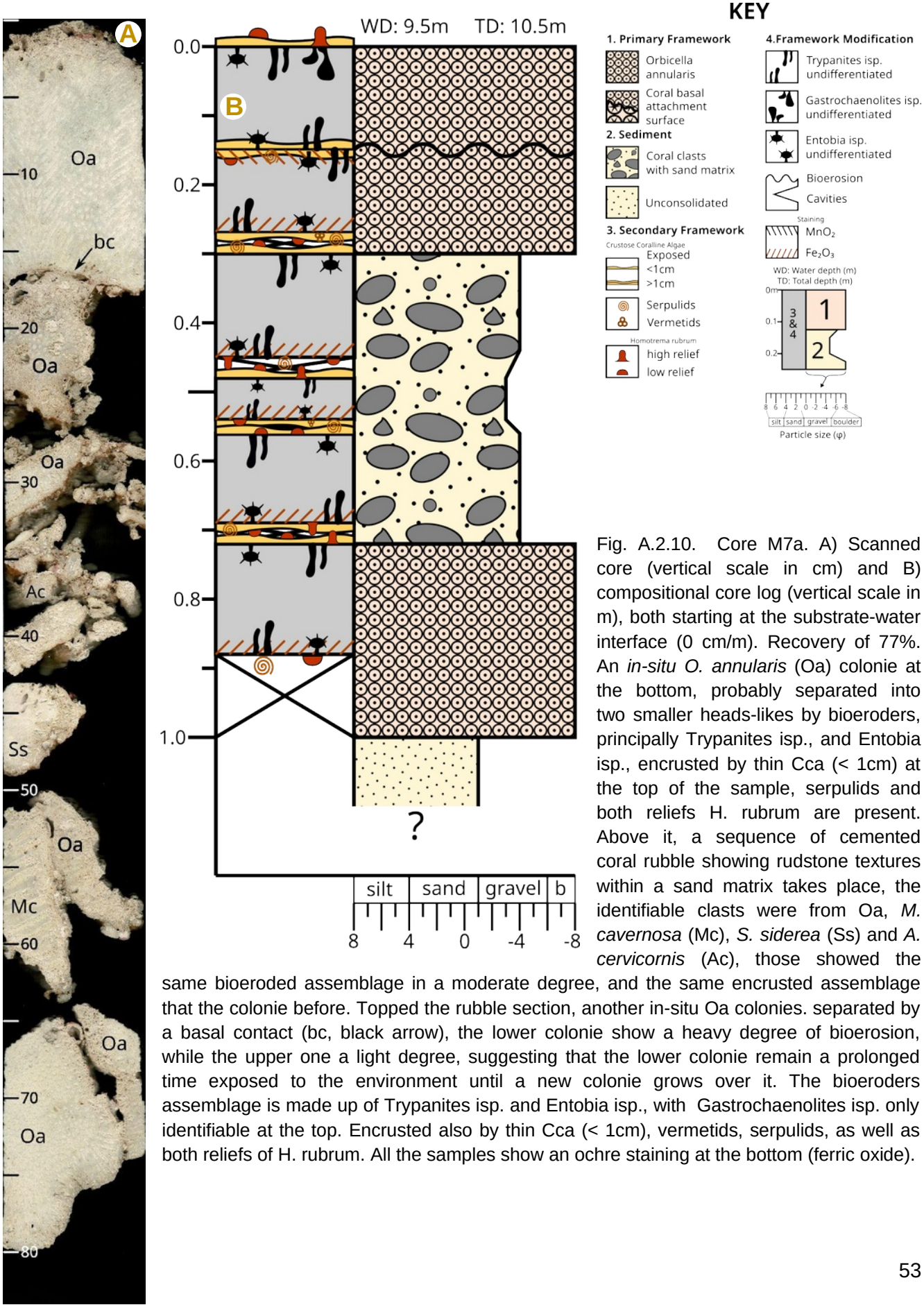

Fig. A.2.10. Core M7a. A) Scanned core (vertical scale in cm) and B) compositional core log (vertical scale in m), both starting at the substrate-water interface (0 cm/m). Recovery of 77%. An *in-situ O. annularis* (Oa) colonie at the bottom, probably separated into two smaller heads-likes by bioeroders, principally Trypanites isp., and Entobia isp., encrusted by thin Cca (< 1cm) at the top of the sample, serpulids and both reliefs H. rubrum are present. Above it, a sequence of cemented coral rubble showing rudstone textures within a sand matrix takes place, the identifiable clasts were from Oa, *M. cavernosa* (Mc), *S. siderea* (Ss) and *A. cervicornis* (Ac), those showed the same bioeroded assemblage in a moderate degree, and the same encrusted assemblage that the colonie before. Topped the rubble section, another in-situ Oa colonies. separated by a basal contact (bc, black arrow), the lower colonie show a heavy degree of bioerosion, while the upper one a light degree, suggesting that the lower colonie remain a prolonged time exposed to the environment until a new colonie grows over it. The bioeroders assemblage is made up of Trypanites isp. and Entobia isp., with Gastrochaenolites isp. only identifiable at the top. Encrusted also by thin Cca (< 1cm), vermetids, serpulids, as well as both reliefs of H. rubrum. All the samples show an ochre staining at the bottom (ferric oxide).

2.11. M7b

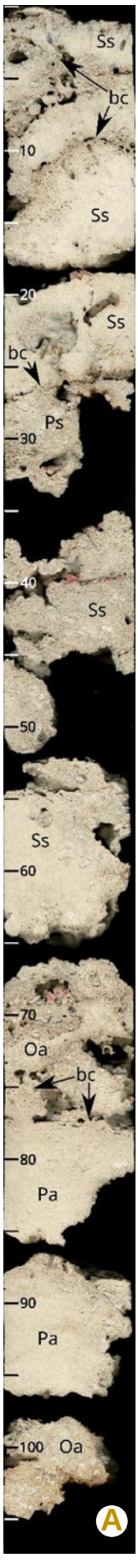

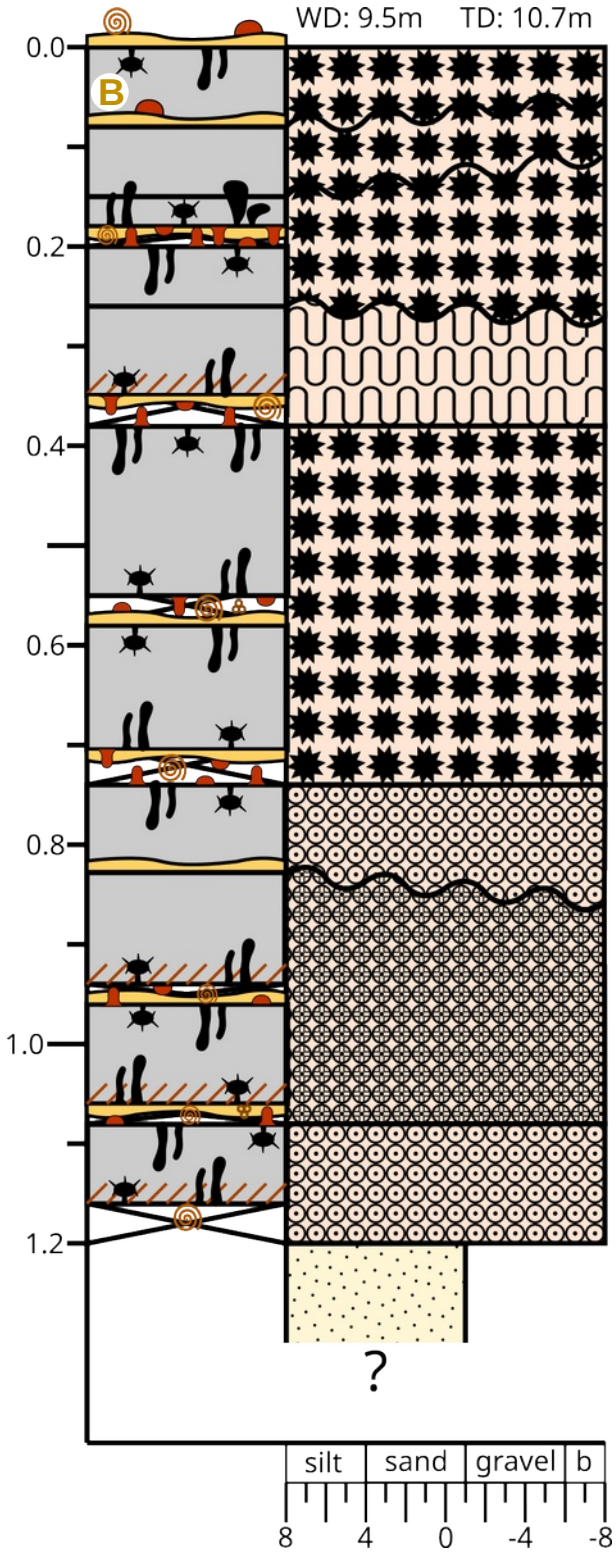

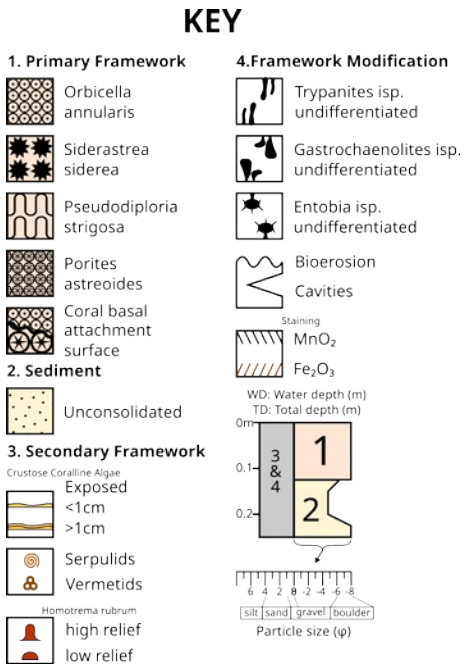

Fig. A.2.11. Core M7b. A) Scanned core (vertical scale in cm) and B) compositional core log (vertical scale in m), both starting at the substrate-water interface (0 cm/m). Recovery of 92.9%. A completely growth sequence, starting at the bottom with a small fragment of *O. annularis* (Oa) colonie, followed by two fragments, probably of the same colonie, of *P. astreoides* (Pa), the upper fragment present a basal contact (bc, black arrow), with an Oa colonie grow directly above it. Next, two fragments of *S. siderea* (Ss) colonies, it is not clear if they were part of the same colonie, fall behind a small *P. strigosa* (Ps) fragment with a bc with another Ss colonie fragment, this one comes after another fragment of the same species, again it is not clear if they were part of the same colonie. The growth sequence ends with an amalgamation of small Ss colonies, growing on top of each other with bc characterising its up oriented growth. All the colonie fragments are moderate to heavy bioeroded by Trypanites isp. and Entobia isp. with only Gastrochaenolites isp. identified in the upper samples. The majority of fragments are encrusted by thin Cca (< 1cm), vermetids, serpulids, as well as both reliefs of H. rubrum. An ochre staining is also visible in the three deepest samples as well as in the small Ps colonie.

2.12. M8a

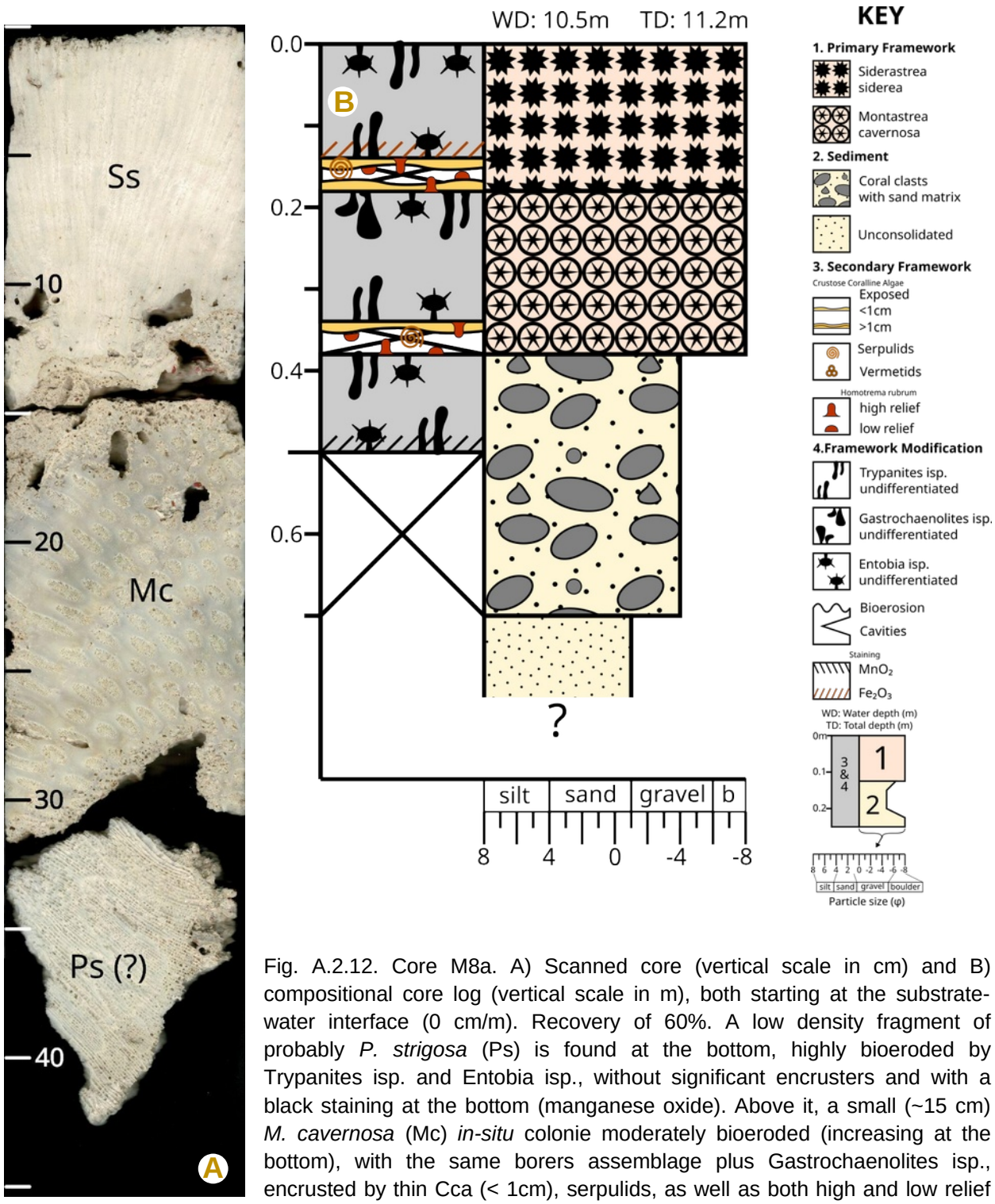

Fig. A.2.12. Core M8a. A) Scanned core (vertical scale in cm) and B) compositional core log (vertical scale in m), both starting at the substrate-water interface (0 cm/m). Recovery of 60%. A low density fragment of probably *P. strigosa* (Ps) is found at the bottom, highly bioeroded by Trypanites isp. and Entobia isp., without significant encrusters and with a black staining at the bottom (manganese oxide). Above it, a small (~15 cm) *M. cavernosa* (Mc) *in-situ* colonie moderately bioeroded (increasing at the bottom), with the same borers assemblage plus Gastrochaenolites isp., encrusted by thin Cca (< 1cm), serpulids, as well as both high and low relief H. rubrum. Topped by a small (~15 cm) in-situ colonie of *S. siderea* (Ss), equally moderately bioreoded, with the same borers and encrusted assemblage than the previous colonie, but with an ochre staining at the bottom (ferric oxide). No signs of basal contacts between the colonies are present.

2.13. M8b

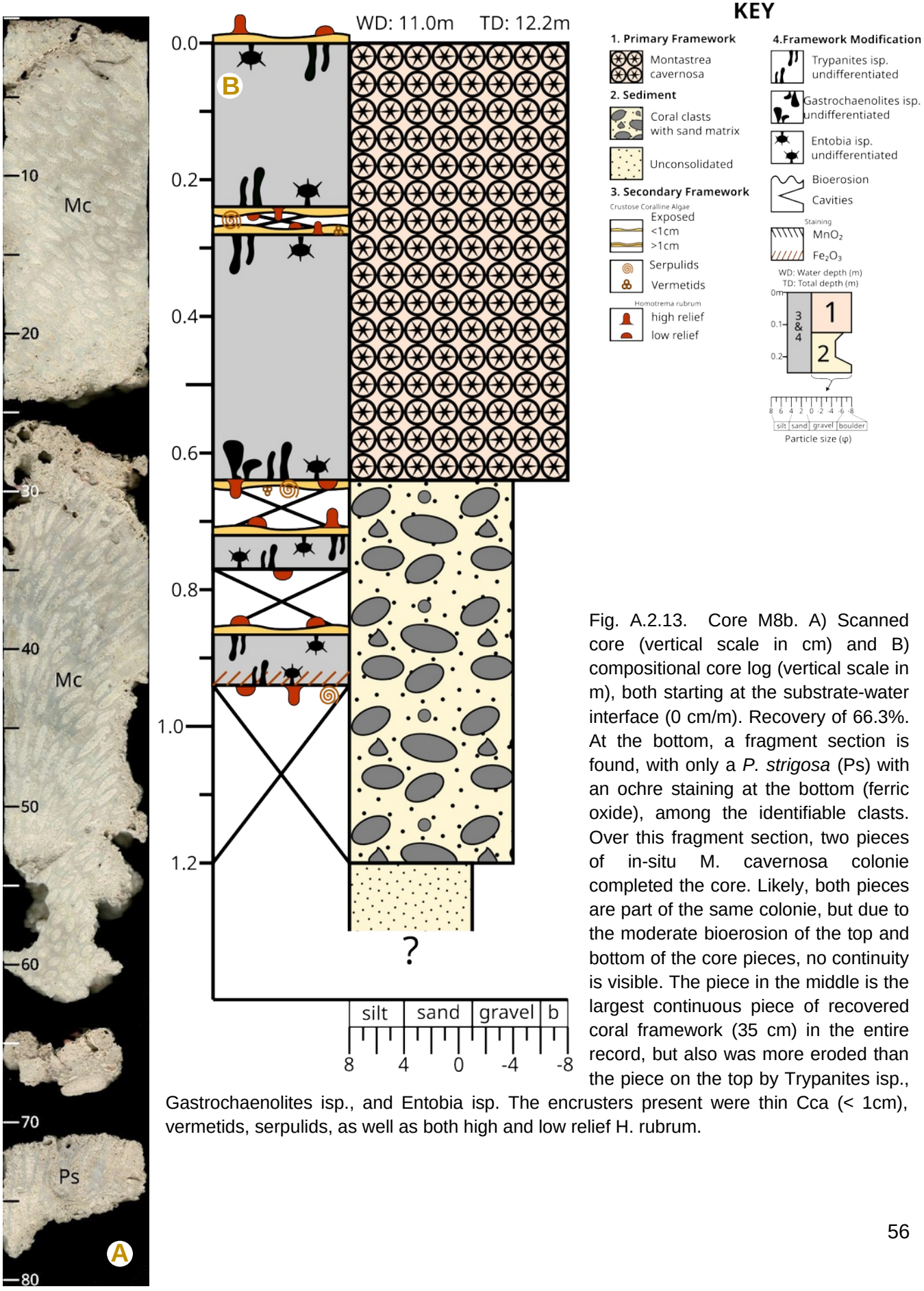

Fig. A.2.13. Core M8b. A) Scanned core (vertical scale in cm) and B) compositional core log (vertical scale in m), both starting at the substrate-water interface (0 cm/m). Recovery of 66.3%. At the bottom, a fragment section is found, with only a *P. strigosa* (Ps) with an ochre staining at the bottom (ferric oxide), among the identifiable clasts. Over this fragment section, two pieces of in-situ M. cavernosa colonie completed the core. Likely, both pieces are part of the same colonie, but due to the moderate bioerosion of the top and bottom of the core pieces, no continuity is visible. The piece in the middle is the largest continuous piece of recovered coral framework (35 cm) in the entire record, but also was more eroded than the piece on the top by Trypanites isp., Gastrochaenolites isp., and Entobia isp. The encrusters present were thin Cca (< 1cm), vermetids, serpulids, as well as both high and low relief H. rubrum.

ANNEX B

1. Initial Inversion Settings

1.1. Criteria for Data Removal

- For data removal, the parameters limits: *Min. Voltage*= 0.02 mV; *Min. abs(V/I)*= 2 x 10-5 Ohm; *Max. Repeat Error*= 3 %; *Min. App. Res*= 0.03 Ohm-m; y *Max App. Res*= 10000 Ohm-m, were set within the recommended and safe settings by the software manufacturer for the inversion process.

- *Remove Neg Res* parameter is set by default, due to the resistivity survey type carried out, the software automatically removes all negative apparent resistivity values, simultaneously with the run of *Min apparent resistivity* parameter.

- *Max. Reciprocal Error* parameter is effective only if reciprocal measurements were taken in the survey. Given that this was the case for DD arrays and after setting this parameter in its default value (5%) a negative effect was evident due to a considerable loss of data. For that reason and after a thorough analysis of those values (section B.3.2), a value of 10000% was set for this parameter, with the objective of making it inoperable, in order to avoid unnecessary data loss (Fig. B.1)

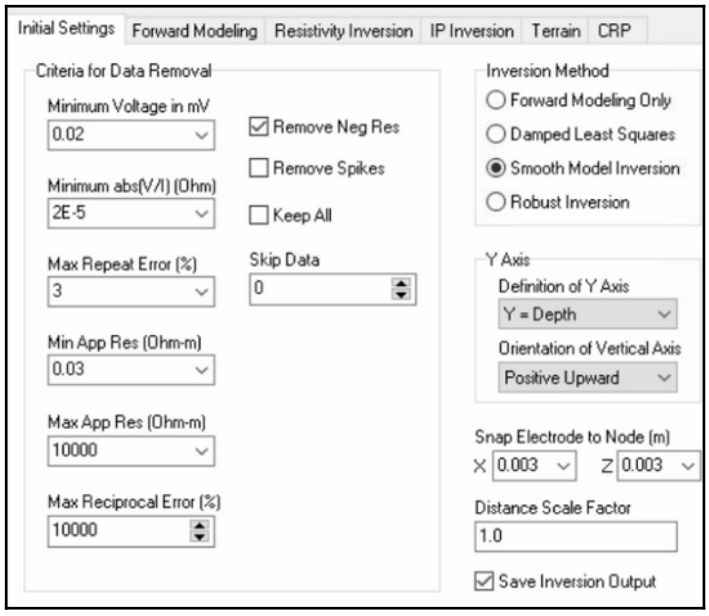

Fig. B.1. Initial Settings window. Both selected parameters and set values are shown.

2. Forward Modelling Settings

- Due to the loaded topography file (.uwt), the forward modelling method set automatically by the software is the *Finite Element Method*, because this method models earth topography better, thanks to a triangular mesh, which is very flexible to cope with topographical variations. This method is used to solve the following two-dimensional partial differential equation in the Fourier transform domain:

$$\frac{\partial}{\partial x}\left(\sigma\frac{\partial V}{\partial x}\right)+\frac{\partial}{\partial z}\left(\sigma\frac{\partial V}{\partial z}\right)-k^2\sigma V=-I\cdot\delta(x)\cdot\delta(z)$$

  where V is the scalar electrical potential in the Fourier transform domain; I is the electric current source; k is the wavenumber in the transform domain; and σ is electrical conductivity as a function of (x, z) (AGI EarthImager 2D, 2009).

- Both *Forward Equation Solve*r and *Type of Boundary* condition were left in its default set. Cholesky decomposition and Dirichlet respectively

- *Number of Mesh Divisions* parameter represents number of cells (blocks) between two electrodes, a finer mesh results in higher accuracy of forward modelling, but longer CPU time (AGI EarthImager 2D, 2009). After run different models with different number of mesh divisions allowed in the software (from 1 to 8 divisions), we conclude that the searched value (~1 Ohm-m) between the units R and B did not show significant variations in its location, therefore a mid value of mesh division was selected, equal to 4.

- *Thickness incremental factor* parameter applies mainly to resistivity surveys where model resolution degrades with depth, just as the current study. It is defined as the ratio of the thickness of the lower layer to the thickness of the layer immediately above it (AGI EarthImager 2D, 2009). Assuming that the lower layers are thicker than the immediate superior, a ratio smaller than 1.0 it is not realistic, based on that assumption, the value of this factor was left in its default setting (1.1).

- The last manageable parameter of this section was the *Depth factor* parameter and has the same considerations as the previous one. This one controls the depth of the inverted section, which is determined by the maximum median depth times the depth factor. Median depth is a function of electrode spacing and array type (AGI EarthImager 2D, 2009). A value of 1.0 was set to this parameter, given the decision of work with the original calculated depth for the inverted section, without adding additional calculations. Modification of this value had minimal effect in the position of the boundary between the units R and B (Fig. B.2).

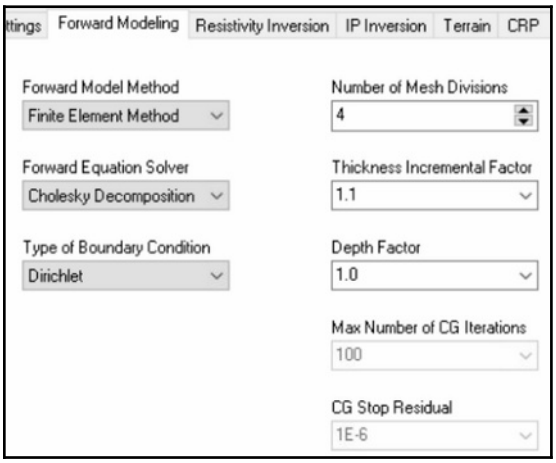

Fig. B.2. Forward Modelling settings window. Both selected parameters and set values are shown.

3. Resistivity Inversion Settings

3.1. Stop criteria

- *Number of Iterations* parameter was set at a value of 8, which is between the recommended ones by the software manufacturer for this kind of resistivity surveys.

- *Maximum RMS Error* parameter is measure of data misfit, the goal of it is to characterise the goodness of fit between the measured data and the predicted data, the value is represented in percent (%) and is defined by:

$$RMS = \sqrt{\frac{\sum_{i=1}^{N}\left(\frac{d_i^{Pred} - d_i^{Meas}}{d_i^{Meas}}\right)^2}{N}} * 100\,\%$$

  where N is the total number of measurements, d^{Pred} is the predicted data and d^{Meas} is the measured data. It is clear that the RMS error depends on the number of bad data points and how bad each bad data point is. It is also important to highlight that the RMS error is an average data misfit over all data points (AGI EarthImager 2D, 2009).

  This parameter was set with a value of 5%, which is within the usual ranges of measurement errors (1% to 5%), and fulfils the recommendations of the software manufacturer in which this number should be equal to or larger than the percentage of estimated noise (see section B.3.2).

- *Error Reduction* parameter remained disabled, which is its default, to avoid a termination of the inversion prematurely.

- *L2 Norm* parameter, is another measure of data misfit and it is enabled by default. It is defined as the sum of the squared weighted data errors, hence depends on the estimate of data weights (errors, section B.3.2):

$$L2-Norm = \sum_{i=1}^{N}\left(\frac{d_i^{calc} - d_i^{meas}}{W_i}\right)^2$$

  where N is the number of measurements. W_i is the data weight, d^{calc} is the calculated data, d^{meas} is the measured data.

  Due to the inversion method chosen (SMI), the software should stop when the L2-norm is smaller than the number of measurements. Since he number of measurements (data points) varies from data set to data set, the software manufacturer define a normalised L2-Norm measure as:

  Normalised L2-Norm = L2-Norm / (Number of Data)

  When the normalised L2-norm reduces to the unity (1.0) or smaller, the inversion is converged (AGI EarthImager 2D, 2009).

3.2. Data weights

- *Estimated Noise* parameter, it is assumed a certain percentage of error in data, the software usually ranges from 1% to 5%. Since the inversion algorithm used in the software minimises a weighted data misfit (L2-norm), a too large noise estimate generates a too smooth model, whereas a too small noise estimate forces the inversion to fit data noise, thus generating artefacts (AGI EarthImager 2D, 2009). The value used was 5%, which is within the recommended ranges.

- *Use Reciprocal Error* parameter, allows the use of these errors as data weights, if reciprocal measurements were taken during the data survey. The software would check for reciprocal measurements automatically while reading the data set, if it finds it, merges the forward and reverse measurements by averaging, and calculates a relative reciprocal error. If the reciprocal error is above the threshold set on the Initial Settings window (section B.1.1), it is deleted (AGI EarthImager 2D, 2009).

  Reciprocal measurements are taken by swapping current and voltage electrode pairs, that is, electrodes A and B are used as potential electrodes while electrodes M and N are used as current electrodes. Theoretically, the reciprocal measurement should yield the same resistance and hence apparent resistivity. The reciprocal measurements are evaluated in different ways, the most common being reciprocal standard error and reciprocity. If the normal and reciprocal measurements of apparent resistivity are $\rho_{a,1}$ and $\rho_{a,2}$, and the average resistivity is $\rho_{a,ave} = \frac{\rho_{a,1} + \rho_{a,2}}{2}$, the reciprocal standard error $\mathbf{s_{recip}}$ and reciprocity **r** are given by (Singha et al., 2022) :

$$s_{recip} = \sqrt{\frac{\left(\rho_{a,1} - \rho_{a,ave}\right)^2 + \left(\rho_{a,1} - \rho_{a,ave}\right)^2}{2}}$$

$$r = \left| \left(\frac{\rho_{a,1} - \rho_{a,2}}{\rho_{a,ave}} \right) \right|$$

  The reciprocity is a dimensionless measure of relative error and, when multiplied by 100, gives the percent error in the reciprocal measurement and is in that way in which EarthImager works. After the initial tests with raw DD data (unique arrays with reciprocal measurements), we noticed that a set value of *Max. Reciprocal Error* of 5%, within the usual ranges, in the initial setting window (section B.1.1), the number of data removed was 272 from 638, around 42.6% of the data set. Duplicating this value to 10%, the percentage of removed data was reduced by half, 20.1% (132 data removed from 638).

  Nevertheless, the amount of data loss was relatively high for one single parameter, and after the analysis of the data with emphasis in the reciprocal measurements using a Python code in Google Colab, we note that the majority of ρ_a values were lower than 1 Ohm-m (Fig, B.3.1.a). Since those values are used to evaluate the reciprocal measurements by means of the reciprocity (**r**), the average of those values is smaller, which translated to the reciprocity equation gave a fraction with a small denominator,

therefore smaller denominator, biggest error (Fig. B.3.1.b). Given that the ρ_a is small, likely due to the underwater nature of the survey, the elimination of data based on this criteria does not provide any benefit to the inversion, nor as data weights. For those reasons this parameter was not taken into account.

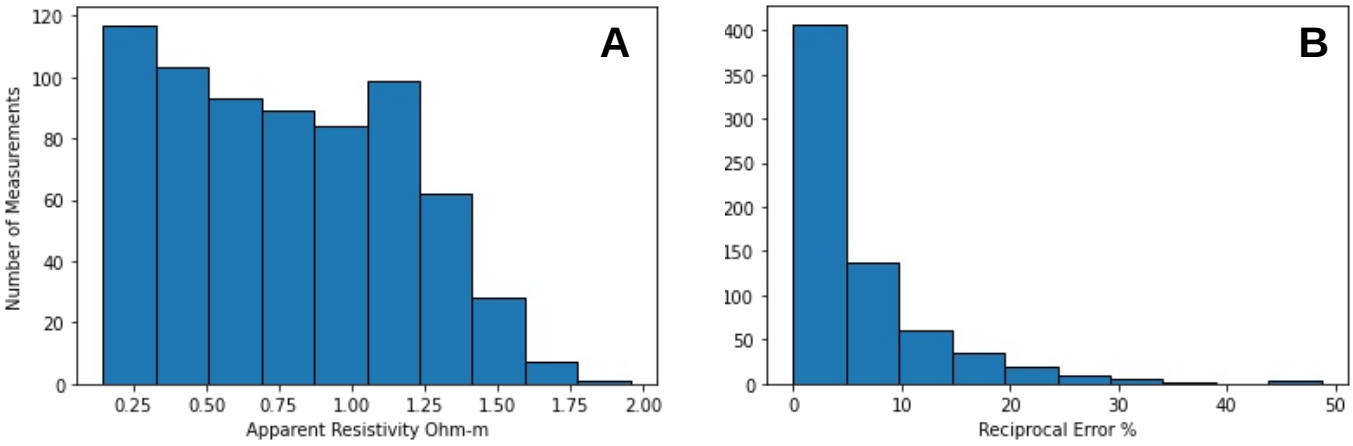

Fig. B.3.1. Reciprocal error analysis. A) Apparent resistivity histogram, note that the majority of values were lower than 1 Ohm-m. B) Reciprocal error histogram, note the amount of errors higher than 5%, for a better visualisation, 6 values higher than 50 % were removed.

- *Suppress Noisy Data* parameter it is enabled by default. This parameter gives less weight to noisy and hard-to-fit data improving dramatically the L2-norm convergence (AGI EarthImager 2D, 2009).

3.3. Horizontal/Vertical Roughness Ratio

If you have enough information about the geology of the project site, this parameter can help you to highlight the characteristics of the area. If strong lateral resistivity variations are present, the parameter should be set larger than 1.0. In contrast, if vertical variations are present (layered earth), the value should be set smaller than 1.0 (AGI EarthImager 2D, 2009). Given that we wanted to highlight the boundary between two layers, and we know that there is a certain vertical variation in the reef, the parameter was set on 0.1.

All the remaining manageable parameters on this resistivity inversion settings: *Smoothness factor; Damping factor; Starting model; Min resistivity; Max resistivity; Model parameter width; and Resolution factor*, were left in its default set. Because these values worked properly to obtain the desired inversion model (Fig. B.3.#).

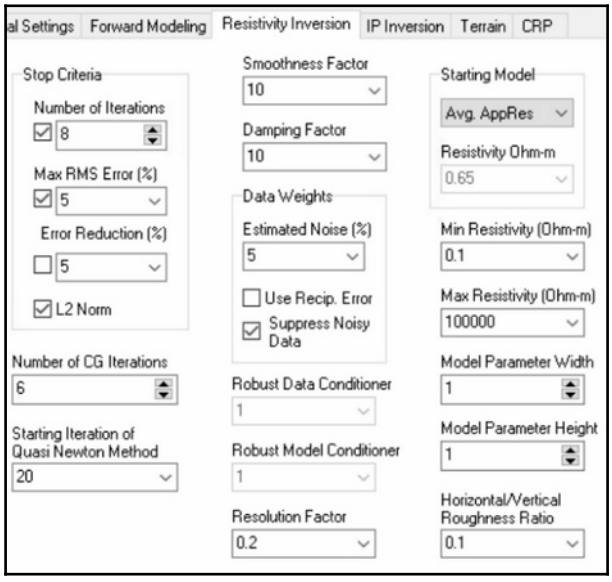

Fig. B.3.2. Resistivity Inversion settings window. Both selected parameters and set values are shown.

4. .UWT files

.UWT files were created from the bathymetric profile obtained with a PLASTIMO Echotest II hand-held echo sounder, during the electrical resistivity survey, and were the follows:

T1.uwt file	T2.uwt file
;Sample underwater terrain file (*.UWT) ;Any line started with ';' is a comment line unit=meters ;case flag: underwater survey cases. ; 1 - Underwater without terrain, ; 2 - underwater w/ terrain ; 3 - mixed surface and underwater electrodes w/ terrain 2 ;Water resistivity. If unknown, leave it blank WaterRes= ; Case 2: X below is the horizontal distance ; X, Water Depth 0, 8.0 5, 7.7 10, 7.3 15, 7.3 20, 7.2 25, 7.3 30, 7.0 35, 6.9 40, 6.9 45, 6.9 50, 6.9 55, 6.9 60, 6.9 65, 6.6 70, 6.4 75, 6.1 80, 6.4 85, 5.4 90, 5.7 95, 5.6 100, 5.4 105, 5.3 110, 5.1 115, 5.0 120, 4.3 125, 4.4 130, 3.8 135, 3.7 140, 3.5 145, 3.4 150, 2.8 155, 2.5 160, 2.1 165, 2.0 170, 1.8 175, 1.6 180, 1.3 185, 0.9 190, 0.7 195, 0.7 200, 0.6 205, 0.6 210, 0.5 215, 0.4 220, 0.3 225, 0.2 230, 0.2 235, 0.1 240. 0.1 245, 0.1 250, 0.1 255, 0.1 260, 0.1 265, 0.1 270, 0.1 275, 0.1	;Sample underwater terrain file (*.UWT) ;Any line started with ';' is a comment line unit=meters ;case flag: underwater survey cases. ; 1 - Underwater without terrain, ; 2 - underwater w/ terrain ; 3 - mixed surface and underwater electrodes w/ terrain 2 ;Water resistivity. If unknown, leave it blank WaterRes= ; Case 2: X below is the horizontal distance ; X, Water Depth 0, 8.3 5, 7.7 10, 7.2 15, 7.3 20, 7.2 25, 7.3 30, 7.0 35, 6.9 40, 7.2 45, 6.9 50, 6.9 55, 6.6 60, 6.4 65, 6.1 70, 6.4 75, 5.4 80, 5.7 85, 5.6 90, 5.4 95, 5.3 100, 5.1 105, 4.0 110, 3.1 115, 3.2 120, 3.3 125, 3.4 130, 3.8 135, 4.0 140, 3.8 145, 3.7 150, 3.5 155, 3.4 160, 3.3 165, 2.8 170, 2.5 175, 2.1 180, 2.0 185, 1.4 190, 1.8 195, 1.5 200, 1.6 205, 1.2 210, 1.3 215, 0.9 220, 0.7 225, 0.5 230, 0.4 235, 0.3 240, 0.2 245, 0.1 250, 0.1 255, 0.1 260, 0.1 265, 0.1 270, 0.1 275, 0.1

For both files, *WaterRes* parameter was intentionally left blank, because although a single water resistivity measurement was taken in the BR, at the time of running the inversion process with this single value fixed, the software created an homogeneous resistivity water layer. This caused very noticeable resistivity artefacts in the models, between the water-land transition zone, consequently losing sensitivity between the boundary of interest, boundary between units R and B. It was concluded that constraining this value to a single one triggered an adjustment of all the other resistivity values, in that way the software fit the homogeneous resistivity water layer into the model (Fig. B.4). For that reason and for the not realistic scenario with only one resistivity value for the entire water column over the reef, as shown in the final resistivity profiles (Fig. 21), this value was not set.

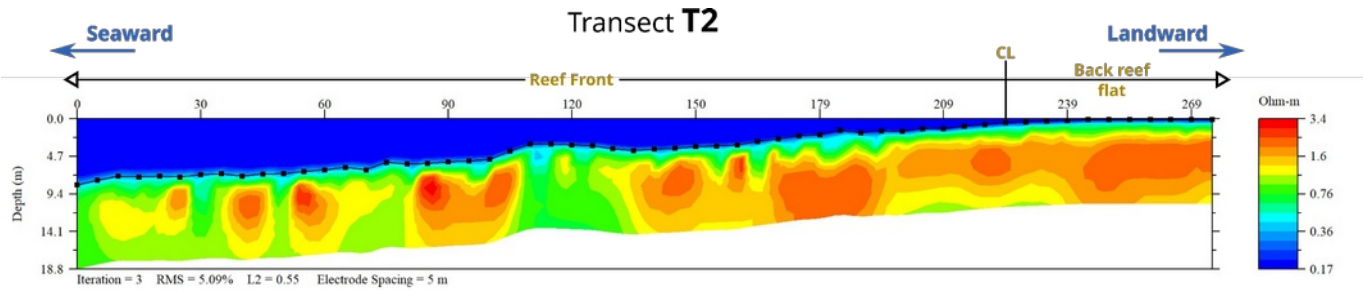

Fig. B.4. T2 Electrical Resistivity Profile with water resistivity value set. Inverted resistivity section with the single measured value of water resistivity in Mahahual reef, set in the .uwt file (0.17 Ohm-m). Therefore a single constant resistivity value is shown for the entire water unit (unit W), causing that the high resistivity values for unit B in the front reef, reduce its depth in comparison with the final model, also they resemble more like concentrated values with peaks toward up, than a layer. While in the back reef flat, the level of water is minimum and does not have significatively effect on the subsurface resistivity values, since they keep the same flat-like shape beneath it. This is a good example of how a single parameter can give us a different interpretation of the same data set. For this inverted section, we used almost the same parameters as in the final models (Fig. 21), changing only the Number of Mesh Divisions = 2, and Depth Factor= 1.1. In the upper x axis the cable length in m, from x=0m (starting point) at the middle of the reef structure, to x=275m (end point) in the back reef flat. Over it, the reef zonation is displayed, as well as its orientation. The cabled electrodes are displayed as a black line with 56 square dots, which represent the 56 passive electrodes. In this section, a dotted red line was not drawn, because the objective was to show the resistivity variations and not the boundary between units R and B. The y axis shows the depth in m, starting at 0m at SL. CL= Crest line.

5. Number of processed data, RMS and L2 values for each transect

Transect	Data number	Iteration	RMS %	L2
T1	821	3	6.64	0.38
T2	1016	2	4.21	0.46

6. Inverted resistivity profile in XYZ format

In order to visualise the calculated inverted resistivity data by the software and give an estimate of the accuracy of the resultant model, we saved the inverted resistivity section (Electrical Resistivity Profiles in the results) in a XYZ data format allowed by the software, afterwards we use Google Colab to write and execute a Python code that allow us to visualise and analyse this XYZ data form, where X and Y are the coordinates of location in two dimensions over the transect, and Z is the calculated resistivity value in the subsurface for each ordered pair.

It is important to remember that the goal of the inversion process is to invert the measured data to obtain a spatially discretized distribution (gridded or meshed) of the electrical properties of the subsurface (Singha et al., 2022). That is, we will obtain from the inversion process a dot mesh which represents the electrical response of the subsurface.

So, the obtained mesh after serial tests of the principal mesh constructors parameters, Number of Mesh Divisions = 4, Thickness incremental factor= 1.1 and Depth Factor= 1.0, section B.2 for T2, was a mesh with 222 points in the X axis and 2368 points in the Y axis (FIg. B.6.2). This mesh plot show how the final model is constructed by dot strings with individual values of Z. It is visual simple to note that in the X axis the separations of the dots are almost all equidistant one to each other, while in the Y axis is noticeable that the separation of the dot strings increase with the depth, this is because of the *Thickness incremental factor*, which assume that the lower layers are thicker than the immediate superior, and in this case with a ratio of 1.1 (section B.2). Additionally, this axis is affected by the underwater topography (yellow line; .uwt file, section B.4), given that it is clear that the dot strings below it follow its shape, this is one reason for which interpreting the contours of the final models as definitive shapes is not always the real shape, as well as only guide it by the colour scale. When a resistivity inversion is carried out without a topography file, the dot mesh is represented by parallel dot strings.

Another reason are the resistivity artefacts that could be generated, just as the isolated data points in the T1 mesh (Fig. B.6.1), which were displayed in the final profiles as small areas of high resistivity values in the water-substrate interface, as a result of presenting a complete profile adjusting the surrounding values to fit the high resistivity ones.

In order to objectively characterise the bedrock position we took a resistivity value rather than only the visual contour of the final model to delimit units R and B (1 Ohm-m), for this, in the plot it is possible to know which value of Z corresponds to each point by only setting the cursor above a point, following this pattern the bedrock boundary was drawn. As the position of the boundary was not at the same depth, the accuracy of it was taken from the extreme points (start and end) of the mesh. In the deeper part of T2, the boundary was set at ~18 m below SL and the separation of the dot strings above and beneath it was from around 2 m each, giving us as a result a range of error of 2 m. For the shallowest part was the same process, only in this case being a shallower depth (~ 2m), the separation of the strings was smaller, around 1 m, resulting in the range of error for this point (Fig. B.6.2). So, the threshold of error is based on the dot mesh construction given certain chosen parameters.

The resistivity value taken for the boundary was not continue either over the entire mesh, between 100 and 130 m in the X axis, low resistivity values are showed between mid resistivity values at the same depth, this is most likely the effect of the ridge-like topography above it,

which altered the survey and gave the impression of a conductive body in the subsurface (low resistivities values, pag. 15).

This analysis was performed for both resistivity transects (T1 and T2), but given that in T2 was possible to acquire the three data arrays, and therefore was the one with more data for the inversion process (section B.5), it was taken as representative for the full reef structure.

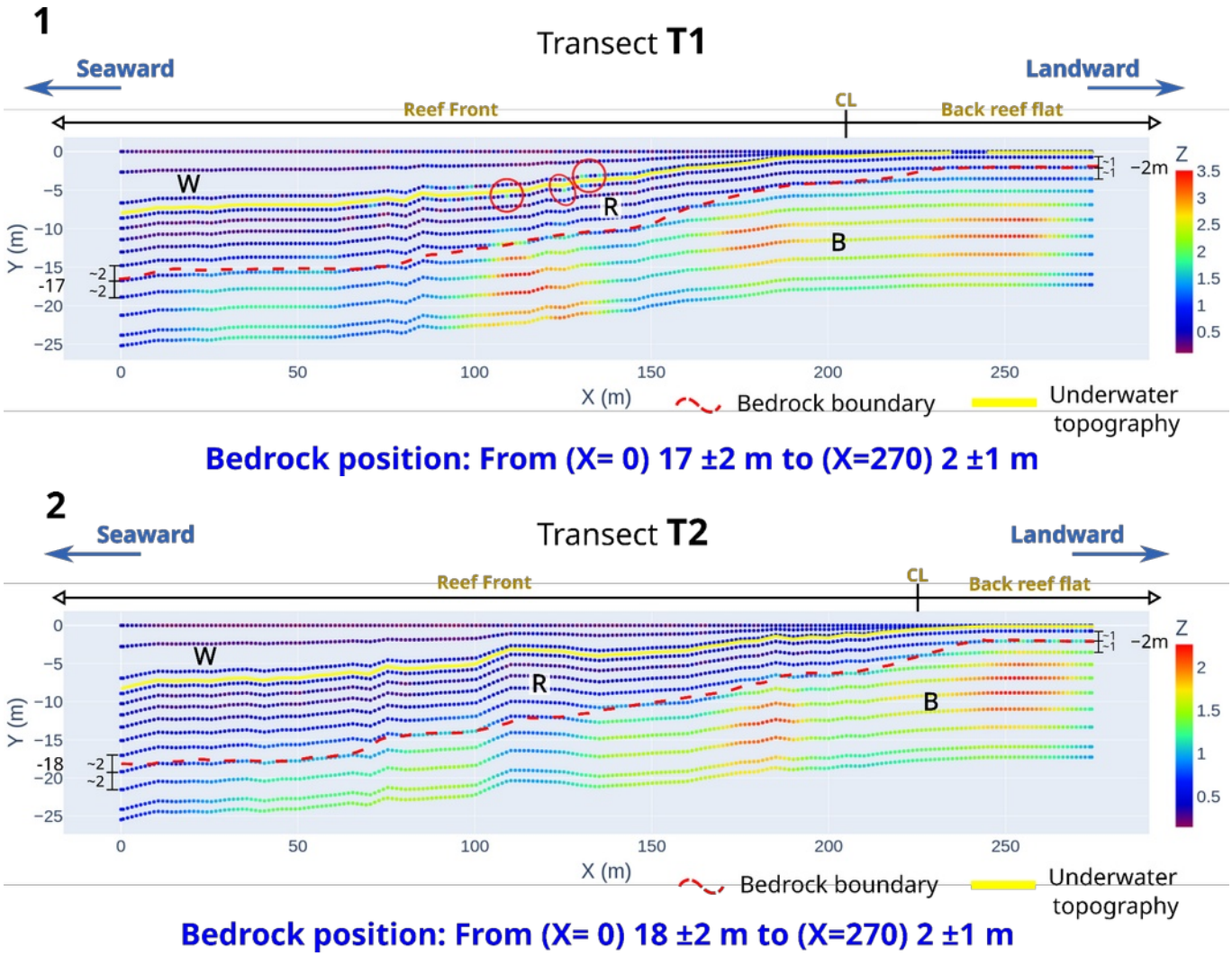

Fig. B.6. ER mesh profiles. 1) T1 Electrical Resistivity Mesh, red circles showed the high resistivity isolated dat points. 2) T2 Electrical Resistivity Mesh. In the lower axis, the cable length in m, from X=0m (starting point) at the middle of the reef structure, to X=275m (end point) in the back reef flat. Over it, the reef zonation is displayed, as well as its orientation. The underwater topography is displayed as a yellow line. The dotted red line represents the boundary between the reef deposit and underlying bedrock, following the resistivity value of 1 Ohm-m in the dot mesh. The colour scale on the right is not the same as the one used in the final profiles because the aim of this analysis was to delineate the boundary based on data, not colour. So, homogenising the colour scale was not important. The Y axis shows the depth in m, starting at 0m at SL. CL= Crest line; B= unit B (bedrock, high resistivity unit ≥ 1 Ohm-m); R= unit R (reef deposit, 0.2 Ohm-m < mid/low resistivity unit ≤ 1 Ohm-m); and W= unit W (Water column, low resistivity unit < 0.7 Ohm-m.).